Draft version June 30, 2014
Preprint typeset using LaTeX style emulateapj v. 5/2/11

arXiv:1406.7034v1 [astro-ph.SR] 26 Jun 2014

# CARBON-RICH DUST PAST THE ASYMPTOTIC GIANT BRANCH: ALIPHATICS, AROMATICS, AND FULLERENES IN THE MAGELLANIC CLOUDS

G. C. Sloan[1], E. Lagadec[1], A. A. Zijlstra[2], K. E. Kraemer[3], A. P. Weis[4,5], M. Matsuura[6], K. Volk[7], E. Peeters[8,9], W. W. Duley[10], J. Cami[8,9], J. Bernard-Salas[11], F. Kemper[12], & R. Sahai[13]

*Draft version June 30, 2014*

## ABSTRACT

Infrared spectra of carbon-rich objects which have evolved off the asymptotic giant branch reveal a range of dust properties, including fullerenes, polycyclic aromatic hydrocarbons (PAHs), aliphatic hydrocarbons, and several unidentified features, including the 21 $\mu$m emission feature. To test for the presence of fullerenes, we used the position and width of the feature at 18.7–18.9 $\mu$m and examined other features at 17.4 and 6–9 $\mu$m. This method adds three new fullerene sources to the known sample, but it also calls into question three previous identifications. We confirm that the strong 11 $\mu$m features seen in some sources arise primarily from SiC, which may exist as a coating around carbonaceous cores and result from photo-processing. Spectra showing the 21 $\mu$m feature usually show the newly defined Class D PAH profile at 7–9 $\mu$m. These spectra exhibit unusual PAH profiles at 11–14 $\mu$m, with weak contributions at 12.7 $\mu$m, which we define as Class D1, or show features shifted to $\sim$11.4, 12.4, and 13.2 $\mu$m, which we define as Class D2. Alkyne hydrocarbons match the 15.8 $\mu$m feature associated with 21 $\mu$m emission. Sources showing fullerene emission but no PAHs have blue colors in the optical, suggesting a clear line of sight to the central source. Spectra with 21 $\mu$m features and Class D2 PAH emission also show photometric evidence for a relatively clear line of sight to the central source. The multiple associations of the 21 $\mu$m feature with aliphatic hydrocarbons suggest that the carrier is related to this material in some way.

*Subject headings:* circumstellar matter — infrared: stars

## 1. INTRODUCTION

Amorphous carbon dominates the circumstellar dust in carbon-rich stars on the asymptotic giant branch (AGB; e.g. Martin & Rogers 1987; Groenewegen et al. 2009). By the time an object has evolved to a mature planetary nebula (PN), the well-known series of infrared (IR) emission features at 3.29, 6.2, 7.7–7.9, 8.6, 11.3, and 12.7 $\mu$m dominate the dust emission. Polycyclic aromatic hydrocarbons (PAHs) are commonly invoked as their carrier.

Carbon-rich objects between the AGB and mature PNe can display a rich variety of spectra. One family of intriguing spectral features is associated with the still unidentified 21 $\mu$m feature discovered by Kwok et al. (1989) in spectra of carbon-rich post-AGB objects. Related features include those at 8, 11, 16, and 26–30 $\mu$m (e.g. Kraemer et al. 2002; Volk et al. 2011).

Circumstellar hydrocarbons can appear in even more exotic forms, as demonstrated by the discovery of $C_{60}$ and $C_{70}$ (referred to here collectively as fullerenes) in the spectrum of a Galactic PN (Cami et al. 2010). García-Hernández et al. (2010) discovered several more PNe showing fullerenes, including one in the Small Magellanic Cloud (SMC), and García-Hernández et al. (2011) added 10 more PNe to the list of Magellanic fullerene candidates (see Bernard-Salas et al. 2012, for references to recent fullerene detections). Previous detections of fullerenes in PNe indicate that they only appear when the central star is still relatively cool (e.g. García-Hernández et al. 2012; Otsuka et al. 2013).

The sensitivity of the Infrared Spectrograph (IRS; Houck et al. 2004) on the *Spitzer Space Telescope* (Werner et al. 2004a) made it possible to obtain rich sets of infrared spectra in the Magellanic Clouds, where we can overcome the uncertainty in distances to Galactic sources and obtain samples less biased by dust extinction in the Galactic plane. The IRS observed over 40 carbon-rich post-AGB objects in the Magellanic Clouds. This paper examines those spectra and relates the character of the dust emission to the properties of the central star and its circumstellar environment. In such a way we can add to our knowledge of the forms carbon-rich dust can take and how those forms respond to photo-processing and evolve as they move from circumstellar environments

[1] Center for Radiophysics & Space Research, Cornell Univ., Ithaca, NY 14853-6801, USA, sloan@isc.astro.cornell.edu
[2] Jodrell Bank Centre for Astrophysics, Univ. of Manchester, Manchester M13 9PL, UK
[3] Institute for Scientific Research, Boston College, 140 Commonwealth Avenue, Chestnut Hill, MA 02467, USA
[4] Department of Astronomy & Astrophysics, Columbia Univ., 550 W. 120th St., New York, NY 10027, USA
[5] Research Experience for Undergraduates, Department of Astronomy, Cornell University, Ithaca, NY 14853-6801, USA
[6] Astrophysics Group, Department of Physics & Astronomy, Univ. College London, Gower Street, London WC1E 6BT, UK
[7] Space Telescope Science Institute, 3700 San Martin Dr., Baltimore, MD 21218
[8] Department of Physics & Astronomy, University of Western Ontario, London, ON N6A 3K7, Canada
[9] SETI Institute, 189 Bernardo Ave., Suite 100, Mountain View, CA 94043
[10] Department of Physics & Astronomy, Univ. of Waterloo, 200 University Ave. W., Waterloo, ON N2L 3G1, Canada
[11] Department of Physical Sciences, The Open University, Walton Hall, Milton Keynes, MK7 6AA, UK
[12] Academia Sinica, Institute of Astronomy and Astrophysics, 11F Astronomy-Mathematics Building, NTU/AS, No. 1, Sec. 4, Roosevelt Rd., Taipei 10617, Taiwan, R.O.C.
[13] Jet Propulsion Laboratory, MS 183-900, California Institute of Technology, Pasadena, CA 91109, USA

into the interstellar medium.

Our focus is primarily observational and will rely on classification and methods of analysis that minimize assumptions about the spectra. By analyzing the IRS data and the photometric properties of the sources, we can uncover clues about the nature of carbon-rich circumstellar dust. Section 2 defines the sample and describes how it was observed with the IRS. In Section 3 we explain how the sources are classified in spectroscopic groups and focus in turn on how different forms of dust contribute to the spectra. Section 4 turns to ancillary data including optical and infrared photometry and optical spectroscopy. Section 5 discusses the accumulated evidence, and Section 6 summarizes the results.

## 2. THE SPECTRAL SAMPLE

### 2.1. *Selection*

Our sample is composed of spectra from several *Spitzer* programs. We inspected all IRS spectra observed in the Magellanic Clouds, focused on those showing carbon-rich properties, and classified them following the criteria and methods described by Kraemer et al. (2002). The carbon-rich sample was then culled, based on our spectral classifications, so that we could focus on the behavior of the dust in those carbon-rich sources in evolutionary phases between the AGB and mature PNe. We did not consider the photometry at this stage because we wish to consider the photometric properties of the sample independently from their spectral properties (Sec. 4.1).

The largest of the excluded carbon-rich groups consists of nearly 150 carbon stars in the LMC and 40 in the SMC. These stars are on the AGB and have spectral energy distributions (SEDs) that peak at wavelengths below $\sim$20 $\mu$m and show absorption from $C_2H_2$ at 7.5 and 13.7 $\mu$m and/or emission from SiC dust at $\sim$11 $\mu$m. The brighter stars in this group have been the subject of several studies (e.g. Sloan et al. 2006; Zijlstra et al. 2006; Lagadec et al. 2007; Leisenring et al. 2008; Gruendl et al. 2008). The dust in their spectra is predominantly amorphous carbon, SiC, and MgS (assuming that MgS is the carrier of the 26–30 $\mu$m feature; see Section 3.6).

We also exclude the other evolutionary endpoint, mature PNe, which have spectra dominated by PAHs and forbidden lines. Multiple papers have studied the Magellanic PNe observed by the IRS (e.g. Stanghellini et al. 2007; Bernard-Salas et al. 2009).

R CrB candidates are also not included, because they represent an unusual evolutionary path outside our scope (e.g. Clayton 2012). Their spectra typically resemble a Planck curve of a few hundred K, due to emission from warm amorphous carbon dust (see Kraemer et al. 2005). The recent work by García-Hernández et al. (2013) reveals PAH-related structures in the spectra of several Galactic R CrB stars observed by the IRS.

Also excluded are those spectra showing strong hydrocarbon absorption features in their spectra (Kraemer et al. 2006; Bernard-Salas et al. 2006). These sources appear to be special cases of edge-on disk geometry.

Table 1 presents the resulting sample. We added one source, the PN SMP LMC 099, which has the spectral characteristics of a mature PN, but had previously been included in sources with fullerenes identified in their spectra (García-Hernández et al. 2011). The remaining sources should be intermediate in nature between the carbon-rich AGB and mature PNe, and they show a rich variety of carbon-rich dust emission features, including fullerene emission, the 21 $\mu$m features, other related features, and/or unusual PAH-like emission features.

The sources in our sample were observed in several IRS programs constructed to meet different scientific objectives. Thus our sample must be affected by multiple biases and should not be considered to be complete. It includes at least one source, SMP SMC 025, which turned out to be oxygen-rich, despite the presence of an 11 $\mu$m feature similar to the SiC feature commonly seen in carbon-rich objects.

Where sources have SMP designations, we have adopted them in Table 1 to remain consistent with previous publications and to indicate that they have been previously identified as PNe (Sanduleak et al. 1978). Otherwise, we adopt the historical name for an object, although if a source received a coordinate-based name at roughly the same time it received a shorter designation, we preferred the latter.

The coordinates in Table 1 are based on the positions of the sources in near-IR surveys. Appendix 2 provides more detail on how these were determined.

### 2.2. *Observations and Reduction*

All observations were obtained by the IRS in standard staring mode, which involved two pointings in each spectral aperture. All but one source was observed with the Short-Low (SL) and Long-Low (LL) modules. The exception, IRAS 05413, was observed using SL, along with the Short-High (SH) and Long-High (LH) modules.

We followed the standard data reduction scheme as described in more detail by Sloan et al. (2014), starting with data produced by the S18.18 version of the pipeline at the *Spitzer* Science Center. For SL, we used images with the source in one aperture as the background for when the source is in the other aperture (i.e., SL order 1 − SL order 2 and vice versa). For LL, we removed the background by differencing images with the source in the same aperture, but the other nod position. For the source observed in SH and LH, we subtracted a dedicated background image obtained in a nearby field. Images were cleaned for bad pixels using the IRSCLEAN package in IDL.

We deviated from previous reduction schemes by extracting the spectra using the optimal extraction algorithm described by Lebouteiller et al. (2010) for all spectra except IRAS 05413, which was extracted using the older additive algorithm (also known as tapered-column extraction), due to the observational design with SH and LH. We resampled this spectrum to match the spectral resolution of the other observations in our sample.

Spectra from separate nods were compared to remove spikes and divots and then combined. To remove discontinuities between spectral segments, we normalized them upward to the segment which was presumably best centered in the spectrographic slits.

Appendix 1 describes our method of spectral analysis and includes tables presenting extracted strengths and positions of the various spectral features considered in the following sections.

## 3. SPECTRAL PROPERTIES

TABLE 1
The sample

| Source[a] | Alias | RA (J2000) | Dec. (J2000) | Program ID | AOR key | Group[b] |
|---|---|---|---|---|---|---|
| SMP SMC 001 | LHA 115-N 1 | 00 23 58.63 | −73 38 04.0 | 103 | 4953088 | Mixed |
| IRAS 00350−7436 | | 00 36 59.58 | −74 19 50.3 | 50240 | 27517184 | PAH-like |
| SMP SMC 006 | LHA 115-N 6 | 00 41 27.75 | −73 47 06.5 | 103 | 4954112 | PAH-like |
| LIN 49 | | 00 43 53.89 | −72 55 14.7 | 50240 | 27537664 | Fullerene |
| 2MASS J00444111−7321361 | | 00 44 41.11 | −73 21 36.2 | 50240 | 27525120 | 21 $\mu$m (D2) |
| SMP SMC 011 | LHA 115-N 29 | 00 48 36.52 | −72 58 00.9 | 103 | 15902976 | Red |
| SMP SMC 013 | LHA 115-N 38 | 00 49 51.64 | −73 44 21.5 | 20443 | 14706176 | Mixed |
| SMP SMC 015 | LHA 115-N 43 | 00 51 07.37 | −73 57 37.6 | 20443 | 14706688 | Mixed |
| SMP SMC 016 | LHA 115-N 42 | 00 51 27.17 | −72 26 11.7 | 20443 | 14706944 | Fullerene |
| SMP SMC 018 | LHA 115-N 47 | 00 51 58.31 | −73 20 31.8 | 20443 | 14707456 | Mixed |
| SMP SMC 020 | LHA 115-N 54 | 00 56 05.38 | −70 19 25.9 | 20443 | 14707968 | Big-11 |
| SMP SMC 024 | LHA 115-N 70 | 00 59 16.11 | −72 01 59.9 | 103 | 15901952 | Fullerene |
| SMP SMC 025 | LIN 357 | 00 59 40.51 | −71 38 15.0 | 20443 | 14708480 | Red (SX) |
| 2MASS J01054645−7147053 | | 01 05 46.46 | −71 47 05.3 | 50240 | 27518464 | 21 $\mu$m (D2) |
| SMP SMC 027 | LHA 115-N 87 | 01 21 10.65 | −73 14 34.8 | 20443 | 14708992 | Big-11 |
| SMP LMC 002 | | 04 40 56.70 | −67 48 01.5 | 103 | 4946944 | Fullerene |
| SMP LMC 008 | LHA 120-N 78 | 04 50 13.14 | −69 33 56.9 | 103 | 15902464 | Mixed |
| IRAS 05063−6908 | MSX LMC 234 | 05 06 03.67 | −69 03 58.8 | 30788 | 19006720 | PAH-like |
| SMP LMC 025 | L63 124 | 05 06 23.89 | −69 03 19.3 | 20443 | 14701568 | Mixed |
| IRAS 05073−6752 | LI-LMC 463 | 05 07 13.93 | −67 48 46.7 | 40519 | 24317184 | PAH-like |
| IRAS 05092−7121 | MSX LMC 156 | 05 08 35.92 | −71 17 30.7 | 50338 | 25992448 | 21 $\mu$m (D1) |
| IRAS 05110−6616 | MSX LMC 287 | 05 11 10.65 | −66 12 53.7 | 50338 | 25992704 | 21 $\mu$m (D2) |
| IRAS 05127−6911 | LI-LMC 611 | 05 12 28.21 | −69 07 55.7 | 40519 | 24316928 | PAH-like |
| IRAS 05185−6806 | MSX LMC 346 | 05 18 28.15 | −68 04 04.0 | 30788 | 19011840 | 21 $\mu$m (B) |
| IRAS F05192−7008 | MSX LMC 390 | 05 18 45.26 | −70 05 34.5 | 40519 | 24314624 | 21 $\mu$m (D2) |
| SMP LMC 048 | LHA 120-N 1230 | 05 20 09.49 | −69 53 39.1 | 20443 | 14703104 | Mixed |
| 2MASS J05204385−6923403 | | 05 20 43.86 | −69 23 40.2 | 50338 | 27985920 | 21 $\mu$m (D2) |
| SMP LMC 051 | LHA 120-N 125 | 05 20 52.44 | −70 09 35.5 | 40519 | 22421504 | Big-11 |
| SMP LMC 056 | LHA 120-N 136 | 05 23 31.12 | −69 04 04.5 | 40519 | 22423808 | Fullerene |
| SMP LMC 058 | LHA 120-N 133 | 05 24 20.75 | −70 05 01.5 | 103 | 4950784 | Big-11 |
| IRAS Z05259−7052 | SAGE MC J052520 | 05 25 20.77 | −70 50 07.5 | 50338 | 25996032 | 21 $\mu$m (D2) |
| NGC 1978 WBT 2665 | MSX LMC 580 | 05 29 02.41 | −66 15 27.8 | 3591 | 11239680 | 21 $\mu$m (D1) |
| IRAS 05315−7145 | | 05 30 44.14 | −71 43 00.6 | 40519 | 22429440 | Red |
| SMP LMC 076 | LHA 120-N 60 | 05 33 56.10 | −67 53 09.0 | 103 | 4951296 | Big-11 |
| IRAS 05360−7121 | MSX LMC 741 | 05 35 25.85 | −71 19 56.6 | 30788 | 19008256 | 21 $\mu$m (B) |
| IRAS 05370−7019 | | 05 36 32.49 | −70 17 37.8 | 40519 | 24315648 | Big-11 |
| SMP LMC 085 | LHA 120-N 69 | 05 40 30.80 | −66 17 37.4 | 103 | 4952320 | Big-11 |
| IRAS 05413−6934 | | 05 40 54.29 | −69 33 18.6 | 40650 | 23884032 | PAH-like |
| IRAS 05495−7034 | LI-LMC 1745 | 05 49 00.01 | −70 33 22.5 | 40519 | 22447104 | Red |
| IRAS 05537−7015 | | 05 53 11.98 | −70 15 22.5 | 40519 | 27084032 | Big-11 |
| IRAS 05588−6944 | MSX LMC 1601 | 05 58 25.98 | −69 44 25.8 | 50338 | 25992960 | Big-11 |
| IRAS 06111−7023 | MSX LMC 1710 | 06 10 32.00 | −70 24 40.8 | 30788 | 19013120 | 21 $\mu$m (D1) |
| SMP LMC 099 | LHA 120-N 221 | 06 18 58.05 | −71 35 50.3 | 20443 | 14705664 | Red (PN) |

[a] We will refer to the targets by these names, shortening the names based on 2MASS and IRAS coordinates.
[b] Defined in Section 3.2; subgroups of the 21 $\mu$m group are defined in Section 3.4.

### 3.1. *Polycyclic aromatic hydrocarbons (PAHs)*

When a warm radiation field illuminates carbon-rich dust, the resulting spectrum shows emission from aromatic hydrocarbons, which are usually described as PAHs. We will adopt this nomenclature, but it is important to keep in mind that the particles responsible for the observed emission features are not necessarily the free and primarily aromatic molecules usually assumed (e.g. Allamandola et al. 1989). An alternative perspective is that the aromatic bonds responsible for the well-known IR emission features exist in an amorphous mixture with a range of structures from aliphatic to aromatic (for recent work, see Kwok & Zhang 2011; Jones 2012a,b).

In aliphatics, all electrons are localized in specific bonds, while in aromatics they are not. In aromatics, the energy of an absorbed photon is quickly distributed over all available bonds, making the PAH structure much more resistant to photodissociation in a harsh radiative environment. The electron cloud also protects aromatic structures from collisions with electrons, with greater protection for larger molecules (Micelotta et al. 2010a,b; Bocchio et al. 2012). Classic PAH emission arises from material which is dominated by aromatic bonds.

Figure 1 presents spectra of the different classes of PAH emission. The top two spectra in the figure are from the Short-Wavelength Spectrometer (SWS) on the *Infrared Space Observatory* (*ISO*), as calibrated by Sloan et al. (2003) and resampled to the IRS wavelength grid. The remainder are IRS data, and they are from the current sample, with the exception of MSX SMC 029, which was discussed by Kraemer et al. (2005). Its spectrum in Figure 1 is processed identically to the spectra in the current sample.

In the PAH model, C–C modes produce the features observed at 6.25, 7.65, and 7.85 $\mu$m. The 8.60 $\mu$m feature arises from an in-plane C–H bending mode, while the out-of-plane C–H bending modes produce features at 11.25, 12.0, and 12.7 $\mu$m, with the wavelength determined by the number of adjacent C–H bonds on the same aromatic ring. In wavelength order, these are the solo, duo, and trio modes (Allamandola et al. 1989).

Peeters et al. (2002) grouped PAH spectra into Classes

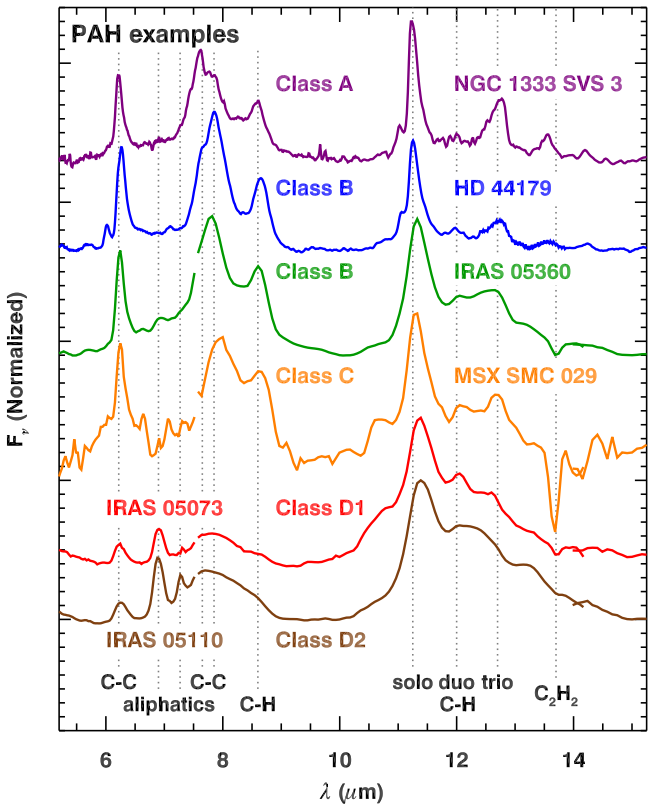


FIG. 1.— Examples of spectra showing different classes of PAH emission. The top two spectra are based on *ISO*/SWS spectra, the rest are IRS data. Of the IRS sources, all but MSX SMC 029 are in our sample. Classes D1 and D2 are defined in Section 3.4. The vertical dotted lines mark the wavelengths of aliphatic modes at 6.90 and 7.27 $\mu$m, aromatic modes at other wavelengths, and the location of the Q branch from molecular $C_2H_2$ absorption at 13.7 $\mu$m.

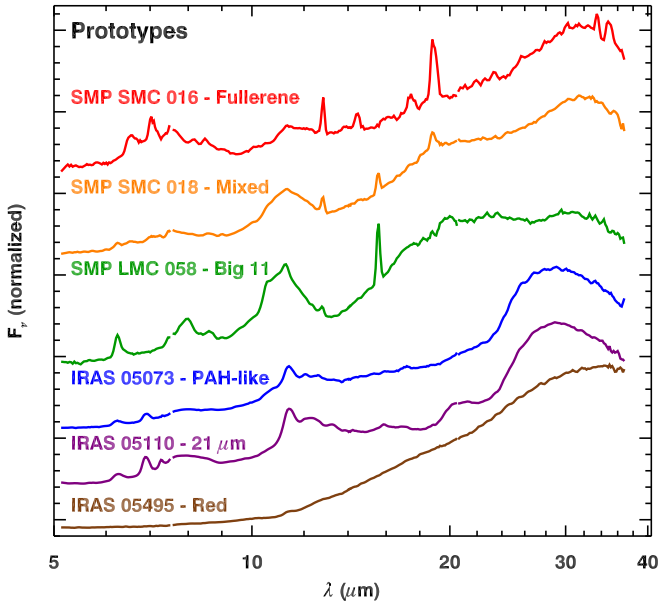


FIG. 2.— Examples of the spectral groups into which we have divided the sample of carbon-rich Magellanic post-AGB spectra.

A, B, and C, based primarily on the position of the 6.2 $\mu$m feature and the shape of the 7.7–7.9 $\mu$m complex, with the peaks shifting from blue to red in the sequence A–B–C. They noted that the different features do not always shift in unison. We will concentrate on the 7.7–7.9 $\mu$m region, which generally consists of two components with peaks ∼7.65 and 7.85 $\mu$m. The former dominates in Class A spectra, while the latter dominates in Class B. Peeters et al. (2002) found that most, but not all, PNe showed Class B PAH emission, while Class A PAH emission sources were more likely to be associated with young stellar objects.

For Class C PAH emission, the peak is further to the red. In the *ISO*/SWS sample examined by Peeters et al. (2002), only two Class C sources were present, and both were post-AGB objects. Observations with the IRS added several more Class C sources, many of which are not post-AGB objects (Sloan et al. 2007; Acke et al. 2010; Smolders et al. 2010; Evans et al. 2010). Generally Class C PAH spectra have a central wavelength beyond a limit of ∼7.9–8.0 $\mu$m (Keller et al. 2008). The PAH features at 6.2 and 11.3 $\mu$m also shift to longer wavelengths in this class.

Laboratory data show that these wavelengths shifts can arise from hydrocarbon mixtures with higher ratios of aliphatics to aromatics (Pino et al. 2008). As this ratio increases, the mixture becomes better described as hydrogenated amorphous carbon (HAC; e.g. Duley & Williams 1981; Jones et al. 1990). Class C PAHs appear to be a special case seen only when hydrocarbon material has not been as heavily photo-processed as the more typical Class A or B PAHs, either because the radiation field is less harsh, or because they have been processed for shorter periods of time (see Evans et al. 2010, for an example of the latter case).

Matsuura et al. (2014) added a new class of PAH emission seen in some post-AGB spectra, Class D, based primarily on the unusual shape to the emission in the 6–9 $\mu$m region (see also Matsuura et al. 2011). While typical PAH spectra show emission peaks in the 7.5–8 $\mu$m region and at 8.6 $\mu$m, with a definite minimum between them, in Class D PAH spectra, the region from 8 to 8.5 $\mu$m is filled in with additional emission. Class D differs from Class C, which shows a clear peak to the red of 8 $\mu$m. In Section 3.4, we show that Class D can be broken into two separate classes.

In addition to the features from aromatic hydrocarbons, aliphatic features can also appear in our spectra, most notably at 6.90 and 7.27 $\mu$m (these wavelengths are determined below in Section 3.3.2). Methyl ($CH_3$) groups produce features from asymmetric and symmetric C–H bending modes at ∼6.8 and ∼7.2 $\mu$m, respectively. Methylene ($CH_2$) groups can contribute at ∼6.8 $\mu$m with a C–H scissoring mode. Additional methylene C–H wagging and twisting modes appear at 7.6–7.7 $\mu$m, but these are buried by the strong C–C PAH modes at these wavelengths.

### 3.2. *Post-AGB spectral groups*

We have assigned each spectrum to one of several groups based on the criteria described below and explained more fully in the following sections. Figure 2 presents the prototypes for the groups, and Figures 3 to 8 plot the individual spectra in each group. We will capitalize the names of the spectral groups to avoid confusion with the use of the same words to describe individual

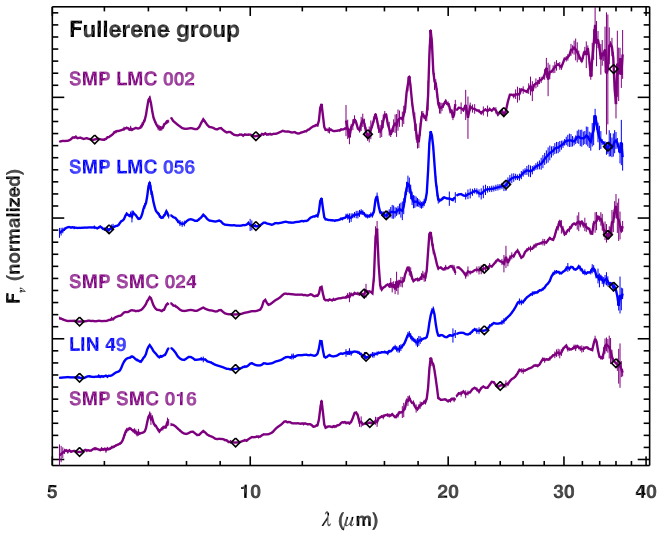


FIG. 3.— The fullerene spectra. The black diamonds mark the wavelengths through which splines were fit.

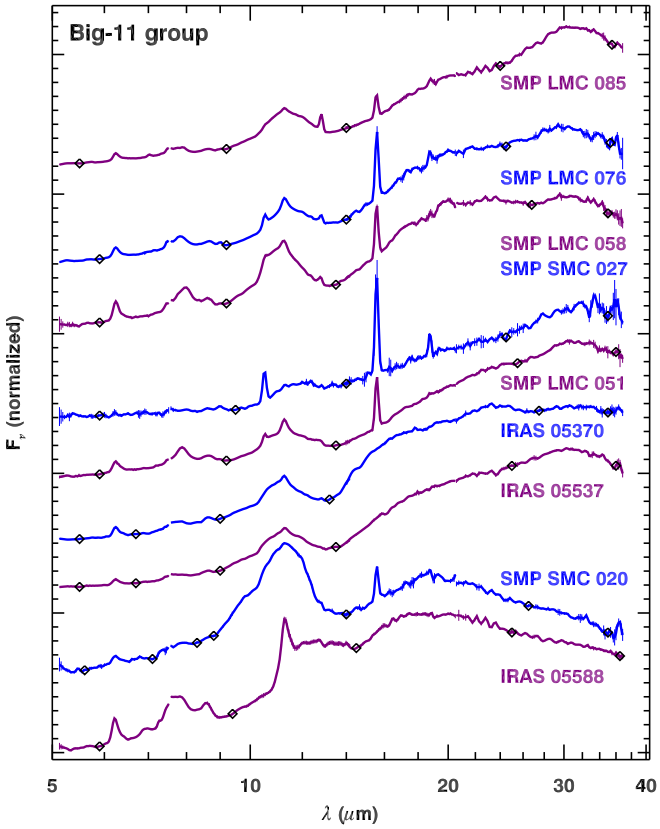


FIG. 4.— The spectra showing the big-11 feature at ∼11.3 μm and other associated features, including emission from PAHs at 6–9 μm, a shoulder at 18 μm, and often strong a strong emission at ∼30 μm. The spline points appear as black diamonds.

spectral features.[14]

The **Fullerene group** shows emission features at 17.4 and 18.9 μm. These spectra have a distinctive structure in the 6–9 μm region which includes the previously identified fullerene features at 7.03 and 8.50 μm (Cami et al. 2010) and additional features which differ from the usual 6–9 μm PAH emission profile. LIN 49 is a new identification of a fullerene source.

[14] For example, "big-11" refers to the spectral feature, while "Big-11" refers to the spectra in the group dominated by this feature.

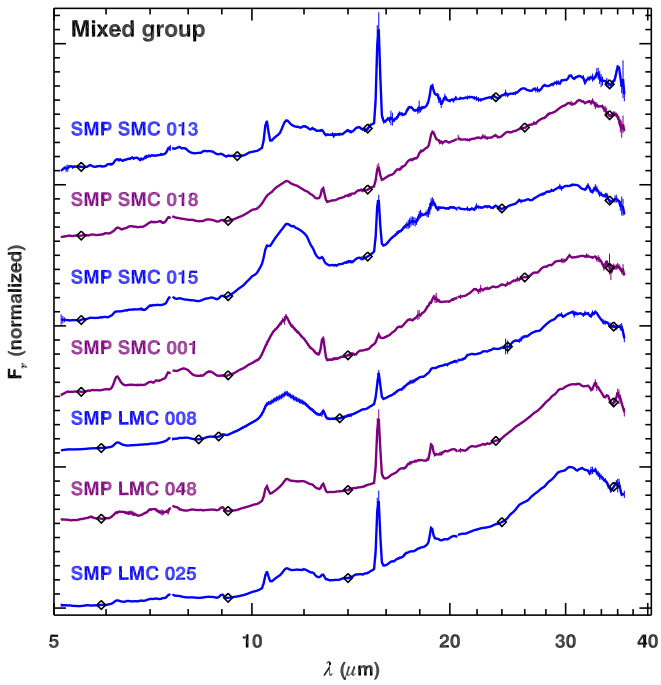


FIG. 5.— The spectra showing a mixture of fullerene features and features associated with the big-11 feature. The boundaries between these groups are unavoidably arbitrary. The black diamonds mark the spline points.

The **Big-11 group** shows a strong emission feature at ∼11 μm, which we refer to throughout this paper as the "big-11" feature. Spectra in this group also show PAH-like emission features, but no clear evidence of fullerenes. They usually also show PAH features in the 6–9 μm region and a shoulder at 18 μm from an unidentified carrier. The key discriminants for this group are (1) a lack of fullerene emission and (2) *either* a clear big-11 feature *or* a combination of a more ambiguous big-11 feature and the 18 μm shoulder.

The **Mixed group** consists of positively identified fullerene sources that show additional structure in the 6–9 μm region usually associated with PAHs. These spectra show clear distinctions from the Fullerene and Big-11 groups to either side, but all three groups represent a continuum and where one draws the line between them is somewhat arbitrary. These spectra typically show the big-11 feature and the associated shoulder at 18 μm (as do some of the Fullerene spectra), but the clear presence of fullerenes distinguishes them. Two sources, SMP LMC 008 and SMP SMC 001, are new fullerene identifications.

The **PAH-like group** shows typical PAH emission features in the 6–9 μm region and PAH-like structure in the 11–14 μm region. Our classification as PAH-like is based primarily on the unusual structure at 11–14 μm, with the relative strengths of the 12.0 and 12.7 μm features reversed, producing a triangular shape for the 11–14 μm complex. The PAH-like spectra also tend to show a broader blue wing to the 11.3 μm feature.

The **21 μm group** typically shows the family of asso-

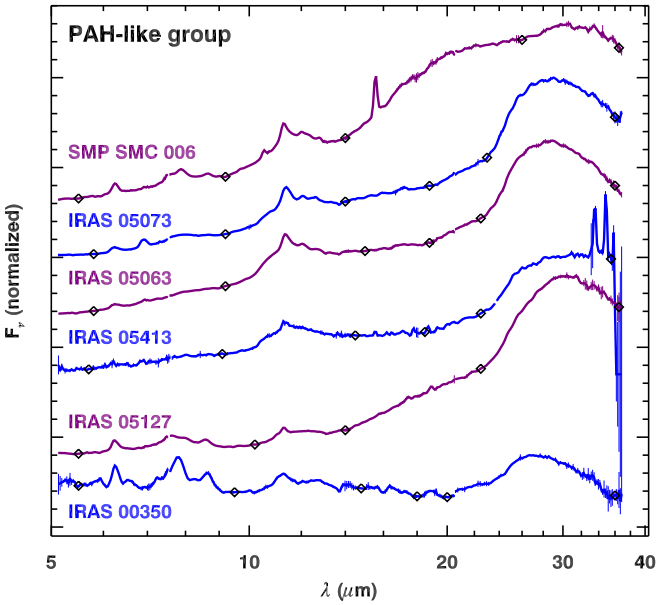


FIG. 6.— Spectra showing PAH emission at 6–9 $\mu$m and a PAH-like spectrum at 11–14 $\mu$m. The black diamonds mark the spline points.

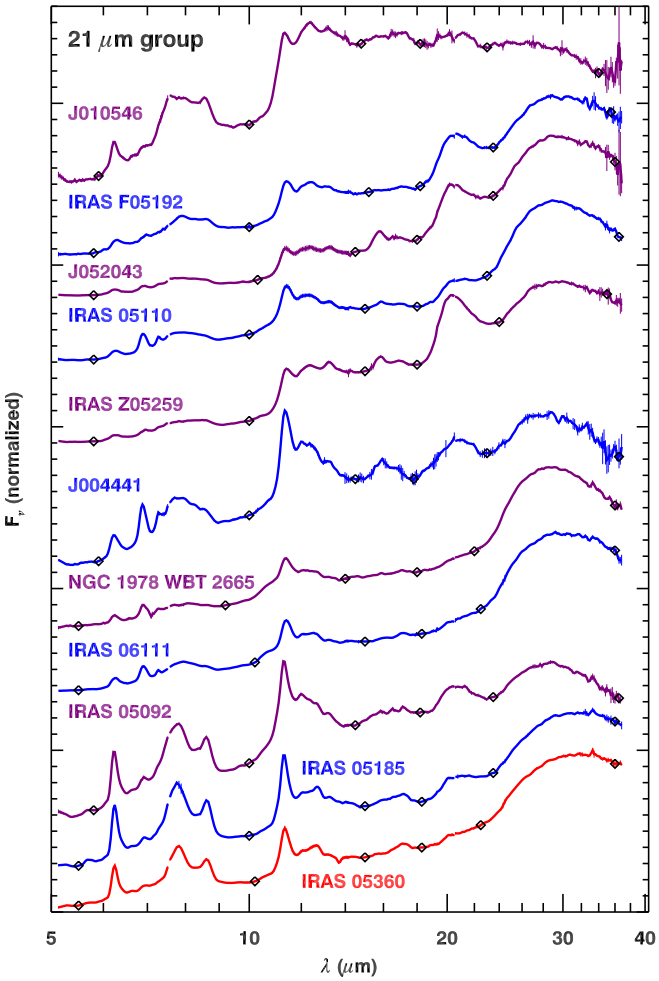


FIG. 7.— Spectra showing the 21 $\mu$m feature and associated features at 8, 11, 16, and 30 $\mu$m. Black diamonds mark the spline points. IRAS 05360 is plotted in red because it is the comparison Class B PAH spectrum in several of the following figures.

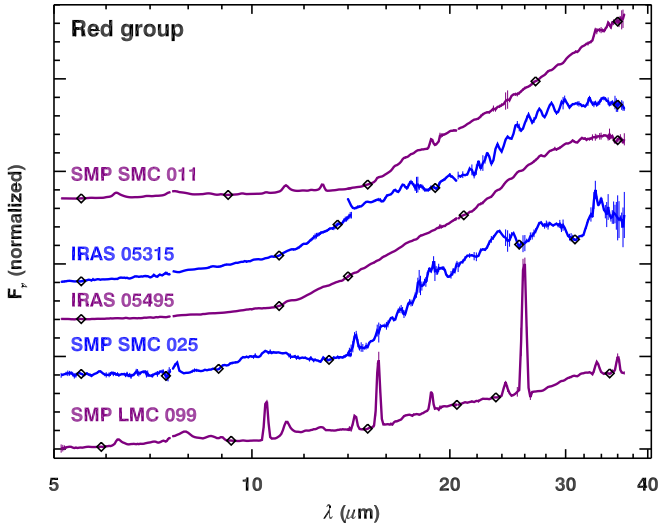


FIG. 8.— The reddest spectra in our sample. Two show little recognizable spectral structure, while one shows normal PAH emission and one shows crystalline silicate emission. The fifth spectrum is a source with fullerenes identified in its spectrum by others but not confirmed here. The spline points are marked with black diamonds.

ciated emission features at 8, 11, 16, 21, and 26–30 $\mu$m, although not all spectra show all of the features. Volk et al. (2011) analyzed many of the same spectra discussed here. Their classification of what belongs in the 21 $\mu$m group and ours do not coincide exactly, due to a combination of the improved optimal spectral extraction used here and different constraints on the classification. In some of our spectra, the 21 $\mu$m feature is ambiguous, but other related features are present (most notably NGC 1978 WBT 2665 and IRAS 0611). Table 1 includes subclassifications for the 21 $\mu$m group based on the nature of the PAH-like emission at 11–14 $\mu$m; these are defined in Section 3.4 below.

The **Red group** is the final group. The only requirement is that the spectrum show a red continuum. Most show only low-contrast features, but this group also serves as the depository for spectra which cannot be placed in other categories. One source, SMP SMC 025, shows crystalline silicate emission. SMP LMC 099 is a fullerene candidate (García-Hernández et al. 2011), although we do not find fullerenes in its spectrum.

### 3.3. *Separating the Fullerene, Mixed, and Big-11 groups*

The $C_{60}$ molecule produces four strong emission features, at 7.0, 8.5, 17.4 and 18.9 $\mu$m (Cami et al. 2010). The spectra containing fullerenes and the big-11 feature represent a continuum, with many spectra exhibiting characteristics of both, making it necessary to develop a straightforward means of recognizing when fullerenes are present. Appendix 1 describes in detail our analysis of the spectral features. In this section, we focus on the results.

#### 3.3.1. *Fullerene at 17–19 $\mu$m*

Figures 9 and 10 present the (spline-removed) 17–19 $\mu$m spectra of sources in the Fullerene, Mixed, and Big-11 groups, as well as the fullerene candidate SMP LMC 099. This region includes the fullerene features at

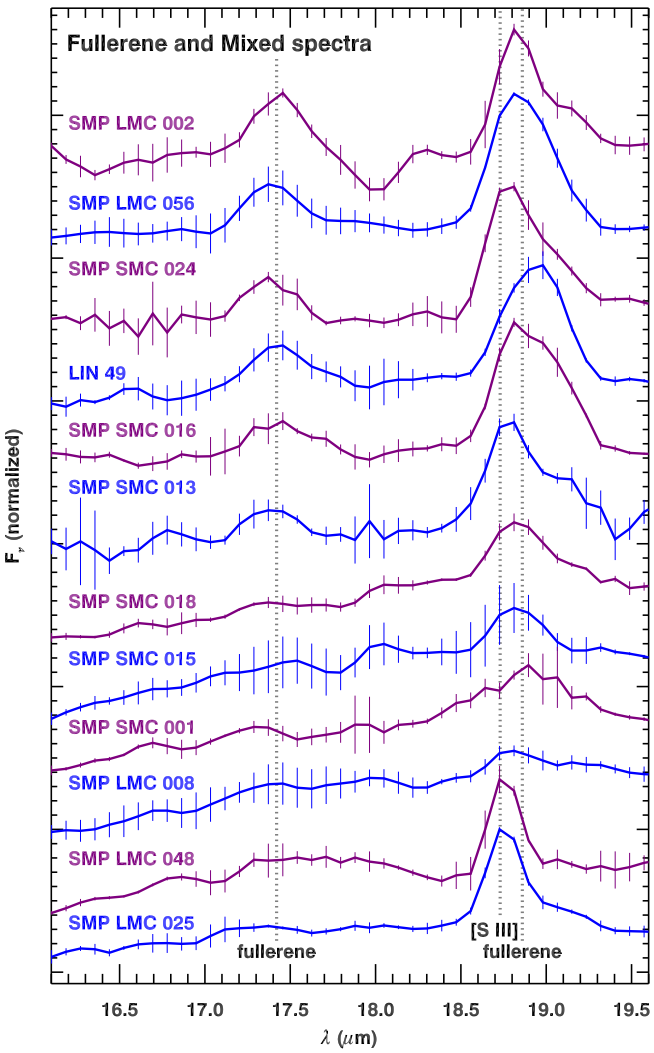


FIG. 9.— The 16–20 $\mu$m region of the spectra showing evidence for fullerene features. The vertical dotted lines are at 17.41 and 18.88, the nominal positions of the fullerene features in our data, and 18.71 $\mu$m, the nominal position of the forbidden lines from [S III]. These spectra have had splines fitted and removed.

17.4 and 18.9 $\mu$m. Many of these spectra have the [S III] line at 18.71 $\mu$m, which, at the low resolution of LL2 ($\lambda/\Delta\lambda$ = 130 at 19 $\mu$m), is blended with the 18.9 $\mu$m fullerene feature. The 17.4 $\mu$m feature is weaker, and for spectra with low signal/noise ratios (SNRs), the 18.9 $\mu$m feature is the better test, if we can address the blending problem.

Appendix 1.1 describes our analysis of this spectral region. Fitting gaussians to the 18.8 $\mu$m blend separates those spectra dominated by [S III] from those dominated by fullerenes, as Figure 11 shows. The widths and positions fall into two quadrants. For most cases, it is not necessary to rely on data from SH or other higher-resolution spectrometers. All of the spectra with $\lambda_0 >$ 18.80 $\mu$m have a FWHM $>$ 0.3 $\mu$m, and in each case, we positively identify fullerenes in the spectrum. The spectra with $\lambda_0 <$ 18.80 $\mu$m have FWHM $<$ 0.3 $\mu$m. Spectra in this quadrant include some Mixed and Big-11 spectra, but all of these are shifted up and to the right of the PNe, indicating that some fullerenes may be blended with the [S III] line.

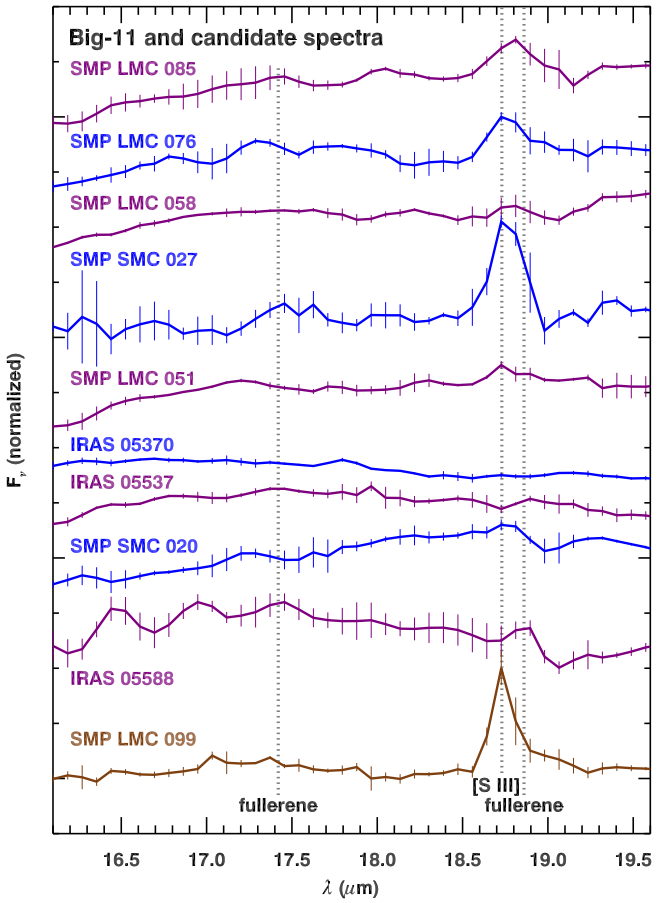


FIG. 10.— The 16–20 $\mu$m region of the spectra in the Big-11 group, along with SMP LMC 099, which shows [S III] but no fullerenes. The vertical dotted lines are as defined for Fig. 9. These spectra have had splines fitted and removed.

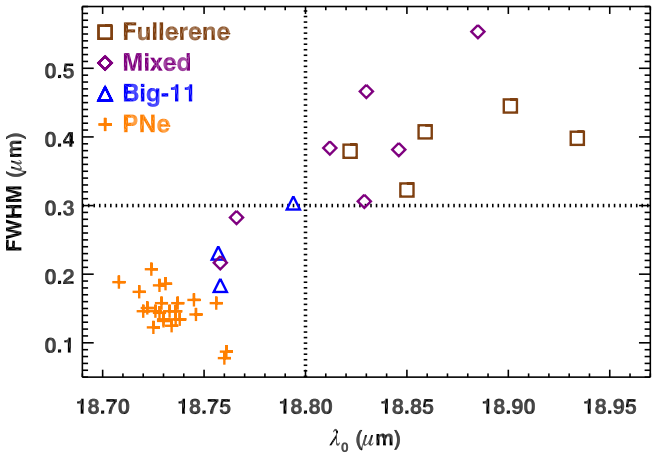


FIG. 11.— Width of the 18.7–18.9 $\mu$m feature vs. wavelength for the Fullerene, Mixed, and Big-11 spectra, as well as a control sample of planetary nebulae. The data plotted are based on fitted gaussians and differ from the data in Tables 11 and 12. Data in the lower left quadrant are from [S III] lines, while the upper right arises from fullerenes.

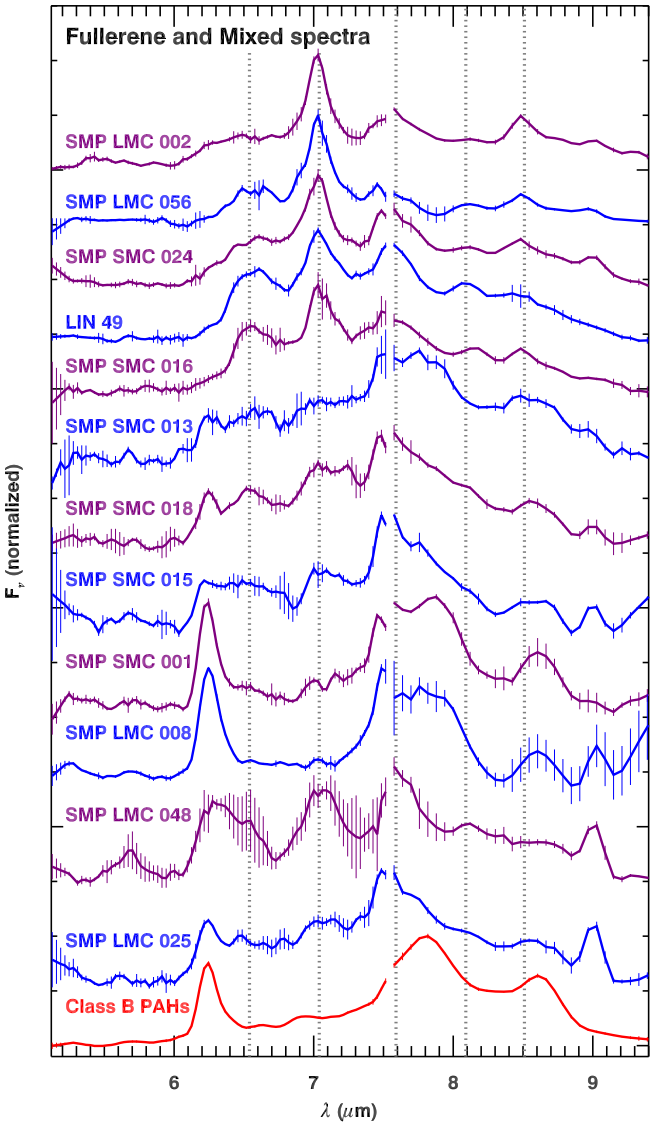


FIG. 12.— The 6–9 $\mu$m emission complex in the spectra showing contributions from fullerene features. The first five spectra are in the Fullerene group, and SMP SMC 013 is the first of the Mixed group. The bottom comparison spectrum of Class B PAHs is the source IRAS 05360. The vertical dotted lines are at 6.54, 7.04, 7.59, 8.09, and 8.51 $\mu$m, marking features associated with fullerenes. All spectra have had splines fitted and removed.

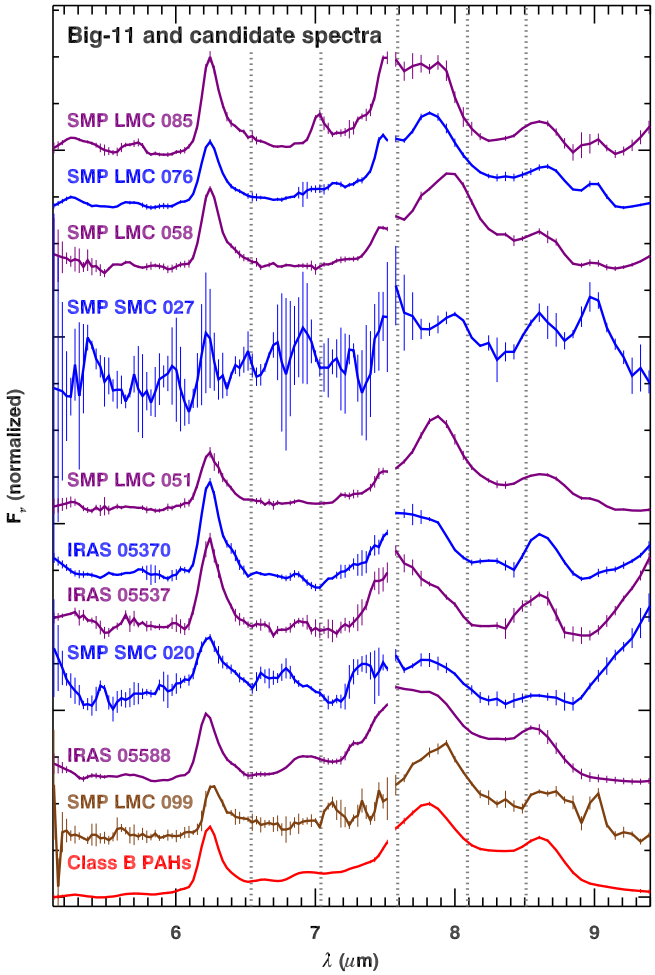


FIG. 13.— The 6–9 $\mu$m emission complex of the Big-11 spectra and SMP LMC 099. The comparison spectrum and the vertical dotted lines are as defined for Fig. 12. The spectra have had splines fitted and removed. Some of the spectra are climbing at the red edge due to the big-11 feature.

The weaker 17.4 $\mu$m feature can help validate the presence of fullerenes in all of the sources in the Fullerene group. PAHs can also produce a feature at 17.4 $\mu$m (Werner et al. 2004b), but it is usually accompanied by a stronger PAH feature at 16.4 $\mu$m (Sellgren et al. 2010) which is not apparent in Figures 9 and 10. A greater problem is the general weakness of the 17.4 $\mu$m feature; it is detected unambiguously in only one third of the Mixed and Big-11 spectra. Fortunately, the 6–9 $\mu$m region can clarify the nature of the spectra.

### 3.3.2. *Fullerene and PAHs in the 6–9 $\mu$m region*

Figure 12 presents the 6–9 $\mu$m spectra of the fullerene candidates identified in the previous section. This spectral region allows an independent assessment of the fullerene properties. Cami et al. (2010) identified two features from $C_{60}$ in this wavelength region, at 7.0 and 8.5 $\mu$m. Unfortunately, the former overlaps the [Ar II] line at 6.99 $\mu$m, and the latter is close to the in-plane C–H bending mode from PAHs at 8.6 $\mu$m. Our spectra also include features centered at 6.5 and 7.6 $\mu$m, and in some cases, a weaker feature ∼8.1 $\mu$m.

Berné et al. (2013) recently identified a series of related features in spectra from the reflection nebula NGC 7023 at 6.4, 7.1, and 8.2 $\mu$m, which they attributed to fullerene cations ($C_{60}^{+}$). The cation features at 6.4 and 8.2 $\mu$m are close to the 6.5 and 8.1 $\mu$m features seen in our Magellanic sample. The 7.1 $\mu$m cation feature, if it appears in our spectra, is blended with the 7.0 $\mu$m feature from neutral fullerenes (and with [Ar II]).

We also see a feature at 7.6 $\mu$m in the fullerene spectra, but it requires more caution because it is near the complex of hydrogen recombination lines which includes Pfund $\alpha$ at 7.46 $\mu$m and the Humphreys $\beta$ and 11–7 transitions at 7.50 $\mu$m. These sources can show forbidden-line emission from the ionized region, as the presence of the [Ar III] line at 8.99 $\mu$m in some spectra attests, and it follows that hydrogen emission might also be present. Nonetheless, we suspect that the 7.6 $\mu$m feature may be related to the 6.5 $\mu$m feature, because both appear to-

TABLE 2
Central wavelengths of 6–9 $\mu$m features

| Feature | $<\lambda_C>$ ($\mu$m) |
|---|---|
| 6.2 $\mu$m PAH | 6.25 ± 0.02 |
| 6.9 $\mu$m aliphatic | 6.90 ± 0.03 |
| 7.3 $\mu$m aliphatic | 7.27 ± 0.02 |
| 8.6 $\mu$m PAH | 8.60 ± 0.02 |
| 7–9 $\mu$m base PAH feature | 7.78 ± 0.12 |
| 6.5 $\mu$m fullerene-related | 6.54 ± 0.01 |
| 7.0 $\mu$m fullerene | 7.04 ± 0.01 |
| 7.6 $\mu$m fullerene-related | 7.59 ± 0.02 |
| 8.1 $\mu$m fullerene-related | 8.10 ± 0.02 |
| 8.5 $\mu$m fullerene | 8.51 ± 0.01 |

gether in spectra where [Ar III] and other emission lines are weak.

The first five spectra in Figure 12 show fullerenes, but no PAH emission. The remaining spectra show some evidence of PAH emission, as do all of the spectra in Figure 13, which includes the Big-11 spectra and the fullerene candidate SMP LMC 099. To aid our efforts to disentangle PAHs and fullerenes and characterize the features observed, we have extracted central wavelengths and integrated feature strengths as described in Appendix 1.2.

Table 2 gives the mean central wavelengths ($\lambda_C$) for the various fullerene-related, PAH, and aliphatic features, based on the spectra which showed a given feature at a strength of 2.5 $\sigma$ or more. For the PAH features, we excluded the Fullerene spectra, but considered all other detections. For the aliphatic features, we considered the detections listed in Appendix 1.2.

Three of the fullerene-related features are more easily separable from other features. We detected the 6.5 $\mu$m feature unambiguously in only five spectra: four of the Fullerene group and one of the Mixed group. Nine spectra contain an emission feature at 7.0 $\mu$m that could arise from fullerenes or [Ar II]: five of the Fullerene group, and four of the Mixed. We only detect the 8.1 $\mu$m feature at 2.5 $\sigma$ or better in three spectra. The fullerene-related features at 7.6 and 8.5 $\mu$m require some care, due to overlap with PAH features.

Most of the spectra show a tentative detection of a feature at 7.6 $\mu$m, but the majority are really PAHs. We find that four of the Fullerene spectra, five of the Mixed spectra, and even two of the Big-11 spectra contain a 7.6 $\mu$m feature with consistent central wavelengths. These spectra give $<\lambda_C> = 7.59 \pm 0.02$ $\mu$m. A central wavelength of 7.62 $\mu$m appears to be the boundary between a fullerene-related and a PAH feature. A central wavelength of 7.59 $\mu$m is 0.14 $\mu$m from the position of the Pfund-$\alpha$ line, giving us some confidence that we are observing a distinct feature.

The 8.5 $\mu$m fullerene feature can be blended with the 8.6 $\mu$m in-plane C–H bending mode from PAHs, but the central wavelength can distinguish them. The five Fullerene spectra with a feature centered at ∼8.5 $\mu$m give $<\lambda_C> = 8.51 \pm 0.01$ $\mu$m, while the 25 other spectra with a feature in this vicinity have $<\lambda_C> = 8.61 \pm 0.02$ $\mu$m. The latter feature is from PAHs.

In our spectra, the 7.0 $\mu$m fullerene feature appears at 7.04 $\mu$m, compared to 6.99 $\mu$m for [Ar II]. Most of the spectra with a 7.0 $\mu$m feature also have [Ne II] lines at 12.8 $\mu$m, indicating that some contamination from [Ar II] is likely, but the shift away from 6.99 $\mu$m shows that fullerenes must be contributing. The shift in fullerene emission from 7.0 $\mu$m to a longer wavelength could be a temperature effect. From 0 K to 1000 K, the $C_{60}$ feature moves from 6.97 to 7.11 $\mu$m, and the $C_{70}$ feature moves from 6.98 to 7.08 $\mu$m (Nemes et al. 1994). The observed shift might also arise from the presence of some fullerene cations. However, the central wavelengths of the other putative cation features do not align particularly well with what Berné et al. (2013) reported for them: 6.54 vs. 6.40 $\mu$m and 8.10 vs. 8.23 $\mu$m.

#### 3.3.3. *Fullerene classification*

Sources in both the Fullerene and Mixed groups should be treated as positive fullerene identifications. Three of these identifications are new: LIN 49 in the Fullerene group and SMP LMC 008 and SMP SMC 001 in the Mixed group.

The first five spectra in Figure 12 show unambiguous fullerene features and no PAH emission and therefore belong to the Fullerene group. The remaining spectra in the figure show a mixture of fullerene-related and PAH features which puts them in the Mixed group. SMP SMC 013 is the transition between the two groups. It clearly has fullerene features at 17.4 and 18.9 $\mu$m, but the 6–9 $\mu$m structure is more ambiguous, with definite PAH features at 6.2 $\mu$m and ∼7.8 $\mu$m alongside fullerene-related features at 6.5 and 7.0 $\mu$m.

The bottom spectrum (of IRAS 05360) in Figure 12 is an example of a Class B PAH spectrum typical for more evolved PNe and a good comparison for the features visible in the Mixed spectra. All of the Mixed spectra show fullerene-like structure at 7.0 and 7.6 $\mu$m, and all but SMP SMC 001 and SMP LMC 008 have a 6.5 $\mu$m feature. While the individual features are hard to discern in SMP LMC 025, the spectrum shows a clear excess between the 6.2 and 7.7–7.9 $\mu$m PAH features compared to a typical PAH spectrum.

Figure 13 plots spectra from the Big-11 group as well as SMP LMC 099. None show convincing evidence of fullerenes. The classification of the top spectrum, SMP LMC 085, is arguable, as it does show some evidence of features at 7.0 and 7.6 $\mu$m. However, it is lacking the plateau from 6.2 to 7.6 $\mu$m and a clear detection of fullerenes at 17.4 or 18.9 $\mu$m. The spectrum of SMP LMC 076 might show a 7.6 $\mu$m feature, but it shows none of the other fullerene features expected in this wavelength region. The line at ∼18.8 $\mu$m looks more like [S III] than fullerenes.

We are unable to confirm previous identifications of fullerenes in the spectra of SMP SMC 020, 027, and SMP LMC 099 (García-Hernández et al. 2011). The structure in the 6–9 $\mu$m region is not consistent with fullerenes, with SMP SMC 020 showing spectral structure close to PAHs. SMP SMC 020 also shows no clear feature at either 17.4 or 18.9 $\mu$m. SMP SMC 027 has what appears to be a fullerene feature at 17.4 $\mu$m, but the structure at ∼18.8 $\mu$m matches [S III], not fullerenes. In SMP LMC 099, the 6–9 $\mu$m spectrum looks like Class B PAHs, the feature at ∼18.8 $\mu$m is clearly [S III], and no recognizable feature appears at 17.4 $\mu$m.

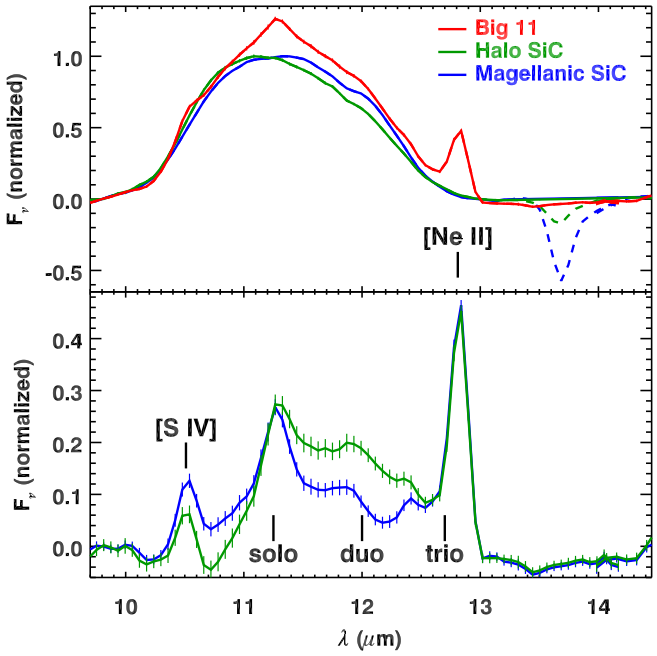


FIG. 14.— The average big-11 feature compared to SiC profiles from Magellanic carbon stars and carbon stars in the Galactic Halo (top panel). The dashed lines show the comparison profiles before removing the $C_2H_2$ absorption band at 13.7 $\mu$m by interpolating a line from the data to either side. The bottom panel shows the residual spectra after subtracting the two comparison profiles from the big-11 feature.

#### 3.3.4. *The nature of the big-11 feature*

The big-11 feature dominates the spectra not just of the Big-11 group, but also the Mixed group. It is clearly present in some of the Fullerene spectra as well. This feature is usually accompanied by a broad feature at ∼18 $\mu$m, which in the redder spectra appears as an inflection or shoulder on a continuum rising to longer wavelengths. Many of these spectra also show a feature in the 26–30 $\mu$m vicinity.

Bernard-Salas et al. (2009) attributed the big-11 feature primarily to SiC. We investigated by comparing the big-11 feature to two coadded SiC profiles from separate control groups. The first group consists of 26 spectra of carbon stars from the LMC and five from the SMC, all with good SNRs and well-defined SiC features.[15] The second group includes six carbon stars in the Galactic Halo.[16] All of these spectra were observed and reduced as described in Section 2.2, except that the brightness of the four Halo spectra made optimal extraction unnecessary.

To generate an average big-11 profile, we combined six spectra: SMP SMC 001, 015, 018, and 020, along with SMP LMC 008 and 085. These sources include the four Mixed spectra with the least contamination from [S IV] at 10.52 $\mu$m, and the two spectra from the Big-11 group with the least structure from [S IV] and PAHs. For the average big-11 profile and the two SiC profiles, a continuum was spline-fitted and removed to isolate the profiles, which were then normalized and averaged. Both of the comparison SiC profiles also show absorption at 13.7 $\mu$m from $C_2H_2$, which we removed from the data by replacing the affected wavelengths with a line interpolated from data to either side. Our post-AGB spectra tend to show weak $C_2H_2$ absorption or none at all.

Figure 14 compares the three profiles (top panel). We have normalized the big-11 profile to 1.0 at 10.95 $\mu$m to align with the other two. Both of the comparison SiC profiles have a FWHM of 0.66 $\mu$m. The central wavelength is 11.29 $\mu$m for the Magellanic profile and 11.22 $\mu$m for the Halo profile. The differences in the shape of the profile between the two are consistent with the wide range of observed positions and profiles in published samples (e.g. Speck et al. 2005; Sloan et al. 2006).

Figure 14 also plots the residuals after subtracting the two comparison SiC profiles from the average big-11 feature (bottom panel). The residual spectrum is a combination of [S IV] and [Ne II] lines at 10.52 and 12.81 $\mu$m, respectively, and PAH-like emission in between, with features or structure apparent at ∼11.3, ∼11.9, and∼12.4 $\mu$m. The first two are close to the positions of the solo and duo out-of-plane C–H bending modes. The position of the feature ∼11.9 $\mu$m depends on the assumed underlying shape of the SiC feature, and it is reasonable to assume that this is in fact the 12.0 $\mu$m duo mode. The third is in the vicinity of the $H_2$ 0–0 S(2) transition at 12.28 $\mu$m, but $H_2$ emission does not appear at other wavelengths in these spectra and can be ruled out. A more likely culprit is the Humphreys $\alpha$ transition at 12.37 $\mu$m. The presence of a strong [Ne II] line prevents us from making any statements about the trio mode at 12.7 $\mu$m, but the duo mode appears to be unusually strong compared to the solo mode, making this residual emission look much like the PAH emission in the PAH-like group.

If we ignore the [S IV] and [Ne II] lines (by replacing the affected data as we did with the $C_2H_2$ line), then SiC emission contributes 88% of the total big-11 feature. This analysis confirms the description by Bernard-Salas et al. (2009) of the feature as primarily from SiC, and it contradicts a recent claim to the contrary by Sloan et al. (2012), who based their preliminary conclusion on a comparison of too few spectra. We will address abundance issues raised by such a strong SiC feature in Section 5.2 below.

### 3.4. *PAH classification*

To classify the spectra in our sample into the PAH classes described in Section 3.1, we have examined both the 6–9 and 11–14 $\mu$m regions. Table 3 presents the results for both wavelength regimes. Where the emission at 11–14 $\mu$m is not the new Classes D1 or D2 (defined below in Section 3.4.2), we have assigned a class consistent with the shape at 6–9 $\mu$m, because Class A and B PAH emission are indistinguishable at 11–14 $\mu$m. The following two sections describe the treatment of the two wavelength regimes.

#### 3.4.1. *Spectral properties at 6–9 $\mu$m*

Variations in the spectra in the 6–9 $\mu$m region can distinguish the different classes of PAH emission. Class A

[15] The sample includes four spectra published by Sloan et al. (2006), 12 by Zijlstra et al. (2006), four by Buchanan et al. (2006), one each by Lagadec et al. (2007) and Leisenring et al. (2008), and nine unpublished spectra from program 30788 (P.I. R. Sahai).

[16] Two in the line of sight toward the Sgr Dwarf Spheroidal (Lagadec et al. 2009) and four in the nearby Halo (Lagadec et al. 2012).

TABLE 3
PAH CLASSIFICATIONS

| Target | Group | 6–9 $\mu$m | 11–14 $\mu$m[a] |
|---|---|---|---|
| SMP SMC 024 | Fullerene | ··· | (D1) |
| SMP SMC 016 | Fullerene | ··· | (D1) |
| SMP SMC 013 | Mixed | ··· | (D1) |
| SMP SMC 018 | Mixed | ··· | (D1) |
| SMP SMC 015 | Mixed | ··· | (D1) |
| SMP SMC 001 | Mixed | ··· | (D1) |
| SMP SMC 008 | Mixed | ··· | (D1) |
| SMP SMC 048 | Mixed | ··· | (D1) |
| SMP SMC 025 | Mixed | ··· | (D1) |
| SMP LMC 085 | Big-11 | A: | (D1) |
| SMP LMC 076 | Big-11 | B | (D1) |
| SMP LMC 058 | Big-11 | B | (D1) |
| SMP SMC 027 | Big-11 | ? | (D1) |
| SMP LMC 051 | Big-11 | B | (D1) |
| IRAS 05370 | Big-11 | A | (D1) |
| IRAS 05537 | Big-11 | A | (D1) |
| SMP SMC 020 | Big-11 | B | (D1) |
| IRAS 05588 | Big-11 | A | A |
| SMP SMC 006 | PAH-like | B | D1 |
| IRAS 05073 | PAH-like | D | D1 |
| IRAS 05063 | PAH-like | D | D1 |
| IRAS 05413 | PAH-like | ? | D1 |
| IRAS 05127 | PAH-like | A | D1 |
| IRAS 00350 | PAH-like | B | D1 |
| J010546 | 21 $\mu$m | D | D2 |
| IRAS F05192 | 21 $\mu$m | D | D2 |
| J052043 | 21 $\mu$m | D | D2 |
| IRAS 05110 | 21 $\mu$m | D | D2 |
| IRAS Z05259 | 21 $\mu$m | D | D2 |
| J004441 | 21 $\mu$m | D | D2 |
| NGC 1978 WBT 2665 | 21 $\mu$m | D | D1 |
| IRAS 06111 | 21 $\mu$m | D | D1 |
| IRAS 05092 | 21 $\mu$m | B | D1 |
| IRAS 05185 | 21 $\mu$m | B | B |
| IRAS 05360 | 21 $\mu$m | B | B |
| SMP LMC 099 | Red | B | B |
| SMP SMC 011 | Red | A | A |

[a] Classifications in parentheses are residuals of the big-11 feature and assumed to be D1.

PAHs are stonger at 7.65 $\mu$m, Class B PAHs are stronger at 7.85 $\mu$m, and Class C PAHs have feature with a central wavelength to the red of ∼8.0 $\mu$m. Only two spectra in our sample are clearly past that limit, both Red spectra with low-contrast spectral structure that may not be PAH emission. A third source, SMP LMC 058, is at the limit, and it resembles more the transitional "B/C" class defined by Keller et al. (2008) and seen in many Herbig AeBe stars. It is interesting that even though the present sample is composed of carbon-rich post-AGB objects, and the two original Class C PAH spectra were both carbon-rich post-AGB objects (Peeters et al. 2002), none of the spectra in our sample are good examples of Class C PAHs.

We excluded the Fullerene and Mixed groups from the PAH classification, because the presence of the fullerene-related feature at 7.6 $\mu$m can mimic the central wavelength of the Class A spectrum (see Figure 12). While most of the spectra in the Big-11 group appear to be Class A, we cannot rule out low levels of fullerenes (see Figure 13). Only three of the Big-11 spectra are unambiguously Class A.

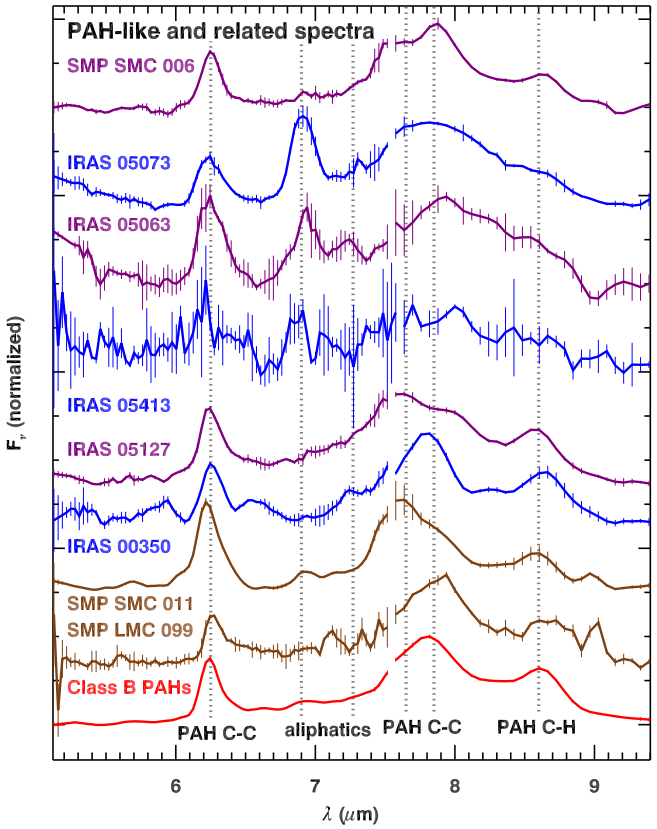


FIG. 15.— The 6–9 $\mu$m emission complex in the six spectra showing PAH-like features, two of the red spectra, and a PAH comparison spectrum (IRAS 05360). The vertical dotted lines mark the PAH and aliphatic features at 6.25, 6.90, 7.27, 7.65, 7.85, and 8.60 $\mu$m. All spectra have had splines fitted and removed.

Figure 15 presents the 6–9 $\mu$m region of the PAH-like spectra, along with three other spectra. Two spectra are missing the usual minimum between the 7.85 and 8.6 $\mu$m features and therefore belong to Class D as defined by Matsuura et al. (2014). These two spectra also have the strongest aliphatic features at 6.9 $\mu$m in this group.

Figure 16 shows the 21 $\mu$m sources in the 6–9 $\mu$m region. All except the bottom three show the Class D PAH profile. The remaining spectra are consistent with Class B PAH emission. All of the spectra with a strong aliphatic feature at 6.9 $\mu$m are associated with Class D profiles at 6–9 $\mu$m, although the inverse is not true. All of the 21 $\mu$m spectra show some aliphatic 6.9 $\mu$m emission, even the Class B spectra.

The aliphatic features can appear in spectra with seeming disregard for the class of the PAH emission. For example, the 6.9 $\mu$m feature is clearly present (though weak) in the spectrum of SMP SMC 011, a Class A source (Figure 15). It also appears in the spectrum of IRAS 05588, a Big-11 source, and possibly in SMP SMC 020 as well (Figure 13).

### 3.4.2. *Spectral properties at 11–14 $\mu$m*

Figures 17 and 18 focus on the 11–14 $\mu$m region in the spectra of the Fullerene, Mixed, and Big-11 groups. The big-11 feature usually appears in spectra in the Fullerene and Mixed groups, because assignment to those groups was based on the 17–19 and 6–9 $\mu$m regions, not the 11–14 $\mu$m region. Some spectra, most notably SMP

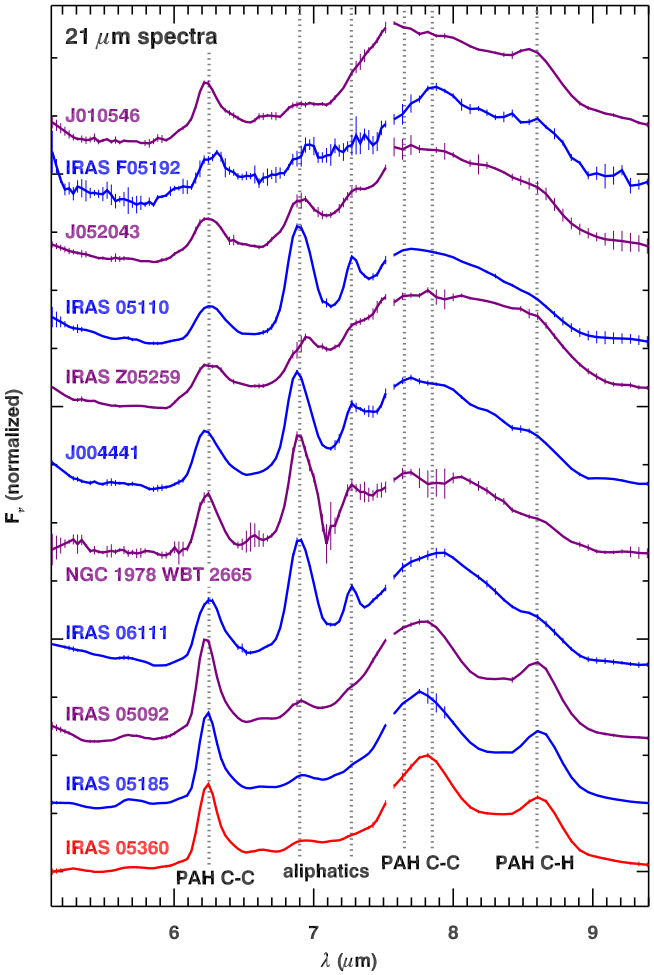


FIG. 16.— The 6–9 $\mu$m region of the spectra with 21 $\mu$m and related emission features. The vertical dotted lines and the comparison spectrum are as defined in Figure 15.

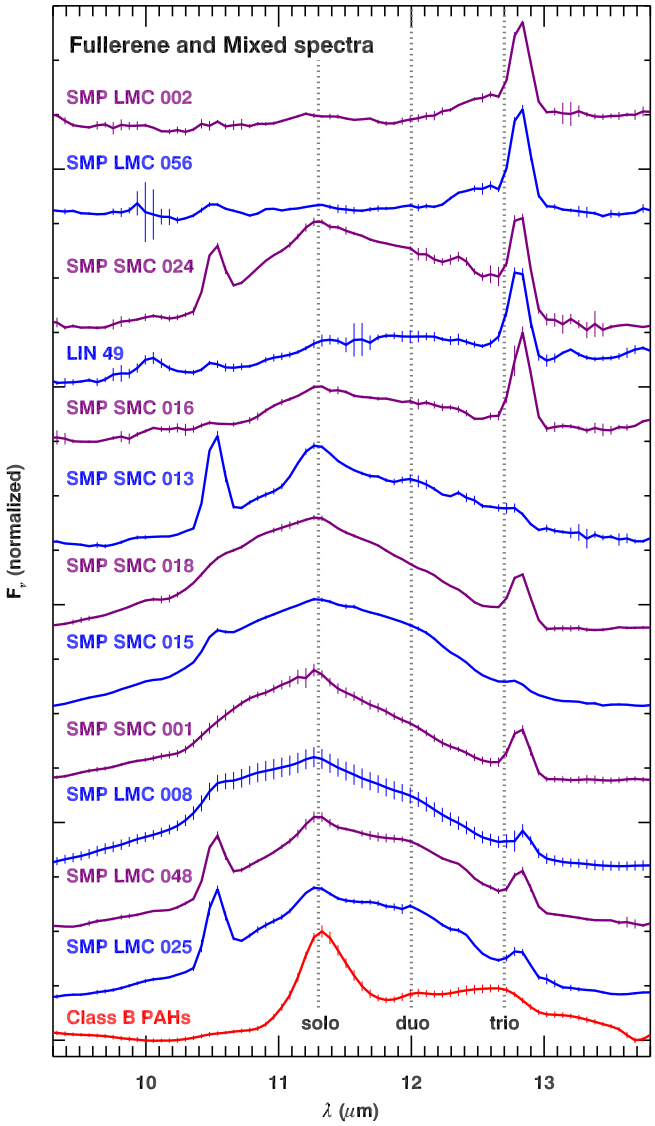


FIG. 17.— The 11–14 $\mu$m region of the spectra classified as Fullerene or Mixed. The vertical dotted lines mark the nominal positions of the PAH modes from solo, duo, and trio out-of-plane C–H bending at 11.3, 12.0, and 12.7 $\mu$m, respectively. The comparison Class B PAH spectrum is of IRAS 05360. Some of the spectra have emission lines from [S IV] and [Ne II] at 10.52 and 12.81 $\mu$m, respectively.

SMC 013, show inflections at 11.3 and 12.0 $\mu$m from a stronger contribution from PAHs.

Figure 18 reveals the wide variation present in the profile of the big-11 feature, with a range of relative contributions between SiC and PAHs. IRAS 05588, near the bottom, shows the least contaminated PAH spectrum, but with a slight reversal in the relative strength of 12.0 and 12.7 $\mu$m features. This spectrum belongs to the Big-11 group because of the strong shoulder at 18 $\mu$m (Figure 4).

As noted in Section 3.3.4, the SiC dust feature dominates the big-11 feature, and the position and shape of the SiC feature can vary significantly from one carbon star to the next. Because the structure of the small PAH residual depends on the assumed SiC profile, we did not classify the PAH contributions in the individual spectra with big-11 features. Instead, we assume that the PAH contributions resemble the residual in Figure 14.

Figure 19 illustrates how the PAH-like spectra usually show an enhanced 12.0 $\mu$m feature, like the residual PAH spectrum in the big-11 profile. We identify this as the Class D1 PAH profile. It also has a broad blue wing to the 11.3 $\mu$m feature not apparent in the three comparison spectra plotted at the bottom. This blue excess at 10.5–11.0 $\mu$m could arise from SiC. IRAS 00350 is the only PAH-like spectrum with a 12.0 $\mu$m feature that is weaker than the 12.7 $\mu$m feature, but it has a strong blue excess.

Figure 20 also reveals deviations from the usual PAH profile at 11–14 $\mu$m in most of the 21 $\mu$m sources. Only the bottom two spectra show a normal profile. The remaining spectra can be separated into two distinct groups. In the top six, the positions of the components at 11–14 $\mu$m have shifted to longer wavelengths, with broad emission components at ∼12.4 and 13.2 $\mu$m, and the shoulder at 10.5 $\mu$m is missing. We label this profile as Class D2. The remaining three sources show intermediate spectra with PAH-like profiles with a stronger feature at 12.0 $\mu$m compared to 12.7 $\mu$m and, in two of the three cases, a blue shoulder (i.e. Class D1).

Thus we have two unusual profiles apparent in the PAH-like and 21 $\mu$m groups. Class D1 has components

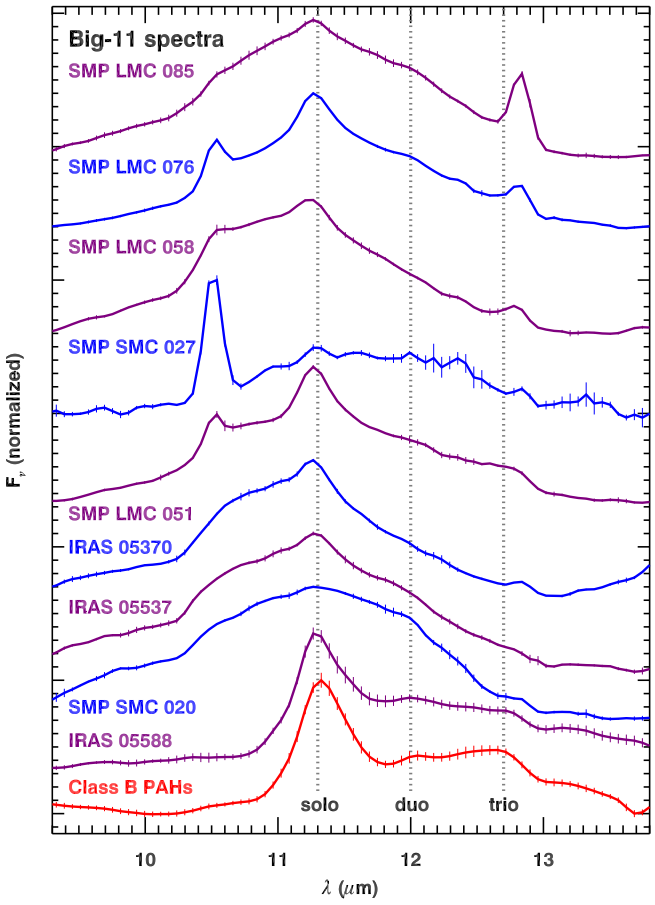


FIG. 18.— The 11–14 $\mu$m region for the Big-11 spectra. The vertical lines and comparison data are as described in Figure 17.

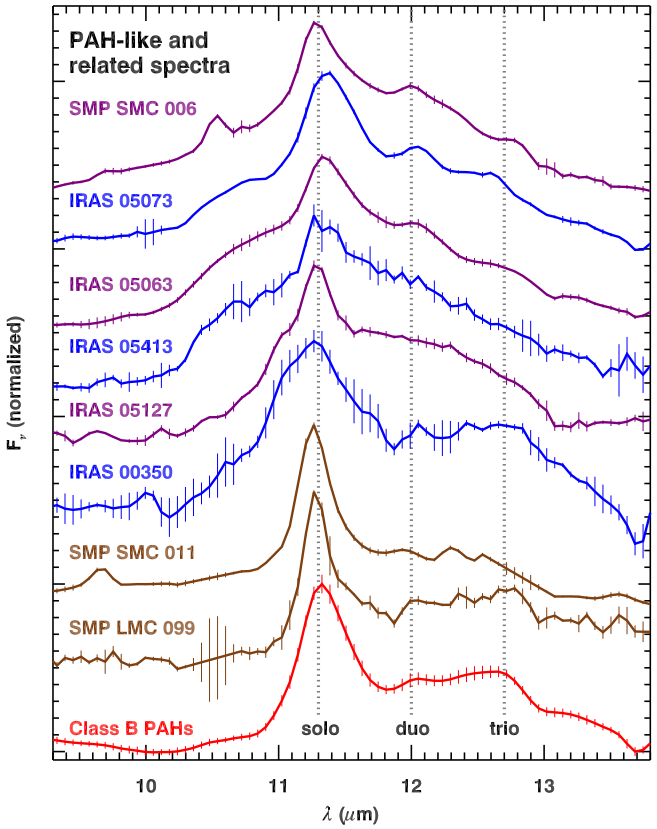


FIG. 19.— The 11–14 $\mu$m region for the spectra defined as PAH-like, along with two Red spectra showing more typical PAH features: SMP SMC 011 and SMP LMC 099. For clarity, the [S IV] line at 10.52 $\mu$m has been removed from the spectra of both of these sources, and for SMP SMC 011, the [Ne II] line at 12.81 $\mu$m has been removed as well. The vertical lines and PAH comparison spectrum are as described in Figure 17.

at 11.3, 12.0, and 12.7 $\mu$m and a blue shoulder, and Class D2 has features at ∼11.4, ∼12.4, and 13.2 $\mu$m. In Figure 20, the spectrum of J004441 appears to be a blend of the D1 and D2 profiles.

In the D2 profile, the 12.4 $\mu$m feature cannot be the $H_2$ 0–0 S(2) transition at 12.28 $\mu$m because it is too broad, and no $H_2$ lines could explain the 13.2 $\mu$m feature. In most of these spectra, the 11.3 $\mu$m solo mode appears to be slightly shifted ∼0.1 $\mu$m to the red, which might be expected from Class C PAH features typically seen in environments cooler than those responsible for more normal PAH emission. Shifts of ∼0.4 $\mu$m at 12.0 $\mu$m and ∼0.5 $\mu$m at 12.7 $\mu$m are a bit harder to explain. While it is possible that the 12.4 and 13.2 $\mu$m components could be related to the duo and trio modes in some kind of modified PAH molecule, it seems equally reasonable that they could arise from some other unidentified bond in a hydrocarbon-related material.

The classifications applied by Matsuura et al. (2014) differ somewhat from ours. At 11–14 $\mu$m, they describe Class A and B profiles together as Class $\alpha$. Their Class $\beta$ is a mixture of Class A, B, and D1. They describe our Class D2 as Class $\gamma$, and our big-11 feature as Class $\delta$. Our classifications and theirs map together reasonably well, but there are exceptions. Most notably, IRAS 05063 is D1 in our scheme but Class $\delta$ in theirs. At 6–9 $\mu$m, our classifications generally agree. One exception is IRAS F05192, which we place in Class D and they place in Class B.

### 3.5. *Spectra with the 21 $\mu$m and related features*

Galactic sources with a 21 $\mu$m feature in their spectra typically show associated features at ∼8, 11, 16, and 26–30 $\mu$m, but not all features appear in all spectra (Kraemer et al. 2002). Even the 21 $\mu$m feature could be absent, because the classification is based on the total spectrum, not just the presence of one feature. The Magellanic sample behave similarly (see Figure 7). The features do not appear in unison, and they can shift noticeably in wavelength from source to source, as Figure 21 shows.

We find the central wavelength of the 21 $\mu$m feature, based on all of the identified 21 $\mu$m sources in our sample, to be 20.47 ± 0.10 $\mu$m. The standard deviation is surprisingly small given the variation in width of the feature. Our analysis confirms the presence of the 21 $\mu$m feature in all 11 spectra in this group, after their initial assignment based on visual inspection. Volk et al. (2011) described the 21 $\mu$m features as very weak in the spectra of IRAS 06111 and IRAS 05360 and as weak in the spectra of J010546 and NGC 1978 WBT 2665. These are the detections with the lowest SNRs, but they still appear to be solid detections, and the features are visible in Figure 21. The SNR gained from optimal extraction has helped here.

Our spectra show an association of 21 $\mu$m spectra with

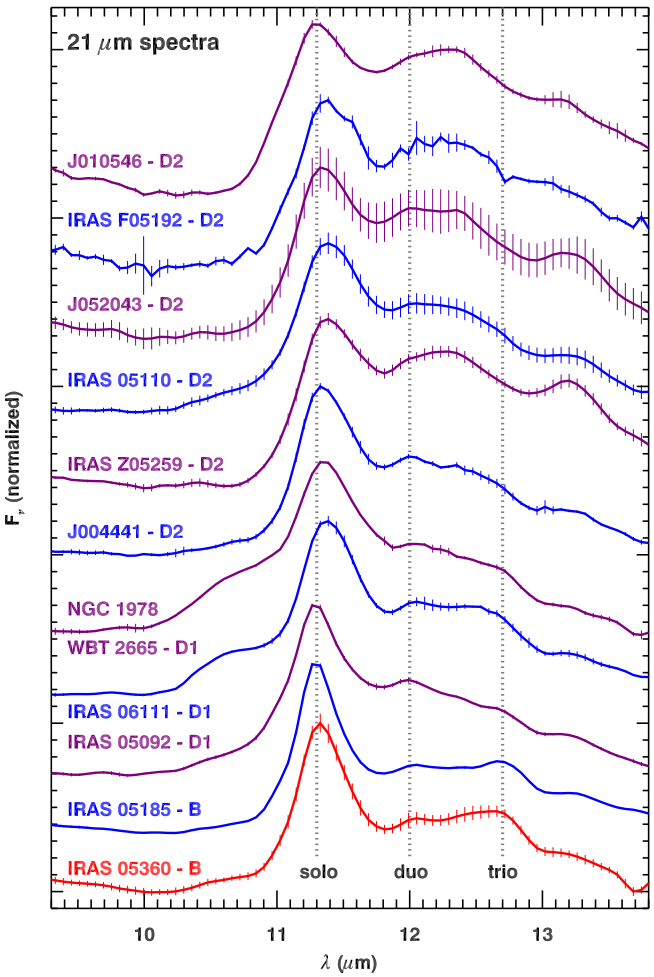


FIG. 20.— The 11–14 $\mu$m region of the spectra with 21 $\mu$m and related emission features. The vertical dotted lines are as defined in Figure 17. The spectrum of IRAS 05360 is plotted in red because it has served as the prototypical PAH spectrum in several other figures.

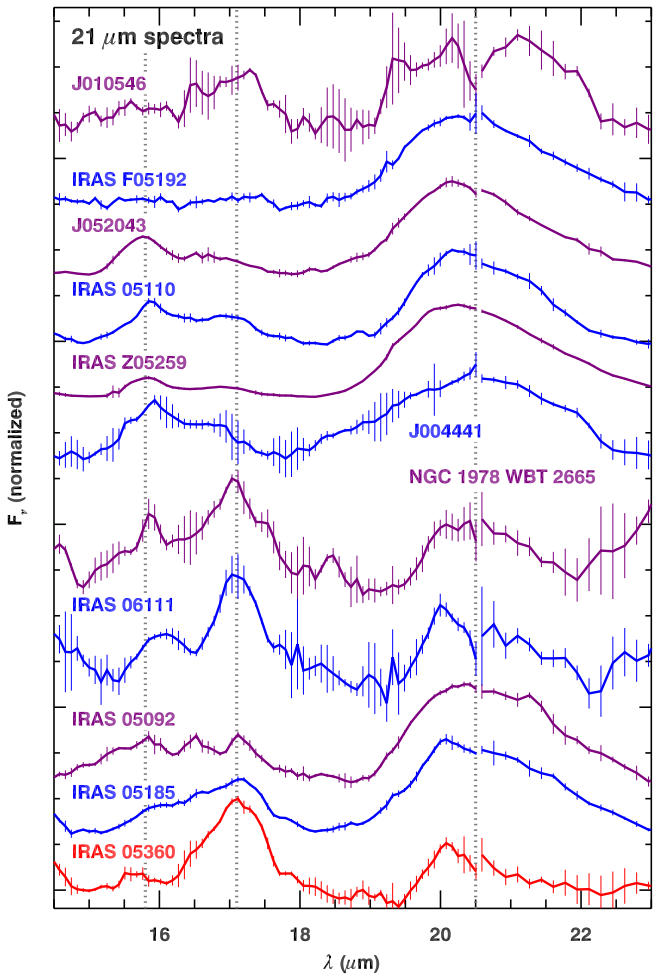


FIG. 21.— The 15–23 $\mu$m region of the spectra with 21 $\mu$m features. The spectra show three features, centered roughly at 15.8, 17.1, and 20.5 $\mu$m (the wavelengths of the dotted vertical lines). While the spectra show a 21 $\mu$m feature, the variation in the relative strengths and positions is substantial. The spectrum of IRAS 05360 is plotted in red because it has served as the prototype for Class B PAHs in several other figures.

aliphatics and a further association with unusual spectral structure in the 6–9 and 11–14 $\mu$m regions. The aliphatic feature at 6.90 appears in all 11 spectra, and most show Class D1 or D2 emission at 11–14 $\mu$m. Table 3 reveals more trends. All of the spectra with Class D2 profiles at 11–14 $\mu$m have Class D profiles at 6–9 $\mu$m, and two of the three Class D1 spectra are Class D at 6–9 $\mu$m. Aliphatics and the Class D profiles, especially D2, are linked.

### 3.5.1. *The 16 $\mu$m emission complex*

The central wavelength of the 16 $\mu$m complex is 16.51 $\pm$ 0.39 $\mu$m. The larger spread in the apparent position of this feature results from its more complex structure. In most of the spectra, it separates into two components, centered at $\sim$15.8 and 17.1 $\mu$m, although both the position and width of the component near 15.8 $\mu$m can shift considerably, as Figure 21 shows.

The position of the feature, 15.8 $\mu$m, matches the C–H bending mode adjacent to a triple, or alkyne, C$\equiv$C bond. Figure 22 illustrates the laboratory spectra of several alkynes, all of which show a feature near 15.8 $\mu$m, using data from the NIST Chemistry WebBook[17]. Table 4 gives the chemical formulae for the molecules considered. Propyne, which can be considered the prototype, shows a broad feature, due to the interactions of the C–H bending mode with numerous modes in the adjacent methyl

TABLE 4
ALKYNES

| Molecule | Formula |
|---|---|
| propyne | CH$\equiv$C—CH$_3$ |
| 1-butyne | CH$\equiv$C—CH$_2$—CH$_3$ |
| 1-pentyne | CH$\equiv$C—CH$_2$—CH$_2$—CH$_3$ |
| 1-hexyne | CH$\equiv$C—CH$_2$—CH$_2$—CH$_2$—CH$_3$ |
| 1-heptyne | CH$\equiv$C—CH$_2$—CH$_2$—CH$_2$—CH$_2$—CH$_3$ |
| 1-octyne | CH$\equiv$C—CH$_2$—CH$_2$—CH$_2$—CH$_2$—CH$_2$—CH$_3$ |
| 1,5-hexadiyne | CH$\equiv$C—CH$_2$—CH$_2$–C$\equiv$CH |
| 1,6-heptadiyne | CH$\equiv$C—CH$_2$—CH$_2$—CH$_2$–C$\equiv$CH |
| 1,7-octadiyne | CH$\equiv$C—CH$_2$—CH$_2$—CH$_2$—CH$_2$–C$\equiv$CH |
| 2,4-hexadiyne | CH$_3$—C$\equiv$C—C$\equiv$C—CH$_3$ |

[17] The National Institute of Standards and Technology maintains the WebBook at http://webbook.nist.gov/chemistry.

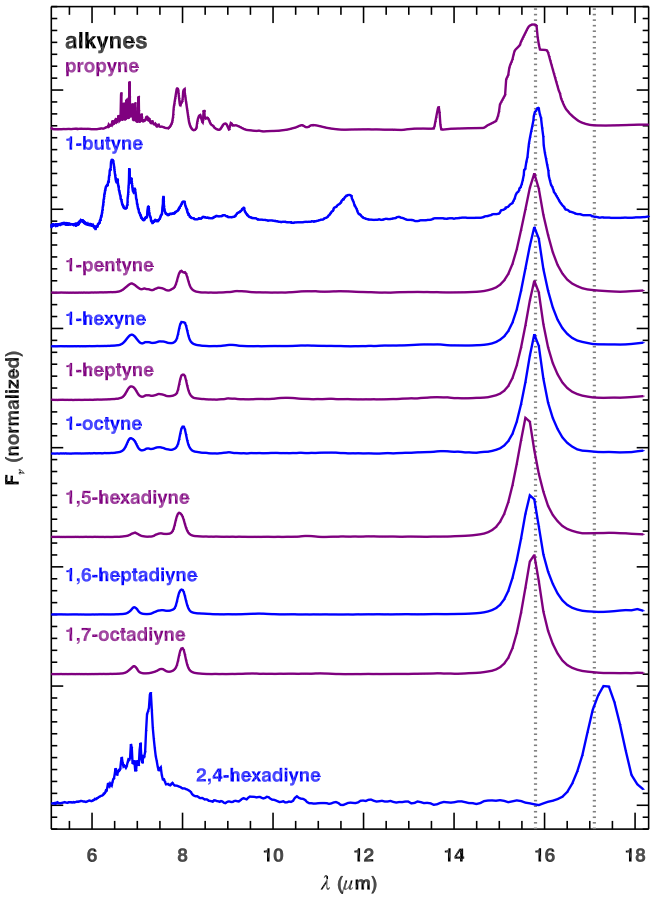


FIG. 22.— Infrared laboratory spectra of several alkyne chains. All except the last molecule have an emission feature at or near 15.8 $\mu$m; the bottom alkyne shows a feature shifted to the vicinity of the 17.1 $\mu$m feature. The data are from NIST Chemistry WebBook, and Table 4 gives the chemical formula for each molecule.

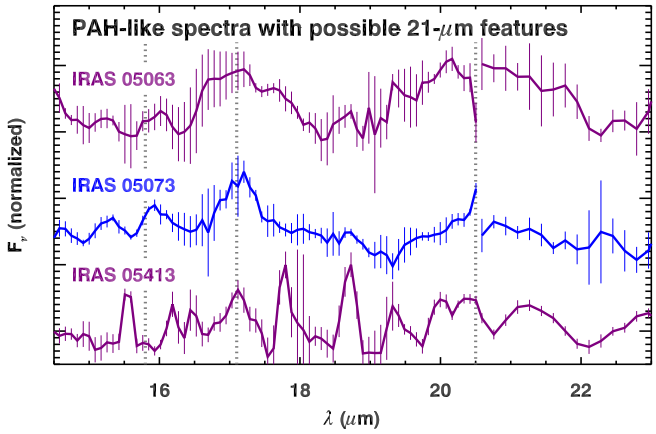


FIG. 23.— The 15–23 $\mu$m spectral region of the three candidate 21 $\mu$m sources among the PAH-like spectra. The vertical dotted lines are as defined in Figure 21.

($CH_3$) group. Malek et al. (2012) detected propyne in absorption in the spectrum of SMP LMC 011. In longer aliphatic molecules, the intervening methylene ($CH_2$) insulates the modes on one side of the molecule from the other, and the resulting feature at 15.8 $\mu$m is narrower. In molecules with a triple bond at both ends, the C–H mode is shifted to higher energies, and again, with more intervening methylene groups, this effect grows smaller.

If a long alkyne chain were attached to a larger molecule, such as a PAH, the intervening methylene groups should insulate the terminal C–H bending mode, much as it does in the longer aliphatic molecules shown in Figure 22. Given other evidence for aliphatics in the spectra of 21 $\mu$m sources (Figures 15 and 16), it is reasonable to expect that some of the aliphatic chains might be terminated by alkyne bonds. Their presence may be enhanced by photo-processing as the hot stellar core grows more exposed. Unfortunately, we are not aware of any laboratory spectra of such molecules to test this hypothesis. Different combinations of PAH, alkyne sidegroups, and alkyne chains might be able to reproduce the variation in the shapes of the observed 15.8 $\mu$m features.

The other component of the 16 $\mu$m feature is centered at ~17.1 $\mu$m. Where it is strong, this component is clearly distinct from the 17.4 $\mu$m features associated with either PAHs or fullerenes. Its carrier may be related to the alkyne chains which produce the 15.8 $\mu$m feature. If the alkyne bond is shifted one notch away from the end of the chain, the terminal carbon becomes part of a methyl group, and the energies of the C–H bending modes shift to longer wavelengths. In 2,4-hexadiyne, the shift is close to the right amount to account for the 17.1 $\mu$m feature. Unfortunately, the NIST Chemistry WebBook does not contain spectral data for longer analogues, and the laboratory spectra for related molecules with a methyl group at just one end (2-butyne, 2-pentyne, etc.), show little or no spectral structure at 15–18 $\mu$m. We conclude that the carrier of the 17.1 $\mu$m feature is not yet confirmed, but it is likely to be related to the alkyne chains responsible for the 15.8 $\mu$m feature.

The combined strength of the two components of the 16 $\mu$m complex does not exceed 5.6% of the total emission from the various features associated with the 21 $\mu$m feature. In most casess it is $\lesssim$2%. The laboratory spectra in Figure 22 also show structure at 6–9 $\mu$m, but that structure would be difficult to detect, given its relative strength to the already weak 15.8 and 17.1 $\mu$m features.

### 3.5.2. *Additional 21 $\mu$m candidates*

The 6–9 $\mu$m spectra of the PAH-like sources (Figure 15) reveal two more Class D profiles, for IRAS 05063 and IRAS 05073. Both also show strong aliphatics. A third spectrum, IRAS 05413, is much noisier but consistent with these two. All three spectra are included in the analysis in Appendix 1.3 and are plotted in Figure 23.

Only IRAS 05063 has a reasonable detection at 21 $\mu$m, with a SNR of 7.5. Because the extraction algorithm used for these features shifts the wavelengths to match minima in the spectra, it will actually fit to the noise, so the extracted SNR should be taken as an upper limit. The central wavelength of the extracted feature is within 1 $\sigma$ of the mean for this feature, which adds some confidence. Furthermore, the 17.1 $\mu$m feature looks reasonable and is extracted with a SNR of 5, so this spectrum remains a viable candidate as a 21 $\mu$m source. Volk et al. (2011) describe its 21 $\mu$m feature as "vW" (very weak). While we conclude that this source is a 21 $\mu$m candidate, we cannot confirm it as a definite 21 $\mu$m source.

IRAS 05073 does not have a measurable 21 $\mu$m feature, and Volk et al. (2011) describe it possibly very weak

TABLE 5
MEAN WAVELENGTHS AND MgS TEMPERATURES FOR THE 26–30 $\mu$m FEATURE

| Group | Number | Out of | $\lambda_C$ ($\mu$m) | $T_{MgS}$ (K) |
|---|---|---|---|---|
| Fullerene | 4 | 5 | 29.88 ± 0.38 | 250 |
| Mixed | 6 | 7 | 30.34 ± 0.59 | 220 |
| Big 11 | 5 | 10 | 30.65 ± 0.57 | 200 |
| Combined | 15 | 22 | 30.32 ± 0.59 | 220 |
| | | | | |
| PAH-like | 6 | 6 | 28.62 ± 1.49 | 360 |
| 21 $\mu$m (B) | 2 | 2 | 28.73 ± 0.21 | 350 |
| 21 $\mu$m (D2) | 6 | 6 | 28.52 ± 0.30 | 370 |
| 21 $\mu$m (D1) | 3 | 3 | 28.26 ± 0.31 | 400 |
| Red | 2 | 5 | 27.92 ± 0.57 | 450 |
| Combined | 18 | 21 | 28.47 ± 0.86 | 380 |

(which they described as "vW?"). The structure in its spectrum at 15.8 and 17.1 $\mu$m suggests that it should also be considered as a candidate.

While our analysis extracted a 21 $\mu$m feature for IRAS 05413, it is only at 3 $\sigma$, and the central wavelength is about 3 $\sigma$ from the mean. This source is the least likely of the three to be a 21 $\mu$m source.

### 3.6. *The 26–30 $\mu$m feature*

Table 5 presents the mean wavelengths of the 26–30 $\mu$m feature in the different spectral groups, based on the analysis in Appendix 1.3. The data show a shift in the position of the 26–30 $\mu$m feature, which is apparent even in Figure 2. The central wavelength moves from the red to the blue in the sequence Big-11, Mixed, Fullerene, PAH-like, 21 $\mu$m, and Red. A gap of over 1 $\mu$m separates the Fullerene and PAH-like groups, suggesting that we really have two larger groups.

Volk et al. (2002) reported that in the *ISO*/SWS spectra of several Galactic 21 $\mu$m sources, the 26–30 $\mu$m feature appeared to consist of two components, with a narrower component centered at ∼26 $\mu$m and a broader component centered at ∼33 $\mu$m. These two components would explain a notch apparent in the feature at ∼27 $\mu$m, but that structure is more likely to be an artifact in the spectra due to a light-leak at the long-wavelength end of Band 3D (27.3 $\mu$m) and the poor quality of Band 3E (27.3–27.7 $\mu$m) (Sloan et al. 2003). In our Magellanic sample, the 26–30 $\mu$m feature appears to shift smoothly from one spectrum to the next. None of the individual spectra show evidence for two separate components to the feature. The difference between the Magellanic and Galactic samples is more likely due to the differences in the spectrometers and not differences in the dust chemistry.

Forrest et al. (1981) discovered the 26–30 $\mu$m feature in spectra from evolved carbon-rich objects, and Goebel & Moseley (1985) proposed MgS dust as the carrier. One of the major objections to MgS as the carrier of the 26–30 $\mu$m feature has been the abundance problem created by the strength of the feature. It can account for up to about a third of the total luminosity of some sources, which would require more sulfur than is available from the central star (Zhang et al. 2009b). If only the outer layers of the grains were MgS, then this would solve the problem. Observational evidence from spectral studies of Magellanic carbon stars supports this scenario. As the dust shells around the stars grow increasingly red,

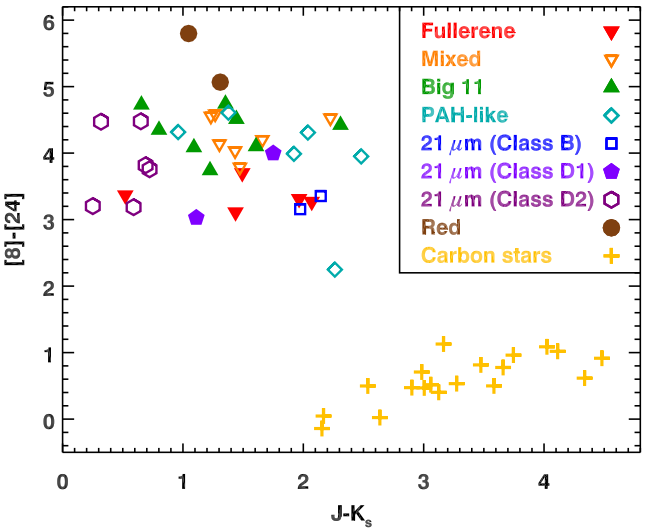


FIG. 24.— A color-color plot showing the locations of the spectral groups defined in this paper. The 21 $\mu$m sources are distinguished by the nature of the PAH emission in their spectra at 6–9 and 11–14 $\mu$m. The comparison sample of carbon stars are the SMC sample originally considered by Sloan et al. (2006). The PAH-like source closest to the carbon stars is IRAS 00350.

the MgS feature strength climbs just as the SiC strength drops (e.g. Sloan et al. 2006; Zijlstra et al. 2006). This behavior is consistent with the coating of dust grains with MgS as they move away from the central star and cool (Lagadec et al. 2007; Leisenring et al. 2008).

Models of condensation of MgS in carbon-rich outflows support this scenario, and the optical properties of MgS-coated grains reproduce the observed feature (Zhukovska & Gail 2008). A more recent study of the optical properties of MgS-coated grains reveals that coatings thin enough to stay within the abundance limits can produce the observed feature (Lombaert et al. 2012).

Assuming that MgS is the carrier of the 26–30 $\mu$m feature, we estimate the dust temperature from its position, following Hony et al. (2002). They could fit the central wavelength by varying either the grain shape distribution (with spherical grains producing the bluest features) or the grain temperature. If the latter is the cause of the shift, then their power law can be used: $T_{MgS} = 5.1 \times 10^{14} \lambda_C^{-8.34}$.

Table 5 includes a column giving the MgS dust temperatures using the above equation. The first three groups have MgS dust temperatures of ∼200–250 K, vs. the remaining groups, at ∼350–450 K. Thus, if MgS produces the 26–30 $\mu$m feature, then a shift in dust temperature can explain the observed shift in the position of the feature among the spectral groups we have defined, with the Big-11 spectra having the coolest MgS dust and the 21 $\mu$m sources having the warmest.

## 4. SUPPORTING PHOTOMETRY AND SPECTROSCOPY

### 4.1. *Infrared colors*

For the sources in the sample, we have collected photometry from several infrared and optical catalogs. Appendix 2 explains how we compiled the photometry and presents the results for each source in the sample. In this section we draw from those data to better under-

TABLE 6
INFRARED COLORS

| Group | $< J - K_s >$ | $< K_s - [3.6] >$ | <[3.6]−[4.5]> | <[4.5]−[5.8]> | <[8]−[24]> |
|---|---|---|---|---|---|
| Fullerene | 1.50 ± 0.61 | 1.60 ± 0.09 | 0.88 ± 0.09 | 2.40 ± 0.08 | 3.35 ± 0.22 |
| Mixed | 1.51 ± 0.35 | 1.64 ± 0.27 | 0.97 ± 0.23 | 2.89 ± 0.30 | 4.26 ± 0.30 |
| Big 11 | 1.26 ± 0.51 | 2.05 ± 0.53 | 1.11 ± 0.16 | 3.28 ± 0.52 | 4.33 ± 0.34 |
| PAH-like | 1.84 ± 0.57 | 1.81 ± 0.31 | 0.93 ± 0.19 | 2.95 ± 0.94 | 3.90 ± 0.85 |
| 21 $\mu$m (Class B) | 2.06 ± 0.12 | 2.86 ± 0.42 | 0.90 ± 0.30 | 4.05 ± 0.37 | 3.26 ± 0.14 |
| 21 $\mu$m (Class D1) | 1.43 ± 0.55 | 1.65 ± 0.63 | 0.92 ± 0.37 | 4.10 ± 0.27 | 3.51 ± 0.69 |
| 21 $\mu$m (Class D2) | 0.54 ± 0.20 | 0.61 ± 0.36 | 0.51 ± 0.45 | 4.11 ± 0.56 | 3.82 ± 0.57 |
| Red | 1.16 ± 0.14 | 1.89 ± 1.28 | 1.49 ± 0.41 | 4.16 ± 1.10 | 5.63 ± 0.50 |

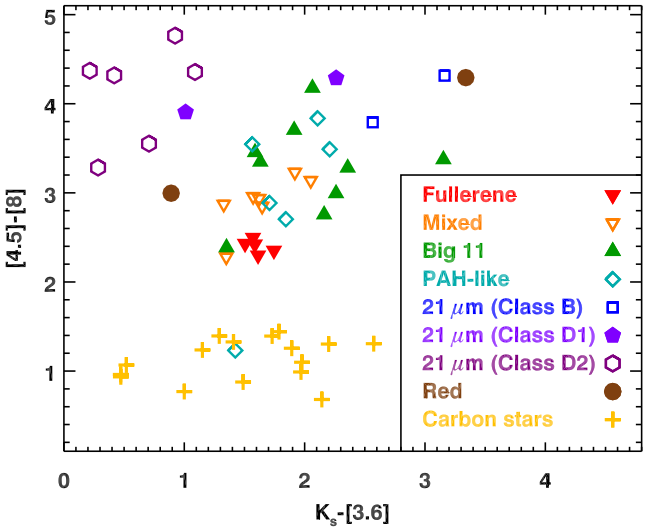


FIG. 25.— A color-color plot with alternative axes showing the locations of the spectral groups defined in this paper. The comparison sample is the same as in Fig. 24. The location of the Fullerene spectra are more tightly constrained in this plot. IRAS 00350 is the PAH-like source amongst the carbon stars, and NGC 1978 WBT 2665 is the Class D1 21 $\mu$m source near to the D2 sources.

stand the photometric properties of the spectral groups we have defined.

Figures 24 and 25 show how the spectral groups are distributed in infrared color-color space. We have included a control sample of carbon stars defined by Sloan et al. (2006), but with updated photometry and applying the techniques described in Appendix 2. The carbon stars trace a well-defined sequence from the bottom center of the diagram up and to the right. The carbon-rich post-AGB objects occupy a different part of the diagram, with blue near-IR colors, because the central star is partially revealed, and red mid-IR colors, because the dust is moving away from the central star and cooling. Table 6 gives mean colors for the spectral groups.

The Fullerene sources have bluer [8]−[24] colors than the Big-11 and Mixed groups. Figure 25 reveals that the colors of the Fullerene sources are tightly constrained in both $K - [3.6]$ and [4.5]−[8].

The 21 $\mu$m sources with Class D2 PAH spectra stand out from the other 21 $\mu$m sources at shorter wavelengths, showing bluer colors in both $J - K_s$ and $K_s - [3.6]$. The 21 $\mu$m sources with Class D1 PAH spectra are bluer than the Class B spectra in both of these colors, but only two spectra plotted in each figure is not enough to draw conclusions.

TABLE 7
TEMPERATURES IN PNE

| Group | Num. | Electron T (K) | Effective T (K) |
|---|---|---|---|
| Fullerene | 4 | 12,430 ± 590 | 34,900 ± 5,100 |
| Mixed | 7 | 11,630 ± 1,340 | 31,300 ± 2,000 |
| Big 11 | 4 | 12,580 ± 730 | 42,800 ± 23,400 |
| control PNe—C-rich | 17 | 13,600 ± 1,330 | 64,300 ± 26,100 |
| control PNe—featureless | 21 | 14,280 ± 2,260 | 65,500 ± 43,400 |

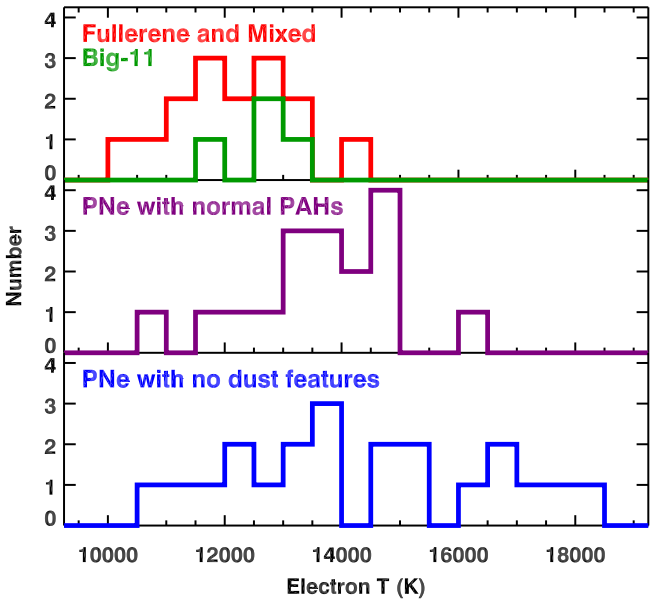


FIG. 26.— The distribution of electron temperatures within the sources in our sample classified as Fullerene, Mixed, or Big 11 (top panel), compared to the control samples of dusty carbon-rich and featureless PNe. The three groups plotted in the top panel have similar distributions, and these differ from both of the control samples.

### 4.2. *Temperatures*

The central stars of PNe exhibiting fullerene features generally appear to be cooler than in more typical PNe (e.g. García-Hernández et al. 2012; Otsuka et al. 2013). To investigate the temperatures of the systems in our sample, we have examined the electron temperature of the gas, the effective temperature of the central star, and the optical colors of the nebulae. Our control sample is based on the PNe observed by the IRS and examined by Stanghellini et al. (2007) and Bernard-Salas et al. (2009). We include the spectra not observed by us and classified by them either as carbon-rich, based on the presence of

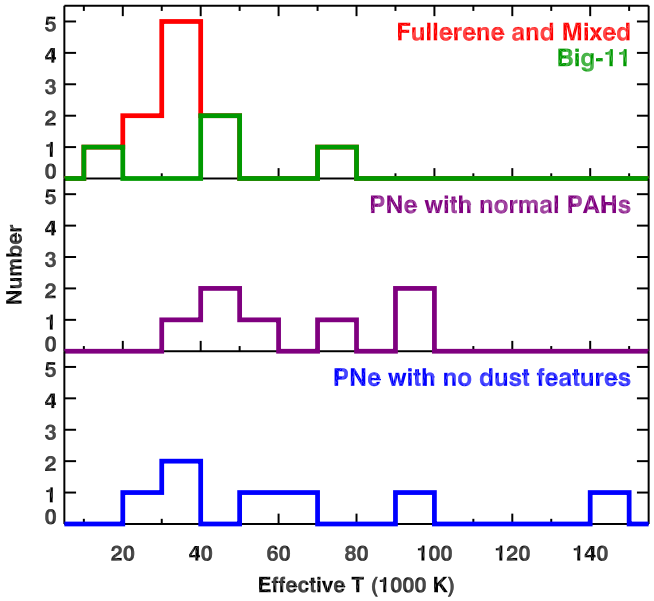


FIG. 27.— The distribution of the effective temperatures of the central stars of the PNe in our sample (top panel), compared to the control samples of PNe (bottom two panel).

normal PAH emission in their spectra (Class A or B), or featureless, based on the absence of any solid-state features.

Leisy & Dennefeld (2006) measured the electron temperature in a large sample of Magellanic PNe, using the [O III] and [N II] lines. Where these produce different temperatures, we took an average. Table 7 presents the means for the Fullerene, Mixed and Big-11 groups, along with control samples. The uncertainties are the standard deviations of the samples. Figure 26 compares the temperature distribution of these groups with the two PNe control samples. The Fullerene, Mixed, and Big-11 groups are indistinguishable. The ionized gas in the PNe producing fullerene, mixed, or big-11 features tends to be cooler than the gas in PNe associated with typical PAH emission. The ionized gas in featureless PNe spans a range of temperatures covering the PNe in our sample and PNe with normal PAHs and continuing to significantly higher temperatures.

Several observers have estimated the effective temperature of the central stars in Magellanic PNe. We rely on the studies of the LMC and SMC by Villaver et al. (2003, 2004). They based their estimates on He II lines and H$\beta$, which often lead to different results. For comparative purposes, we will concentrate on the estimates from H$\beta$ because they cover more of our sample. We have supplemented these temperatures with measurements of SMP LMC 002 and 085 by Dopita et al. (1994) and Herald & Bianchi (2004) and a rough estimate of the effective temperature of IRAS 05588 by Volk et al. (2011).

The mean effective temperatures for the different groups appear in Table 7. As with the electron temperatures, the Fullerene and Mixed groups have overlapping distributions. The Big-11 sources show a wider spread, with three sources shifting to higher temperatures. The exception is IRAS 05588, which has $T_{eff} \approx 14{,}000$ K and is better classified as a proto-PN (Volk et al. 2011). Its presence in the Big-11 group is due primarily to a strong

TABLE 8
OPTICAL COLORS

| Group | $< U-B >$ | $< B-V >$ | $< V-I >$ |
|---|---|---|---|
| Fullerene | $-1.07 \pm 0.18$ | $0.23 \pm 0.33$ | $-0.32 \pm 0.49$ |
| Mixed | $-0.58 \pm 0.32$ | $0.99 \pm 0.22$ | $-1.04 \pm 0.48$ |
| Big 11 | $-0.34 \pm 0.45$ | $1.15 \pm 0.68$ | $-0.46 \pm 0.89$ |
| PAH-like | $0.03 \pm 1.04$ | $0.90 \pm 0.55$ | $0.20 \pm 1.36$ |
| 21 $\mu$m | $1.08 \pm 0.85$ | $1.29 \pm 0.50$ | $1.29 \pm 0.73$ |
| Red | $-0.49 \pm$ ··· | $0.63 \pm$ ··· | $-0.94 \pm$ ··· |

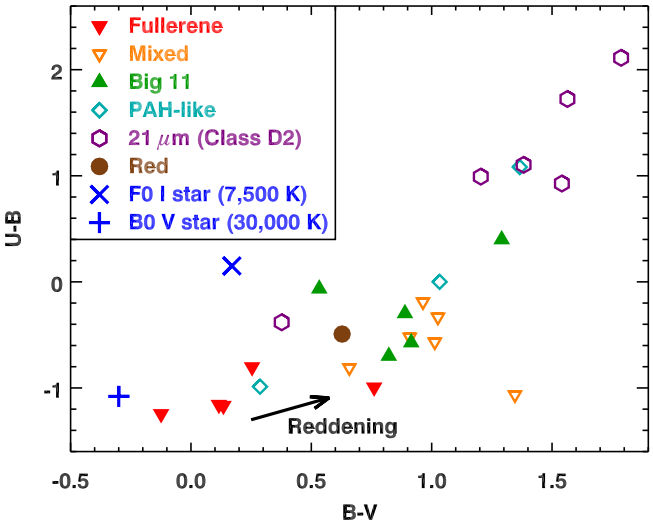


FIG. 28.— An optical color-color plot of the carbon-rich post-AGB sample, showing that the colors are consistent with dust extinction. The positions of an F0 supergiant and a main sequence B0 star ($T_{eff}$ = 30,000 K and 7,500 K, respectively) are marked with blue crosses (Cox 2000). The reddening vector depicts one magnitude of extinction as determined by Rieke & Lebofsky (1985). The two non-fullerene sources with $B-V < 0.5$ are IRAS 05127 (PAH-like) and J010546 (21 $\mu$m/D2).

18 $\mu$m feature (Section 3.3.4), but its spectrum has the strongest PAH-like contribution at 11 $\mu$m in the group, suggesting that it may differ from the rest. Excluding it raises $< T_{eff} >$ for the three remaining Big-11 sources to 52,400 ± 16,500 K, clearly hotter than the Fullerene and Mixed groups.

Figure 27 illustrates the differences between the effective temperatures of the PNe in our sample and the control samples. The results are similar to those for the electron temperatures, although the number of control sources for which we have effective temperatures is smaller. The dusty PNe from the control group, which only show PAH emission and no other dust, tend to have hotter central sources than the PNe in our sample, while the dust-free PNe show a wide range of temperatures.

The temperature analysis confirms previous conclusions about the fullerene sources. Fullerenes appear in a subset of PNe with lower electron temperatures and cooler central stars than the general population of PNe.

### 4.3. *Optical colors*

An examination of optical colors reveals clear differences among the spectroscopic groups in our sample. Figure 28 plots $U-B$ versus $B-V$. The Fullerene sources occupy the blue end of the diagram, while the 21 $\mu$m sources for which we have optical colors occupy the red

end. The Mixed, Big-11, and PAH-like spectra are between the two extremes. Many sources are missing from this diagram because they are too embedded for optical photometry at the distances involved. Generally, sources with $J - K \gtrsim 1$, are absent, which explains why for the 21 $\mu$m sources, only those associated with Class D2 PAH emission appear. The Fullerene and Mixed sources are an exception. Despite their red $J - K$ colors, they are surprisingly blue in the optical.

Figure 28 also shows the nominal positions of an F0 supergiant, which is analogous to the central star in a post-AGB object with 21 $\mu$m emission, a 30,000 K star to approximate the central star in PNe with fullerene emission (Cox 2000), and a vector depicting one magnitude of interstellar extinction (Rieke & Lebofsky 1985). While the extinction from carbon-rich circumstellar dust will be different in detail from typical interstellar extinction, the reddening arrow still gives a reasonable impression. The optical colors in our sample are consistent with extinction by circumstellar dust.

The blue colors of the Fullerene sources indicate that we have a clear line of sight to the central star in these systems, or if not that, that we at least can see a region scattering direct radiation from the central star. Polarimetry would settle that question, but in the meantime it is fair to say that the optical colors of the Fullerene sources are consistent with a reasonably clear line of sight to a radiation source of ∼30,000 K at their center. The colors of the Mixed and Big-11 sources indicate more dust extinction. In the other groups, the line of sight to the central region is more obscured.

Table 8 presents mean optical colors for the spectral groups in our sample and provides some quantitative support for Figure 28. The $V - I$ colors tell a different story. Once we move to wavelengths longer than $V$, the Fullerene sources cease to be the bluest. The near- and mid-IR colors plotted in Figures 24 and 25 show that the Fullerene sources do have significant amounts of circumstellar dust; it is just not distributed in the line of sight to the central star.

### 4.4. *Spectral energy distributions*

Figure 29 plots the mean SED for each spectral group, separating the 21 $\mu$m sources by the class of PAH emission. We have not included the Red group because of the disparate nature of its members. For each remaining group or subgroup, the spectra and photometric data were normalized at 3.6 $\mu$m and averaged.

The Fullerene spectra diverge from the other groups at the shortest wavelengths, showing bluer SEDs. This behavior is more obvious in Figure 28.

Within the 21 $\mu$m group, the Class D2 sources differ from the others, showing a secondary maximum peaking at $J$ while the rest drop monotonically from [4.5] to $V$ and $U$, due to extinction from dust. The dust around the Class D2 sources is optically thin enough to reveal a secondary peak at $J$, corresponding to a blackbody temperature of ∼4000 K. If the peak were due to hot amorphous carbon dust, its temperature would be ∼2500 K, well above its condensation temperature. The inflection at ∼2 $\mu$m in the Class D1 SED may be of the same nature.

A better explanation of the differences between the D2 sources and the other 21 $\mu$m sources comes from the models of their SEDs by Volk et al. (2011). The optical depth that they fitted at 0.55 $\mu$m ranged from 1.1 to 5.6 for the six Class D2 sources, with a mean of 2.5 ± 1.9. For the five other 21 $\mu$m sources, the minimum optical depth was 9.4, and the mean was 18.8 ± 8.3, with no obvious distinction between the Class D2 and Class B sources. The distribution of temperatures of the central stars showed no difference between the different subgroups of 21 $\mu$m sources. The mean temperature was 7,400 ± 2,000 K, quite cool compared to the central temperatures of the Fullerene and related groups.

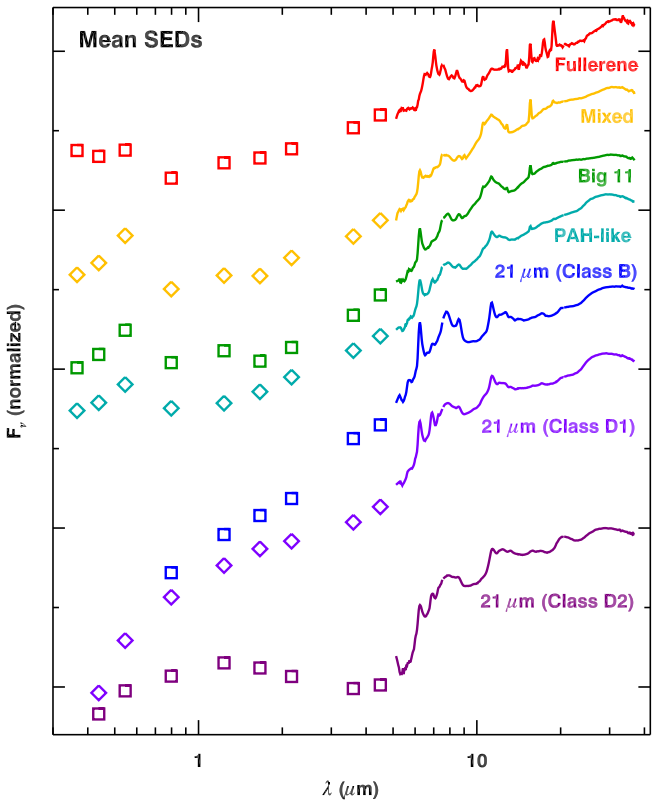


FIG. 29.— Mean SEDs for each spectral group.

TABLE 9
ABSOLUTE BOLOMETRIC MAGNITUDES

| Group | Num. | $< M_{\rm bol} >$ | Notes |
|---|---|---|---|
| Fullerene | 5 | $-4.34 \pm 0.52$ | |
| Mixed | 7 | $-4.30 \pm 0.37$ | |
| Big 11 | 9 | $-4.36 \pm 0.86$ | |
| PAH-like | 6 | $-4.70 \pm 0.16$ | excluding IRAS 00350 |
| 21 $\mu$m (Class D2) | 6 | $-4.55 \pm 0.25$ | |
| 21 $\mu$m (Class D1) | 3 | $-4.90 \pm 0.20$ | |
| 21 $\mu$m (Class B) | 2 | $-5.12 \pm 0.07$ | |

### 4.5. *Bolometric magnitudes*

Table 8 also includes absolute bolometric magnitudes for the sample, which are estimated as described in Appendix 2. All of the sources have bolometric magnitudes between −3.3 (SMP SMC 099) and −5.8 (SMP SMC 011), with the exception of IRAS 00350, which has $M_{\rm bol}$ = −7.1, right at the AGB limit. Table 9 gives the mean bolometric magnitude for each spectral group (excluding IRAS 00350). The overlap betwen the Fullerene, Mixed,

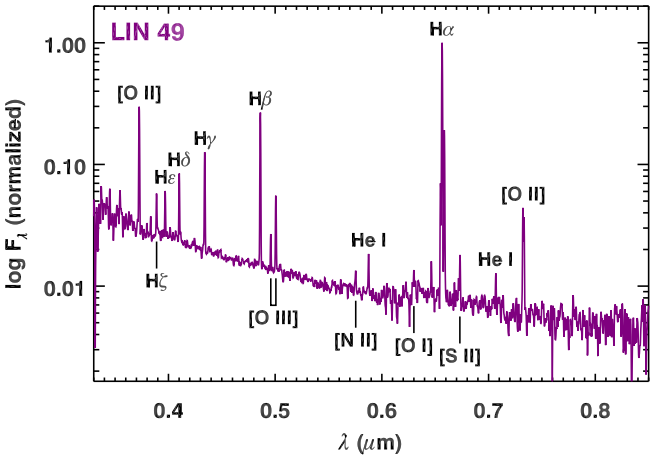


FIG. 30.— An optical spectrum of LIN 49, showing the Balmer series of hydrogen recombination lines, He I emission lines, and forbidden lines from [O II], [O III], [N II], and [S II].

and Big-11 groups is complete, suggesting a common origin, although the scatter in the Big-11 sources is substantial. The PAH-like and 21 $\mu$m groups are brighter, and there is enough separation between the 21 $\mu$m subgroups to suggest that the Class D2 spectra come from a fainter population.

### 4.6. *Optical spectroscopy*

Figure 30 shows the optical spectrum for LIN 49, taken with the Double-Beam Spectrograph on the 2.3 m telescope at Siding Springs Observatory on 2008 December 17. The spectrum shows the Balmer series of hydrogen recombination lines and forbidden lines from [O II] at 3727 and 7323 Å and [O III] at 4958 and 5007 Å. Weaker lines are also apparent from He I at 5876 and 7065 Å, [N II] at 5755 Å, and [S II] at 6731 Å. These relatively low-excitation lines indicate that LIN 49 is a relatively cool PN, much like the other fullerene sources.

### 4.7. *Optical variability*

In the final stages of their evolution on the AGB, stars are associated with strong pulsational variability as they eject their envelopes and evolve into white dwarfs. One might expect some variability in the embedded post-AGB sources in our sample, where the central star still has a significant envelope and is relatively cool.

A search for sources in our sample in the OGLE-III survey of the Magellanic Clouds (Soszyński et al. 2009, 2011) reveals five variables. Four of the five, J004441, IRAS F05192, J052043, and IRAS Z05259 are 21 $\mu$m sources with Class D2 PAH emission. The first three are semi-regular variables; the last is a small-amplitude variable. The fifth variable is IRAS 00350, the exceptional source in the PAH-like group. It is classified as a small-amplitude variable.

The EROS-2 LMC survey uncovered two additional variables, both 21 $\mu$m sources, IRAS 05092, and IRAS 05413 (Spano et al. 2011). Multiple periods are given for IRAS 05092, making it a likely semi-regular. It is a 21-$\mu$m source with Class D1 PAH emission. IRAS 05413 is a PAH-like source, and its variability was not characterized.

Both the OGLE and EROS surveys include a Mira only 3.″6 away from SMP LMC 048, but this is a different source.

Surprisingly, the four 21 $\mu$m variables detected in the OGLE survey are classified as oxygen-rich, based on their Wesenheit index, which is insensitive to reddening and usually separates carbon-rich and oxygen-rich AGB stars reliably. However, optical spectroscopy of J004441 shows that it is clearly a carbon-rich object (De Smedt et al. 2012), casting some doubt on the applicability of the Wesenheit index to post-AGB objects.

The variables include three semi-regulars and one small-amplitude variable among the Class D2 sources, one semi-regular among the Class D1 sources, and two small-amplitude or uncharacterized variables among the PAH-like sources. Thus three of the six Class D2 sources are semi-regular variables, compared to one of the five other 21 $\mu$m sources. This is most likely a selection effect caused by the differences in dust extinction in the sources. In the Class D2 sources, we can see deeper into the system, making the variability easier to detect.

## 5. DISCUSSION

### 5.1. *Notes on individual sources*

Spectral classification involves placing sources which show a continuous distribution of spectral properties into discrete bins, usually with the constraint that the number of bins should be minimized. Successful classification can reveal trends in the properties of the sources not otherwise apparent, which the classification presented here has accomplished. However, a number of sources resisted our efforts to pigeon-hole them, either because they are at the boundary between two groups, or because they show unusual characteristics which do not fit the average properties of any bin.

Several of the transition sources have been pointed out above. The Mixed source SMP SMC 013 could be placed in the Fullerene group, and the Big-11 source SMP LMC 085 could belong with the Mixed sources. As noted in Section 3.5.2, the PAH-like source IRAS 05063 is almost a 21 $\mu$m source, and IRAS 05073 may be similar.

IRAS 05588 is classified in the Big-11 group despite the absence of an obvious big-11 feature because it shows the associated strong emission shoulder at $\sim$18 $\mu$m. This approach is analogous to the classification of some sources by Kraemer et al. (2002) as 21 $\mu$m sources because their spectra included the associated spectral features but not the 21 $\mu$m feature itself. However, this source is much cooler than the other three Big-11 sources. Its inclusion in any group should not take away from its unique spectrum.

The Big-11 source SMP SMC 020 has an unusual spectrum dominated by strong broad features with peaks at $\sim$11 and $\sim$19 $\mu$m. If this spectrum were redshifted silicate emission, such as has been seen in active galactic nuclei (e.g. Hao et al. 2005; Hony et al. 2011), then the 10 $\mu$m silicate feature (rest wavelength) would be more asymmetric, with a sharper rise on the blue side than the red, and the 18 $\mu$m silicate feature would have to be at 20 $\mu$m to match the shift at 10 $\mu$m. The complete lack of a shift in the [Ne III] line at 15.6 $\mu$m is the nail in the coffin for this scenario. Instead, we have a spectrum showing more clearly than any other the 18 $\mu$m shoulder associated with the big-11 feature.

SMP SMC 006 in the PAH-like group differs in some ways from the rest of the group. Its spectral structure at 11–14 $\mu$m fits the rest of the group well, but its spectrum also shows an inflection at 18 $\mu$m that could be the shoulder associated with the big-11 feature.

IRAS 00350 is another exception among the PAH-like sources. First, its spectrum shows nearly normal PAH emission in both the 6–9 and 11–14 $\mu$m ranges. Only the width of the 11.3 $\mu$m feature is consistent with Class D1 emission. Second, it is 2.4 mag brighter than the mean for the remaining PAH-like sources and 1.3 mag brighter than the next brightest source in our sample. Third, its infrared colors place it close to or in the range of colors covered by carbon stars. Whitelock et al. (1989) first suggested that IRAS 00350 may be an interacting binary, although they also noted that it could be a post-AGB object evolving to a PN. The combination of its unusual luminosity, colors, and carbon-rich nature are suggestive that it is a symbiotic carbon star (Whitelock, private communication, 2013)

Two non-Fullerene sources show unusually blue $B-V$ colors, the PAH-like source IRAS 05127 and the 21 $\mu$m source J010546. IRAS 05127 is the only Class A PAH source among the PAH-like spectra, and its blue colors in both $B-V$ and $U-B$ indicate less dust extinction to the central nebula, where the PAHs may be more processed.

J010546 has a unique spectrum which is difficult to classify, as noted by Volk et al. (2011). Its infrared spectrum shows a strong jump from 10 to 11 $\mu$m reminiscent of the larger jump in the spectrum of the T Tauri star CoKu Tau 4 (Forrest et al. 2004). The latter spectrum arises from a circumstellar disk with an inner gap. While one must be careful about invoking disk geometries, the parallels are interesting. In the optical, J010546 is bluer than the other Class D2 sources by 0.8 mag in $B-V$ and 0.6 mag in $U-B$, and such a relatively clear line of sight in a relatively red source (at longer wavelengths) is consistent with a disk or torus-like geometry.

We included SMP SMC 025 in the sample because the 11 $\mu$m feature might have been SiC, but this source is oxygen-rich. The spectrum shows emission peaks at 18–19, 23–24, 27–28, and 33 $\mu$m, and these reveal the presence of crystalline silicates. The shape of the spectrum in the 25–35 $\mu$m region is too structured to be consistent with any of the MgS features in the other spectra. Furthermore, the feature at $\sim$11 $\mu$m is bluer and broader than the big-11 features. Silicate dust would normally show a peak at 10 $\mu$m if it were amorphous, or structure throughout the 10–11 $\mu$m region if it were crystalline. While the longer-wavelength features can be ascribed to crystalline silicates with confidence, the nature of the 11 $\mu$m feature remains unclear.

### 5.2. *Coated grains and SiC*

Section 3.6 explained that grains coated with MgS would produce the observed 26-30 $\mu$m feature while staying within the abundance limits. This mechanism may also solve a similar problem with SiC as the carrier of the big-11 feature first noted by Bernard-Salas et al. (2009). Comparisons of carbon stars in the Galaxy, LMC, and SMC show that more metal-poor carbon stars have less SiC in their spectra (e.g. Sloan et al. 2012, and references therein). This relation is likely driven by the abundance of Si. How then can the big-11 features be so strong in Magellanic post-AGB objects if the strength of the SiC feature is limited by abundances on the AGB?

Grains coated with SiC would produce strong big-11 features, as observed, despite the lower amounts of available Si. This scenario is consistent with observations of how the strength of the SiC feature behaves with increasing mass-loss rate for stars of different metallicities. In the more metal-rich Galactic sample, SiC forms first, followed by a layer of amorphous carbon and finally, once the dust shell is sufficiently optically thick, MgS (see Figure 10 by Sloan et al. 2012, as an example). However in the more metal-poor Magellanic samples, the SiC strength rises more slowly as the dust shells thicken and redden, due presumably to the lower abundance of Si. Lagadec et al. (2007) and Leisenring et al. (2008) both suggested that the metal-poor case is consistent with a layer of SiC-rich material around a core of amorphous carbon.

As a star evolves off the AGB and sheds its envelope, circumstellar dust grains are exposed to an increasingly harsh radiation field. SiC has a higher condensation temperature than amorphous carbon, and increased photo-processing of the grains would preferentially remove solid carbon from the outer layers of the grains, making the grains more SiC-rich at their surface and producing stronger SiC features in the dust spectrum. The condensation sequence in the Galaxy, with SiC grains forming first and coatings of amorphous carbon second, would explain why the spectra of carbon-rich PNe in the Galaxy rarely show SiC dust features (Casassus et al. 2001). The entire mantle would have to be removed to expose the SiC core.

The origin of the 18 $\mu$m shoulder associated with the big-11 feature remains unknown. With the exception of SMP SMC 025, none of our sources show any evidence of oxygen-rich dust at any other wavelength, making it unlikely that the 18 $\mu$m shoulder could arise from silicates. In the more intense radiation fields expected in post-AGB environments, some processing of the CO gas is expected, and while silicates could conceivably form from the freed oxygen, the lack of a 10 $\mu$m silicate emission feature would be difficult to explain.

### 5.3. *The Fullerene, Mixed, and Big-11 spectra*

Compared to the general population of PNe associated with carbon-rich dust, the properties of the Fullerene, Mixed, and Big-11 groups roughly follow two progressions. First, we see a temperature progression, with the fullerenes appearing only in the vicinity of central stars with effective temperatures of $\sim$25,000–40,000 K, and the big-11 feature at temperatures up to $\sim$ 70,000 K. Second, we see an optical depth progression, with the bluest $UBV$ colors associated with the Fullerene group, which is defined to be those fullerene sources with no PAH emission in the 6–9 $\mu$m range. The Mixed spectra, which show both fullerene and PAH features, are more enshrouded than the Fullerene group, both in the optical and at longer wavelengths, like [8] $-$ [24]. However, the photometric data complicate this scenario.

The SEDs of the Mixed and Big-11 groups are quite similar and show substantial overlap in all colors considered. How can one group have fullerene emission in its spectra and not the other? Invoking a disk or torus and differences in inclination between the two groups might

help, but that is inconsistent with the similarities in the SEDs and photometric colors in the two groups. Explaining the differences between the Fullerene and Mixed groups is also a challenge. A pole-on inclination would give a direct line of sight to the central star and its immediate environment, explaining the presence of fullerene emission and the blue optical colors of the Fullerene group, but our large beam would also include the surrounding disk which presumably would show the PAH emission evident in the Mixed group.

It is also difficult to explain why the Fullerene group has such tight distributions in infrared colors, starting with $K_s - [3.6]$ and continuing to $[8] - [24]$. The Mixed group, which is also composed of fullerene sources, shows broader color distributions which overlap the Fullerene group. It is the combination of the presence of fullerenes and absence of PAHs that somehow constrains the possible shape of the SED from 2 to 24 $\mu$m.

In the sequence from Big-11 to Mixed to Fullerene, the center of the 26–30 $\mu$m feature shifts from 30.7 to 29.9 $\mu$m. If MgS is the carrier, then this shift corresponds to a rise in temperature of the MgS dust from 200 to 250 K, and its temperature traces a relatively shielded or more distant dust component. The optical colors of the Fullerene group suggest less optically thick dust, which would lead to higher MgS temperatures. The lower MgS temperatures of the Big-11 group imply more optically thick dust, but as already noted the broad-band colors of the Mixed and Big-11 groups show little difference.

Several authors have suggested that fullerenes result from the photo-processing of larger grains, either large PAHs (Berné & Tielens 2012) or grains or clusters composed of mixtures of aromatic and aliphatic hydrocarbons (García-Hernández et al. 2012; Micelotta et al. 2012; Otsuka et al. 2013). For the cooler PNe, fullerenes appear to be the final survivor of the hydrocarbon mix, but in PNe with hotter central stars, if the dust is carbon-rich, we either see PAHs or no solid-state component at all. In these harsher radiation fields, the fullerenes either cannot form as the parent hydrocarbon population is destroyed, or they cannot survive long enough to be detected.

### 5.4. *The 21 $\mu$m and PAH-like spectra*

The 21 $\mu$m and PAH-like groups are more embedded in their own dust than the Fullerene, Mixed, and Big-11 groups, and their central stars are even cooler. Together these point to an earlier evolutionary phase closer to the AGB. Their dust properties are suggestive of less processed carbonaceous material more like amorphous carbon than the classic PAHs, fullerenes, and possibly SiC-coated grains seen in more evolved sources.

Spectra with the 21 $\mu$m feature almost always show PAH or PAH-related emission features, a point first noted by Kwok et al. (1989). This association suggests that the carrier of the 21 $\mu$m feature is either a hydrocarbon itself, or closely related. Justtanont et al. (1996) raised this possibility, based on their study of Galactic 21 $\mu$m sources, and a more recent study based on IRS spectra of Galactic sources reached a similar conclusion (Cerrigone et al. 2011). Hill et al. (1998) showed that nano-diamonds could be the responsible hydrocarbon, based on fits to the shape of the emission feature.

Our spectral sample reveals that over half of the 21 $\mu$m sources are associated with the newly defined Class D2 PAH emission at 11–14 $\mu$m, and all but three show Class D PAH structure at 7–9 $\mu$m. The 6.9 $\mu$m feature from aliphatic hydrocarbons appears in all of the 21 $\mu$m spectra, in some cases quite strongly, and in over half the 21 $\mu$m spectra, the 7.3 $\mu$m aliphatic feature is visible as well.

The spectra of all of the 21 $\mu$m sources include an emission complex at 16 $\mu$m, which we have separated into components at 15.8 and 17.1 $\mu$m. The 15.8 $\mu$m feature aligns well with a C–H mode in a terminal C≡CH bond on a longer aliphatic chain, and it further strengthens the connection of the 21 $\mu$m feature to aliphatic hydrocarbons. The 17.1 $\mu$m feature may also arise from aliphatic chains with alkyne bonds, but the supporting evidence is weaker. To produce triple bonds in aliphatics chains, it is necessary to partially dehydrogenate the methyl and methylene groups at the ends and in the middle of the chains, respectively. This suggests that the aliphatic component of the hydrocarbon mix is being photo-processed.

The carrier of 21 $\mu$m feature remains unknown, but the case for a hydrocarbon-based carrier is growing, even if it still circumstantial. Some caution is advisable. Numerous candidates for the 21 $\mu$m carrier have been proposed over the years. Zhang et al. (2009a) examined several inorganic candidates and ruled out some because they produced additional spectral features which were not observed and some because they violated abundance constraints. The latter group included TiC, fullerenes with Ti atoms, $SiS_2$ and unusual forms of SiC. Given the possibility that coated grains could bypass the abundance constraints, some of these candidates may still be viable.

### 5.5. *Non-spherical geometries*

Figure 29 shows that the 21 $\mu$m sources associated with Class B or Class D1 PAHs are the most embedded sources in our sample (after the Red sources). The Class D2 sources differ, in that they have more warm dust, indicating a clearer line of sight through the circumstellar material toward the center of the nebula. This could result from either a thinner spherical shell or an inclination effect in a disk or torus-like geometry. In the latter case, the Class D2 sources are more pole-on. The other sources could be either more edge-on or less asymmetric.

Invoking a disk-like geometry might also help explain the origin of the 21 $\mu$m feature and its associated dust features. If the dust were trapped in a disk in these systems instead of simply flowing outward, then it would remain near the central sources and be subject to more intense photo-processing for a longer period. An outflow velocity of only 5 km/s corresponds to outward motion of 1 AU/yr.[18] Thus the outflow timescales are short even compared to the short evolutionary timescales from the AGB to the PN stage. Perhaps the carrier of the 21 $\mu$m feature is an unusual hydrocarbon only produced when hydrocarbons are trapped in a disk in a post-AGB system.

The 26–30 $\mu$m feature in the PAH-like and 21 $\mu$m spectra has a central wavelength between 27.9 and 28.9 $\mu$m,

[18] A 10 km/s outflow velocity is a common assumption (Groenewegen et al. 2009, e.g.); we have halved that value to be conservative.

which is shifted significantly from the position seen in the Fullerene-Big-11 family, 29.9–30.7 $\mu$m. The corresponding MgS temperatures range from 350 to 400 K. The Class D2 sources are in the middle of the range for the PAH-like and 21 $\mu$m family. If the SEDs are indicating a clearer line of sight to the center of Class D2 sources, then one would expect them to have warmer dust, and while the near-IR colors reflect that, the MgS temperatures do not.

The spectra in this sample are not always self-consistent. For most of the trends we have uncovered, there exists at least one spectrum that is an exception. The coming and going of the 6.9 $\mu$m aliphatic feature is a good example. These spectral disparities can be explained by complex geometries, either disks or tori, and possibly clumping as well. The result would be multiple regions in our single beam, each with its own physical conditions and spectral signature. If a disk or torus is viewed edge-on, then extinction will block our view of the inner disk and central star more effectively at shorter wavelengths. Conversely, if scattering gives us an indirect view of the interior, that view is better at shorter wavelengths. Follow-up polarimetric observations would test these hypotheses and clarify the geometry.

## 6. SUMMARY

We have investigated a sample of carbon-rich post-AGB objects in the Magellanic Clouds by first classifying the mid-IR spectra into self-consistent groups and then investigating their ancillary properties. This approach had led to a number of findings.

- The width and position of the narrow emission feature at ∼18.8 $\mu$m can distinguish between fullerene emission at 18.9 $\mu$m and [S III] emission at 18.7 $\mu$m.
- Combining this information with an assessment of the 17.4 $\mu$m fullerene feature and the structure of the 6–9 $\mu$m region can determine which spectra show fullerenes and which do not. This analysis adds three sources to the family of fullerene emitters: LIN 49, SMP LMC 008, and SMP SMC 001. It also also removes three previously identified fullerene candidates: SMP SMC 020, SMP SMC 027, and SMP LMC 099.
- We confirm that the big-11 feature is due primarily to SiC dust. In order to stay within abundance constraints, it is likely that the SiC is coating grains consisting of amorphous carbon.
- We have divided the sources showing Class D PAH emission at 7–9 $\mu$m into two groups based on their spectra at 11–14 $\mu$m. Class D1 spectra show an unusual profile with a strong 12.0 $\mu$m feature compared to the 12.7 $\mu$m feature. In Class D2, the features in the 11–14 $\mu$m range are shifted to ∼11.4, 12.4, and 13.2 $\mu$m.
- All of the PAH-like and some of the 21 $\mu$m spectra show Class D1 PAH emission. Removing SiC from the big-11 feature leaves a residual that resembles Class D1 PAHs. Not all Class D1 PAHs are associated with Class D PAHs at 6–9 $\mu$m.
- Over half of the 21 $\mu$m sources show Class D2 PAH emission at 11–14 $\mu$m, and all of these show Class D PAHs at 6–9 $\mu$m. Most of these sources are also associated with strong aliphatic emission at 6.9 $\mu$m.
- The 21 $\mu$m sources can show Class B, D1, or D2 PAH emission. The Class D2 PAH sources show the least extinguished line of sight to the central source.
- The 15.8 $\mu$m feature associated with 21 $\mu$m sources is fitted well with laboratory data from aliphatic hydrocarbon chains terminated with an alkyne CH group. The carrier of the 17.1 $\mu$m feature may be related.
- We attribute the 26–30 $\mu$m feature to MgS. This feature shifts from a central wavelength of ∼30 to ∼28 $\mu$m in the sequence Big-11 — Mixed — Fullerene — 21 $\mu$m, consistent with a shift in temperature of MgS from ∼200 to ∼400 K
- The Fullerene group shows the bluest $UBV$ colors in our sample, indicating a relatively clear line of sight to the ∼30,000 K stars at their center. From $K$ to [24], their infrared colors exhibit a remarkably narrow distribution. The colors of the Mixed group overlap those of the Fullerene group, but show a broader range.
- The optical spectrum of LIN 49, one of the newly detected fullerene sources, reveals a low-excitation PN and a cool central star, which is consistent with the other Fullerene sources.

The Fullerene, Mixed, and Big-11 groups form one family. They show fullerenes, mixtures of fullerenes and PAHs, or just PAHs in their spectra (respectively). Most show the big-11 and 26–30 $\mu$m features from what we believe to be grains coated with SiC and MgS, and the MgS feature typically peaks to the red of 29 $\mu$m, indicating lower dust temperatures. Previous studies have shown that fullerene emission is limited to those PNe with relatively cool central stars, and we confirm that result and extend it to the Big-11 spectra. The most significant new clue is the relatively clear view of the central star in the Fullerene group.

The 21 $\mu$m and PAH-like groups also form a family. Two of the PAH-like sources may in fact be 21 $\mu$m sources. All of the 21 $\mu$m spectra and half of the PAH-like group show clear evidence of aliphatic hydrocarbons in their spectra, and most show unusual Class D1 or D2 PAH emission profiles, with the Class D2 spectra associated with clearer lines of sight to the central nebula. Our identification of the 15.8 $\mu$m feature, which usually accompanies the 21 $\mu$m feature, with alkyne bonds in aliphatic chains, adds to the growing body of circumstantial evidence that the 21 $\mu$m feature is related to hydrocarbons. Aliphatics suggest less photo-processing, which is consistent with the earlier evolutionary phase suggested by the cooler central stars and thicker dust shells of the 21 $\mu$m sources.

We thank the referee, A. P. Jones, for a thorough report which led to substantial improvements in this pa-

TABLE 10
Continuum-fitting wavelengths

| Feature | Blue continuum ($\mu$m) | Red continuum ($\mu$m) |
|---|---|---|
| 6–9 $\mu$m combined flux | 5.90–5.99 | 9.00–9.12 |
| 6.2 $\mu$m PAH | 5.90–5.96 | 6.56–6.62 |
| 6.9 $\mu$m aliphatic | 6.68–6.75 | 7.05–7.11 |
| 7.3 $\mu$m aliphatic | 7.11–7.17 | 7.38–7.44 |
| 8.6 $\mu$m PAH | 8.21–8.33 | 8.82–8.94 |
| 7–9 $\mu$m base PAH feature | 6.65–6.74 | 9.00–9.12 |
| 6.5 $\mu$m fullerene-related | 6.29–6.35 | 6.74–6.80 |
| 7.0 $\mu$m fullerene | 6.80–6.86 | 7.26–7.32 |
| 7.6 $\mu$m fullerene-related | 7.29–7.38 | 7.90–8.03 |
| 8.1 $\mu$m fullerene-related | 7.84–7.97 | 8.21–8.33 |
| 8.5 $\mu$m fullerene | 8.21–8.33 | 8.82–8.94 |
| 17.4 $\mu$m fullerene | 16.82–16.98 | 17.75–17.92 |
| 18.7 $\mu$m [S III] | 18.34–18.52 | 19.02–19.20 |
| 18.9 $\mu$m fullerene | 18.17–18.34 | 19.45–19.61 |
| 18.7–18.9 $\mu$m gaussian | 18.25–18.43 | 19.28–19.45 |

per. We are grateful to P. R. Wood for providing the spectrum of LIN 49. G. C. S. was supported by NASA through Contract Number 1257184 issued by the Jet Propulsion Laboratory, California Institute of Technology under NASA contract 1407. F. K. received support from the National Science Council of Taiwan, grant NSC100-2112-M-001-023-MY3. This research relied on the following resources: NASA's Astrophysics Data System, the Infrared Science Archive at the Infrared Processing and Analysis Center, operated by JPL, and the SIMBAD and VizieR databases, operated at the Centre de Données astronomiques de Strasbourg.

## APPENDIX 1 SPECTRAL ANALYSIS

Our spectral analysis follows a standard sequence. We first simplified the overall structure in the spectra by fitting cubic splines and subtracting them. We chose the spline points so that the fitted continuum would pass through minima in the spectra; therefore, the spline points vary from one spectrum to the next. They are visible as diamonds in Figures 3 to 8. In cases where forbidden lines would interfere with estimates of the continuum around spectral features of interest, we replaced them with lines interpolated from the spectrum to either side before measuring feature strengths and positions. We removed the following lines: [Ar III] at 8.99 $\mu$m, [S IV] at 10.52 $\mu$m, [Ne II] at 12.81 $\mu$m, [Ne III] at 15.56 $\mu$m, [S III] at 33.5 $\mu$m, and [Si II] at 34.8 $\mu$m.

To extract central wavelengths and feature strengths we estimated a continuum by fitting line segments to the wavelengths given in Table 10 and integrating the flux density in between. The wavelengths used to fit line segments were fixed for all spectra, except the 21 $\mu$m sources (Appendix 1.3). The central wavelength $\lambda_C$ is defined as the position in the spectrum that bisects the integrated flux from the feature. Fitting a linear continuum is essential for accurate central wavelengths because they are sensitive to any residual slopes in the spectrum. The main purpose of the spline is to remove the curvature underneath the broader features to facilitate the fitting of line segments.

The use of line segments when measuring the PAH features assumes the presence of PAH plateaus, which have long been hypothesized to arise from larger PAH clusters and underlie the emission features (e.g. Allamandola et al. 1989; Bregman et al. 1989). Whether or not this assumption is correct, the line-segment method generates central wavelengths which are easily measured and reproduced, and which can be compared to similarly determined values from previous (and future) work. We rely on these wavelengths to identify and track the various spectral features. For the most part, our measurements of feature strengths first serve to check the validity of the central wavelength, and we have included them in the following tables even when we use them for only that purpose.

Other methods could also be used, most notably fitting of gaussians or other assumed feature profiles, from which the apparent plateaus can be built. Central wavelengths found using this method depend on the shape of the adopted profile shape, and because the method assumes that the plateaus do not exist, it forces the creation of a series of spectral components which can modify the apparent positions of the stronger features on which we are focused.

### *APPENDIX 1.1. 17–19 $\mu$m*

For the spectra with possible fullerene emission, we analyzed the 17–19 $\mu$m spectral region using our standard approach and a second method fitting gaussians to deblend the [S III] and fullerenes at 18.7–18.9 $\mu$m. To better understand the behavior of the [S III] line, we added a control sample of PNe with [S III] lines detected at a SNR of 2.5 $\sigma$ or better, but no fullerenes.

Table 11 presents the results for the program sources, while Table 12 presents the comparison sample of PNe. SMP LMC 099 appears in the latter table. In this and all data tables, $F$ is the integrated flux from a feature, $\lambda_C$ is the central wavelength of the feature, and $\lambda_O$ is the centroid wavelength based on a fitted gaussian. Wavelengths are not reported if the SNR of the extracted feature is less than 2.5. The gaussian centroids ($\lambda_O$) generally differ slightly from the central wavelengths determined by integration due to noise in the spectra and asymmetries in the features.

The results of the gaussian test appear in Section 3.3.1 and Figure 11. The relation between the width and position of the blended feature is tight, with the unambiguous fullerene spectra showing broader, redder features and the PNe showing narrower, bluer features. The PNe have a mean central wavelength of $18.73 \pm 0.01$ $\mu$m and a FWHM of $0.15 \pm 0.03$ $\mu$m, compared to $18.87 \pm 0.04$ $\mu$m and $0.39 \pm 0.05$ $\mu$m for the fullerene sources.[19] We used the results of the gaussian fitting to determine which set of continuum wavelengths in Table 10 to use when integrating the 18.9 $\mu$m feature.

Even when fullerenes are present, the LL spectra do not have the resolution to deblend the 18.9 $\mu$m feature from [S III] emission, which is most likely present. Thus the ratios of the strengths of the 17.4 and 18.9 $\mu$m features based on Table 11 will be lower than those determined from higher-resolution data or from model calculations

[19] We attribute the shift of 0.02 $\mu$m from the nominal position of the [S III] feature to uncertainties in the wavelength calibration; the shift amounts to about a quarter pixel.

TABLE 11
FULLERENE FEATURES AT 17.4 AND 18.9 $\mu$M

| Source | 17.4 $\mu$m fullerene feature | | 18.9 $\mu$m fullerene feature | | Gaussian fit to 18.9 $\mu$m | |
|---|---|---|---|---|---|---|
| | $\lambda_C(\mu m)$ | $F$ ($10^{-18}$ W m$^{-2}$) | $\lambda_C$ ($\mu$m) | $F$ ($10^{-18}$ W m$^{-2}$) | $\lambda_0$ ($\mu$m) | FWHM ($\mu$m) |
| SMP LMC 002 | 17.44 ± 0.05 | 35.4 ± 4.7 | 18.88 ± 0.03 | 49.6 ± 4.3 | 18.85 | 0.32 |
| SMP LMC 056 | 17.39 ± 0.11 | 22.4 ± 6.7 | 18.86 ± 0.02 | 80.7 ± 2.8 | 18.86 | 0.41 |
| SMP SMC 024 | 17.38 ± 0.08 | 18.8 ± 4.2 | 18.84 ± 0.03 | 63.6 ± 4.3 | 18.82 | 0.38 |
| LIN 49 | 17.41 ± 0.08 | 12.1 ± 2.4 | 18.93 ± 0.02 | 28.8 ± 1.3 | 18.93 | 0.40 |
| SMP SMC 016 | 17.44 ± 0.13 | 18.4 ± 5.2 | 18.90 ± 0.02 | 74.4 ± 2.8 | 18.90 | 0.45 |
| SMP SMC 013 | 17.41 ± 0.10 | 8.6 ± 2.4 | 18.82 ± 0.06 | 37.8 ± 4.5 | 18.83 | 0.47 |
| SMP SMC 018 | 17.37 ± 0.18 | 10.7 ± 4.1 | 18.86 ± 0.03 | 66.9 ± 4.0 | 18.85 | 0.38 |
| SMP SMC 015 | ··· | 12.3 ± 12.1 | 18.84 ± 0.15 | 32.5 ± 10.9 | 18.83 | 0.31 |
| SMP SMC 001 | ··· | 9.5 ± 5.1 | 18.88 ± 0.08 | 70.6 ± 9.4 | 18.89 | 0.55 |
| SMP LMC 008 | ··· | 22.4 ± 18.8 | 18.86 ± 0.08 | 59.6 ± 7.4 | 18.81 | 0.38 |
| SMP LMC 048 | ··· | 6.1 ± 6.9 | 18.78 ± 0.05 | 42.0 ± 7.7 | 18.76 | 0.22 |
| SMP LMC 025 | 17.23 ± 0.18 | 13.1 ± 5.6 | 18.79 ± 0.01 | 90.8 ± 3.3 | 18.77 | 0.28 |
| SMP LMC 085 | ··· | 23.4 ± 16.4 | ··· | 24.4 ± 12.8 | ··· | ··· |
| SMP LMC 076 | ··· | 7.0 ± 6.0 | 18.78 ± 0.08 | 25.8 ± 6.2 | 18.76 | 0.23 |
| SMP LMC 058 | 17.42 ± 0.21 | 20.8 ± 6.6 | ··· | ··· | ··· | ··· |
| SMP SMC 027 | 17.48 ± 0.16 | 55.9 ± 2.2 | 18.75 ± 0.04 | 14.4 ± 2.6 | 18.76 | 0.18 |
| SMP LMC 051 | 17.21 ± 0.11 | 16.3 ± 5.1 | 18.86 ± 0.21 | 21.5 ± 7.6 | 18.79 | 0.30 |
| IRAS 05370 | ··· | ··· | ··· | 14.0 ± 13.2 | ··· | ··· |
| IRAS 05537 | ··· | 11.1 ± 8.8 | ··· | 27.8 ± 12.8 | ··· | ··· |
| SMP SMC 020 | ··· | 0.8 ± 5.8 | ··· | 7.0 ± 3.9 | ··· | ··· |
| IRAS 05588 | ··· | 6.9 ± 13.9 | ··· | ··· | ··· | ··· |

TABLE 12
[S III] EMISSION IN THE PNE SAMPLE

| Source | [S III] emission line | | Gaussian fit to 18.9 $\mu$m | |
|---|---|---|---|---|
| | $\lambda_C$ ($\mu$m) | $F$ ($10^{-18}$ W m$^{-2}$) | $\lambda_0$ ($\mu$m) | FWHM ($\mu$m) |
| SMP SMC 005 | 18.74 ± 0.04 | 28.2 ± 5.0 | 18.73 | 0.19 |
| SMP SMC 008 | 18.70 ± 0.04 | 8.0 ± 2.2 | 18.72 | 0.15 |
| SMP LMC 004 | 18.74 ± 0.09 | 9.8 ± 3.4 | 18.73 | 0.18 |
| SMP LMC 009 | 18.76 ± 0.07 | 17.8 ± 5.4 | 18.76 | 0.09 |
| SMP LMC 010 | 18.73 ± 0.04 | 15.7 ± 4.9 | 18.73 | 0.12 |
| SMP LMC 016 | 18.73 ± 0.03 | 26.3 ± 5.4 | 18.74 | 0.15 |
| SMP LMC 019 | 18.72 ± 0.03 | 38.5 ± 9.8 | 18.73 | 0.13 |
| SMP LMC 021 | 18.73 ± 0.02 | 87.9 ± 13.1 | 18.73 | 0.15 |
| SMP LMC 034 | 18.73 ± 0.04 | 22.3 ± 5.6 | 18.75 | 0.16 |
| SMP LMC 038 | 18.75 ± 0.05 | 52.3 ± 11.5 | 18.73 | 0.14 |
| SMP LMC 040 | 18.68 ± 0.07 | 9.1 ± 3.6 | 18.72 | 0.17 |
| SMP LMC 045 | 18.74 ± 0.03 | 66.2 ± 12.8 | 18.74 | 0.13 |
| SMP LMC 053 | 18.72 ± 0.04 | 36.6 ± 10.4 | 18.73 | 0.12 |
| SMP LMC 061 | 18.76 ± 0.03 | 70.3 ± 10.9 | 18.76 | 0.16 |
| SMP LMC 066 | 18.77 ± 0.07 | 7.0 ± 2.8 | 18.76 | 0.08 |
| SMP LMC 062 | 18.72 ± 0.02 | 66.4 ± 7.8 | 18.72 | 0.15 |
| SMP LMC 071 | 18.73 ± 0.03 | 34.3 ± 6.3 | 18.73 | 0.15 |
| SMP LMC 079 | 18.74 ± 0.03 | 26.3 ± 6.4 | 18.75 | 0.14 |
| SMP LMC 080 | 18.73 ± 0.02 | 24.7 ± 2.9 | 18.73 | 0.16 |
| SMP LMC 087 | 18.73 ± 0.04 | 52.9 ± 11.8 | 18.74 | 0.13 |
| SMP LMC 095 | 18.72 ± 0.08 | 15.4 ± 5.3 | 18.72 | 0.21 |
| SMP LMC 099 | 18.74 ± 0.03 | 59.7 ± 9.3 | 18.74 | 0.16 |
| SMP LMC 100 | 18.72 ± 0.04 | 14.7 ± 4.7 | 18.73 | 0.13 |

(e.g. Bernard-Salas et al. 2012).

### *APPENDIX 1.2 6–9 $\mu m$*

We followed our standard method to measure the strengths and positions of the fullerene-related, PAH, and aliphatic hydrocarbon features. Tables 13, 14, and 15 present the results. For all of the spectra, we have integrated the total strength of the 6–9 $\mu$m emission complex and expressed the strengths of the individual features as a percentage of the flux from the overall complex.

We extracted features from the spectra after spline-fitting and removing a continuum and removing the forbidden lines when they were clearly present. Only [Ar III] at 8.99 $\mu$m would affect the analysis at 6–9 $\mu$m. The tables only list the sources where at least one feature of the relevant family has been detected at a SNR of at least 2.5 $\sigma$. When the fullerene and PAH features are too blended to disentangle, we do not report a result.

### *APPENDIX 1.3. LONGER WAVELENGTHS*

We adjusted our method to measure the strengths and positions of the features in the 21 $\mu$m spectra because they can shift from one spectrum to the next. Rather

TABLE 13
FULLERENE-RELATED FEATURES AT 6–9 $\mu$M

| Target | Total Feature Flux (6–9 $\mu$m) ($10^{-15}$ W m$^{-2}$) | 6.5 $\mu$m Feature $\lambda_C$ ($\mu$m) | 6.5 $\mu$m Feature Flux/Total (%) | 7.0 $\mu$m Feature $\lambda_C$ ($\mu$m) | 7.0 $\mu$m Feature Flux/Total (%) | 7.6 $\mu$m Feature $\lambda_C$ ($\mu$m) | 7.6 $\mu$m Feature Flux/Total (%) | 8.5 $\mu$m Feature $\lambda_C$ ($\mu$m) | 8.5 $\mu$m Feature Flux/Total (%) |
|---|---|---|---|---|---|---|---|---|---|
| SMP LMC 002 | 0.33 ± 0.01 | ··· | 1.2 ± 0.7 | 7.03 ± 0.01 | 18.9 ± 1.1 | 7.58 ± 0.02 | 8.9 ± 0.5 | 8.51 ± 0.02 | 5.4 ± 0.4 |
| SMP LMC 056 | 0.44 ± 0.02 | 6.55 ± 0.05 | 9.9 ± 1.4 | 7.03 ± 0.01 | 24.9 ± 1.7 | ··· | 3.5 ± 1.5 | 8.50 ± 0.02 | 3.8 ± 0.4 |
| SMP SMC 024 | 0.57 ± 0.01 | 6.54 ± 0.03 | 3.6 ± 0.3 | 7.03 ± 0.01 | 11.1 ± 0.7 | 7.58 ± 0.03 | 8.7 ± 0.8 | 8.51 ± 0.04 | 2.9 ± 0.4 |
| LIN 49 | 0.59 ± 0.01 | 6.53 ± 0.02 | 8.6 ± 0.6 | 7.04 ± 0.01 | 8.1 ± 0.5 | 7.57 ± 0.02 | 5.5 ± 0.5 | 8.52 ± 0.15 | 1.6 ± 0.6 |
| SMP SMC 016 | 0.84 ± 0.02 | 6.54 ± 0.03 | 7.8 ± 1.1 | 7.05 ± 0.02 | 9.2 ± 0.9 | 7.59 ± 0.06 | 5.9 ± 0.9 | 8.52 ± 0.04 | 1.8 ± 0.4 |
| SMP SMC 018 | 0.97 ± 0.04 | 6.54 ± 0.06 | 2.6 ± 0.8 | 7.04 ± 0.05 | 4.8 ± 0.8 | 7.59 ± 0.03 | 9.5 ± 0.8 | ··· | ··· |
| SMP SMC 015 | 0.60 ± 0.01 | ··· | 1.4 ± 0.8 | 7.06 ± 0.04 | 5.1 ± 0.9 | 7.59 ± 0.02 | 15.0 ± 0.8 | ··· | ··· |
| SMP LMC 008 | 0.84 ± 0.03 | ··· | −11.4 ± 1.8 | ··· | −2.4 ± 0.5 | 7.57 ± 0.11 | 13.4 ± 3.0 | ··· | ··· |
| SMP LMC 048 | 1.07 ± 0.05 | ··· | −0.3 ± 2.4 | 7.05 ± 0.04 | 9.8 ± 1.6 | 7.62 ± 0.05 | 10.8 ± 1.8 | ··· | ··· |
| SMP LMC 025 | 0.93 ± 0.03 | ··· | −1.7 ± 0.8 | 7.03 ± 0.07 | 2.4 ± 0.7 | 7.58 ± 0.02 | 10.1 ± 0.6 | ··· | ··· |
| SMP SMC 027 | 0.04 ± 0.01 | ··· | 13.0 ± 7.2 | ··· | 4.8 ± 14.5 | 7.56 ± 0.10 | 43.4 ± 14.6 | ··· | ··· |
| IRAS 05537 | 0.70 ± 0.07 | ··· | −16.2 ± 2.8 | ··· | −3.7 ± 1.8 | 7.61 ± 0.04 | 29.3 ± 2.9 | ··· | ··· |

TABLE 14
PAH FEATURES AT 6–9 $\mu$M

| Target | Total Feature Flux (6–9 $\mu$m) ($10^{-15}$ W m$^{-2}$) | 6.2 $\mu$m Feature $\lambda_C$ ($\mu$m) | 6.2 $\mu$m Feature Flux/Total (%) | 8.6 $\mu$m Feature $\lambda_C$ ($\mu$m) | 8.6 $\mu$m Feature Flux/Total (%) | 7–9 $\mu$m Complex $\lambda_C$ ($\mu$m) | 7–9 $\mu$m Complex Flux/Total (%) |
|---|---|---|---|---|---|---|---|
| SMP SMC 013 | 0.59 ± 0.02 | 6.25 ± 0.13 | 3.9 ± 1.5 | 8.58 ± 0.05 | 3.3 ± 0.4 | 7.73 ± 0.05 | 42 ± 2 |
| SMP SMC 018 | 0.97 ± 0.04 | 6.27 ± 0.11 | 3.8 ± 1.1 | 8.60 ± 0.04 | 2.1 ± 0.3 | 7.59 ± 0.04 | 47 ± 2 |
| SMP SMC 015 | 0.60 ± 0.01 | 6.33 ± 0.05 | 5.4 ± 0.8 | 8.59 ± 0.03 | 3.5 ± 0.4 | 7.57 ± 0.03 | 44 ± 2 |
| SMP SMC 001 | 1.16 ± 0.03 | 6.25 ± 0.00 | 18.2 ± 0.5 | 8.61 ± 0.05 | 4.8 ± 1.0 | 7.75 ± 0.02 | 65 ± 2 |
| SMP LMC 008 | 0.84 ± 0.03 | 6.26 ± 0.00 | 25.1 ± 0.7 | ··· | 4.0 ± 2.0 | 7.66 ± 0.06 | 50 ± 4 |
| SMP LMC 048 | 1.07 ± 0.05 | 6.31 ± 0.05 | 14.4 ± 2.5 | ··· | 0.7 ± 0.5 | 7.58 ± 0.08 | 56 ± 4 |
| SMP LMC 025 | 0.93 ± 0.03 | 6.27 ± 0.03 | 8.7 ± 1.2 | 8.60 ± 0.06 | 2.2 ± 0.5 | 7.60 ± 0.03 | 48 ± 1 |
| SMP LMC 085 | 1.42 ± 0.03 | 6.26 ± 0.00 | 21.8 ± 0.6 | 8.59 ± 0.02 | 4.5 ± 0.4 | 7.67 ± 0.03 | 60 ± 2 |
| SMP LMC 076 | 0.66 ± 0.02 | 6.26 ± 0.00 | 17.6 ± 0.4 | 8.63 ± 0.04 | 3.7 ± 0.5 | 7.78 ± 0.02 | 69 ± 2 |
| SMP LMC 058 | 1.67 ± 0.18 | 6.26 ± 0.01 | 24.0 ± 1.3 | 8.62 ± 0.05 | 2.7 ± 0.6 | 7.91 ± 0.01 | 70 ± 1 |
| SMP SMC 027 | 0.04 ± 0.01 | ··· | 8.4 ± 18.4 | ··· | 13.6 ± 5.7 | ··· | 32 ± 28 |
| SMP LMC 051 | 2.59 ± 0.08 | 6.25 ± 0.01 | 19.8 ± 1.1 | 8.63 ± 0.03 | 3.8 ± 0.5 | 7.88 ± 0.02 | 66 ± 2 |
| IRAS 05370 | 1.21 ± 1.62 | 6.25 ± 0.01 | 39.1 ± 1.3 | 8.64 ± 0.02 | 9.4 ± 0.9 | 7.73 ± 0.03 | 51 ± 3 |
| IRAS 05537 | 0.70 ± 0.07 | 6.25 ± 0.01 | 40.5 ± 2.0 | 8.59 ± 0.03 | 12.9 ± 1.6 | 7.61 ± 0.07 | 60 ± 8 |
| SMP SMC 020 | 0.26 ± 0.02 | 6.23 ± 0.03 | 24.6 ± 3.9 | ··· | 1.7 ± 1.3 | 7.83 ± 0.08 | 16 ± 4 |
| IRAS 05588 | 8.03 ± 0.09 | 6.23 ± 0.00 | 15.4 ± 0.3 | 8.59 ± 0.03 | 5.3 ± 0.6 | 7.76 ± 0.01 | 69 ± 2 |
| SMP SMC 006 | 1.49 ± 0.04 | 6.25 ± 0.01 | 16.4 ± 0.9 | 8.63 ± 0.02 | 2.7 ± 0.3 | 7.81 ± 0.02 | 65 ± 2 |
| IRAS 05073 | 1.93 ± 0.04 | 6.25 ± 0.01 | 11.9 ± 0.8 | ··· | 0.5 ± 0.5 | 7.83 ± 0.03 | 65 ± 2 |
| IRAS 05063 | 0.74 ± 0.04 | 6.26 ± 0.02 | 20.1 ± 1.8 | ··· | 1.1 ± 1.2 | ··· | ··· |
| IRAS 05413 | 0.78 ± 0.12 | 6.24 ± 0.12 | 37.5 ± 10.2 | ··· | 7.2 ± 5.3 | 7.74 ± 0.17 | 97 ± 12 |
| IRAS 00350 | 2.25 ± 0.17 | 6.29 ± 0.01 | 4.3 ± 0.9 | 8.64 ± 0.04 | 8.8 ± 1.4 | 7.84 ± 0.03 | 90 ± 4 |
| IRAS 05127 | 2.74 ± 0.09 | 6.25 ± 0.01 | 16.2 ± 0.6 | 8.60 ± 0.01 | 4.3 ± 0.3 | 7.72 ± 0.02 | 59 ± 1 |
| J010546 | 2.31 ± 0.04 | 6.23 ± 0.01 | 9.9 ± 0.5 | 8.59 ± 0.02 | 4.0 ± 0.3 | 7.82 ± 0.02 | 65 ± 1 |
| IRAS F05192 | 4.16 ± 0.13 | 6.27 ± 0.04 | 9.2 ± 1.5 | 8.61 ± 0.03 | 3.8 ± 0.4 | 7.89 ± 0.03 | 66 ± 2 |
| J052043 | 0.97 ± 0.02 | 6.24 ± 0.01 | 9.3 ± 0.4 | 8.59 ± 0.09 | 1.9 ± 0.5 | 7.84 ± 0.04 | 69 ± 2 |
| IRAS 05110 | 3.79 ± 0.03 | 6.26 ± 0.00 | 7.7 ± 0.1 | 8.57 ± 0.08 | 0.7 ± 0.2 | 7.80 ± 0.04 | 61 ± 2 |
| IRAS Z05259 | 1.38 ± 0.03 | 6.25 ± 0.01 | 8.1 ± 0.3 | 8.58 ± 0.04 | 2.5 ± 0.3 | 7.83 ± 0.03 | 68 ± 2 |
| J004441 | 1.78 ± 0.01 | 6.24 ± 0.00 | 9.7 ± 0.2 | 8.61 ± 0.05 | 1.0 ± 0.2 | 7.81 ± 0.03 | 57 ± 2 |
| NGC 1978 WBT 2665 | 3.24 ± 0.06 | 6.23 ± 0.02 | 9.0 ± 1.0 | ··· | −0.0 ± 0.2 | 7.87 ± 0.05 | 50 ± 2 |
| IRAS 06111 | 5.13 ± 0.04 | 6.25 ± 0.00 | 10.9 ± 0.2 | ··· | 0.4 ± 0.2 | 7.86 ± 0.02 | 57 ± 1 |
| IRAS 05092 | 7.48 ± 0.07 | 6.24 ± 0.00 | 15.1 ± 0.2 | 8.61 ± 0.02 | 5.2 ± 0.3 | 7.79 ± 0.01 | 59 ± 0 |
| IRAS 05185 | 14.65 ± 0.16 | 6.25 ± 0.00 | 15.6 ± 0.2 | 8.62 ± 0.02 | 5.9 ± 0.4 | 7.82 ± 0.01 | 59 ± 1 |
| IRAS 05360 | 9.95 ± 0.10 | 6.25 ± 0.00 | 15.2 ± 0.2 | 8.62 ± 0.02 | 5.9 ± 0.4 | 7.84 ± 0.01 | 59 ± 1 |
| SMP SMC 011 | 2.43 ± 0.10 | 6.23 ± 0.00 | 32.7 ± 0.6 | 8.58 ± 0.05 | 4.7 ± 1.0 | 7.68 ± 0.03 | 73 ± 2 |
| IRAS 05315 | 0.21 ± 0.05 | ··· | −8.9 ± 14.5 | ··· | 0.2 ± 9.2 | 8.15 ± 0.26 | 92 ± 27 |
| IRAS 05495 | 0.37 ± 0.03 | 6.21 ± 0.10 | 11.1 ± 3.1 | ··· | 4.7 ± 3.9 | 7.98 ± 0.08 | 91 ± 7 |
| SMP LMC 099 | 0.94 ± 0.04 | 6.29 ± 0.03 | 12.7 ± 1.7 | ··· | 2.6 ± 1.1 | 7.87 ± 0.04 | 68 ± 3 |

TABLE 15
ALIPHATIC HYDROCARBON FEATURES AT 6–9 $\mu$M

| Target | Total Feature Flux (6–9 $\mu$m) ($10^{-15}$ W m$^{-2}$) | 6.9 $\mu$m Feature $\lambda_C$ ($\mu$m) | 6.9 $\mu$m Feature Flux/Total (%) | 7.3 $\mu$m Feature $\lambda_C$ ($\mu$m) | 7.3 $\mu$m Feature Flux/Total (%) |
|---|---|---|---|---|---|
| SMP SMC 020 | 0.26 ± 0.02 | 6.83 ± 0.08 | 4.8 ± 1.3 | ··· | 3.5 ± 2.2 |
| IRAS 05588 | 8.03 ± 0.09 | 6.91 ± 0.02 | 2.1 ± 0.2 | ··· | −0.9 ± 0.3 |
| IRAS 05073 | 1.93 ± 0.04 | 6.90 ± 0.01 | 12.5 ± 0.9 | ··· | −0.0 ± 0.5 |
| IRAS 05063 | 0.74 ± 0.04 | 6.92 ± 0.03 | 7.0 ± 1.1 | ··· | 0.6 ± 0.7 |
| IRAS 05413 | 0.78 ± 0.12 | 6.85 ± 0.05 | 10.0 ± 3.5 | ··· | −3.9 ± 4.8 |
| IRAS 00350 | 2.25 ± 0.17 | ··· | −3.1 ± 1.2 | 7.24 ± 0.04 | 2.0 ± 0.6 |
| J010546 | 2.31 ± 0.04 | 6.91 ± 0.05 | 0.9 ± 0.2 | ··· | −0.0 ± 0.3 |
| IRAS F05192 | 4.16 ± 0.13 | 6.95 ± 0.05 | 2.1 ± 0.6 | ··· | 0.4 ± 0.8 |
| J052043 | 0.97 ± 0.02 | 6.90 ± 0.02 | 3.9 ± 0.3 | 7.28 ± 0.04 | 0.8 ± 0.2 |
| IRAS 05110 | 3.79 ± 0.03 | 6.89 ± 0.00 | 12.8 ± 0.3 | 7.28 ± 0.00 | 2.6 ± 0.1 |
| IRAS Z05259 | 1.38 ± 0.03 | 6.92 ± 0.03 | 2.7 ± 0.4 | 7.29 ± 0.03 | 0.4 ± 0.1 |
| J004441 | 1.78 ± 0.01 | 6.89 ± 0.00 | 10.5 ± 0.3 | 7.28 ± 0.01 | 1.8 ± 0.2 |
| NGC 1978 WBT 2665 | 3.24 ± 0.06 | 6.91 ± 0.01 | 15.2 ± 1.2 | 7.27 ± 0.02 | 2.5 ± 0.4 |
| IRAS 06111 | 5.13 ± 0.04 | 6.90 ± 0.01 | 11.4 ± 0.4 | 7.27 ± 0.01 | 1.5 ± 0.1 |
| IRAS 05092 | 7.48 ± 0.07 | 6.90 ± 0.01 | 1.3 ± 0.1 | ··· | −0.3 ± 0.1 |
| IRAS 05185 | 14.65 ± 0.16 | 6.91 ± 0.01 | 1.0 ± 0.1 | ··· | −0.3 ± 0.1 |
| IRAS 05360 | 9.95 ± 0.10 | 6.92 ± 0.02 | 0.8 ± 0.1 | ··· | −0.3 ± 0.1 |
| SMP SMC 011 | 2.43 ± 0.10 | 6.92 ± 0.01 | 1.9 ± 0.2 | ··· | −2.8 ± 0.6 |

TABLE 16
FEATURES IN THE 21 $\mu$M SPECTRA

| Target | Total Feature Flux (5–37 $\mu$m) ($10^{-15}$ W m$^{-2}$) | 6–9 $\mu$m Flux/Total (%) | 11–14 $\mu$m Flux/Total (%) | 16 $\mu$m Complex $\lambda_C$ ($\mu$m) | 16 $\mu$m Complex Flux/Total (%) | 21 $\mu$m Feature $\lambda_C$ ($\mu$m) | 21 $\mu$m Feature Flux/Total (%) | 26–30 $\mu$m Featur $\lambda_C$ ($\mu$m) | 26–30 $\mu$m Featur Flux/ (% |
|---|---|---|---|---|---|---|---|---|---|
| J010546 | 5.01 ± 0.03 | 60.9 ± 0.3 | 30.8 ± 0.2 | 16.75 ± 0.17 | 1.5 ± 0.1 | 20.62 ± 0.25 | 2.5 ± 0.2 | 28.07 ± 0.58 | 3.2 |
| IRAS F05192 | 14.68 ± 0.15 | 42.9 ± 0.6 | 26.2 ± 0.3 | 16.83 ± 0.54 | 0.8 ± 0.1 | 20.44 ± 0.05 | 12.9 ± 0.3 | 28.90 ± 0.27 | 13.8 |
| J052043 | 4.30 ± 0.04 | 29.4 ± 0.3 | 23.2 ± 0.7 | 15.98 ± 0.05 | 5.6 ± 0.2 | 20.35 ± 0.03 | 17.3 ± 0.2 | 28.72 ± 0.09 | 23.3 |
| IRAS 05110 | 12.99 ± 0.07 | 31.0 ± 0.2 | 29.2 ± 0.4 | 16.23 ± 0.05 | 2.1 ± 0.1 | 20.40 ± 0.04 | 4.4 ± 0.1 | 28.46 ± 0.04 | 30.6 |
| IRAS Z05259 | 5.95 ± 0.03 | 29.7 ± 0.2 | 33.9 ± 0.3 | 16.07 ± 0.08 | 3.4 ± 0.2 | 20.43 ± 0.01 | 22.8 ± 0.1 | 28.33 ± 0.13 | 9.3 |
| J004441 | 4.21 ± 0.03 | 46.9 ± 0.2 | 31.8 ± 0.3 | 16.11 ± 0.11 | 3.2 ± 0.2 | 20.32 ± 0.11 | 6.6 ± 0.3 | 28.63 ± 0.24 | 8.6 |
| NGC 1978 WBT 2665 | 13.37 ± 0.08 | 23.4 ± 0.4 | 28.1 ± 0.1 | 16.69 ± 0.17 | 1.5 ± 0.1 | 20.60 ± 0.23 | 0.4 ± 0.1 | 28.00 ± 0.03 | 46.0 |
| IRAS 06111 | 14.49 ± 0.06 | 30.2 ± 0.2 | 31.2 ± 0.2 | 16.99 ± 0.09 | 1.1 ± 0.1 | 20.55 ± 0.34 | 0.4 ± 0.1 | 28.17 ± 0.04 | 36.7 |
| IRAS 05092 | 14.16 ± 0.04 | 55.9 ± 0.2 | 29.3 ± 0.1 | 16.21 ± 0.11 | 2.1 ± 0.1 | 20.57 ± 0.04 | 3.4 ± 0.1 | 28.60 ± 0.09 | 8.7 |
| IRAS 05185 | 28.44 ± 0.10 | 63.3 ± 0.3 | 21.7 ± 0.0 | 16.80 ± 0.03 | 1.8 ± 0.0 | 20.51 ± 0.04 | 3.1 ± 0.1 | 28.87 ± 0.07 | 9.4 |
| IRAS 05360 | 21.23 ± 0.09 | 60.0 ± 0.2 | 20.9 ± 0.3 | 16.99 ± 0.04 | 1.5 ± 0.1 | 20.41 ± 0.20 | 0.4 ± 0.1 | 28.58 ± 0.05 | 16.9 |
| IRAS 05073 | 10.43 ± 0.07 | 18.8 ± 0.3 | 28.9 ± 0.3 | 16.86 ± 0.39 | 1.6 ± 0.2 | ··· | 0.1 ± 0.2 | 28.10 ± 0.05 | 48.1 |
| IRAS 05063 | 7.93 ± 0.05 | 8.9 ± 0.3 | 40.6 ± 0.3 | 17.13 ± 0.22 | 0.9 ± 0.2 | 20.55 ± 0.35 | 1.3 ± 0.2 | 28.04 ± 0.05 | 46.4 |
| IRAS 05413 | 6.82 ± 0.21 | 14.9 ± 1.7 | 39.4 ± 0.8 | ··· | −0.1 ± 0.2 | 20.14 ± 1.53 | 1.3 ± 0.4 | 27.90 ± 0.18 | 40.6 |

TABLE 17
THE 26–30 $\mu$M FEATURE

| Target | Total Feature Flux (5–37 $\mu$m) ($10^{-15}$ W m$^{-2}$) | 26–30 $\mu$m Feature $\lambda_C$ ($\mu$m) | Flux/Total (%) |
|---|---|---|---|
| SMP LMC 002 | 0.95 ± 0.02 | 30.08 ± 0.56 | 18.9 ± 1.2 |
| SMP LMC 056 | 1.00 ± 0.02 | 30.15 ± 0.52 | 13.4 ± 1.1 |
| SMP SMC 024 | 1.43 ± 0.02 | ··· | 18.9 ± 1.0 |
| LIN 49 | 1.19 ± 0.01 | 29.32 ± 0.11 | 21.2 ± 0.3 |
| SMP SMC 016 | 1.79 ± 0.03 | 29.96 ± 0.21 | 11.8 ± 0.4 |
| SMP SMC 013 | 1.53 ± 0.03 | ··· | 6.7 ± 0.5 |
| SMP SMC 018 | 3.69 ± 0.03 | 31.03 ± 0.17 | 8.4 ± 0.2 |
| SMP SMC 015 | 4.60 ± 0.04 | 30.24 ± 0.17 | 6.0 ± 0.2 |
| SMP SMC 001 | 5.71 ± 0.05 | 31.09 ± 0.29 | 5.1 ± 0.2 |
| SMP LMC 008 | 10.39 ± 0.13 | 30.17 ± 0.14 | 10.9 ± 0.2 |
| SMP LMC 048 | 4.54 ± 0.06 | 29.79 ± 0.07 | 25.6 ± 0.2 |
| SMP LMC 025 | 4.78 ± 0.05 | 29.72 ± 0.07 | 28.0 ± 0.3 |
| SMP LMC 085 | 9.09 ± 0.06 | 30.03 ± 0.09 | 16.0 ± 0.2 |
| SMP LMC 076 | 3.06 ± 0.02 | 30.04 ± 0.39 | 5.2 ± 0.3 |
| SMP LMC 058 | 8.77 ± 0.08 | 31.23 ± 0.38 | 2.2 ± 0.2 |
| SMP SMC 027 | 0.57 ± 0.03 | ··· | 25.2 ± 1.4 |
| SMP LMC 051 | 10.21 ± 0.08 | 30.86 ± 0.32 | 3.8 ± 0.3 |
| IRAS 05370 | 16.87 ± 0.06 | ··· | 0.4 ± 0.2 |
| IRAS 05537 | 11.93 ± 0.07 | 31.08 ± 0.33 | 4.8 ± 0.3 |
| SMP SMC 020 | 3.83 ± 0.03 | ··· | 0.4 ± 0.1 |
| IRAS 05588 | 18.72 ± 0.15 | ··· | 0.9 ± 0.1 |
| SMP SMC 006 | 6.42 ± 0.04 | 31.51 ± 0.36 | 4.7 ± 0.2 |
| IRAS 00350 | 8.15 ± 0.15 | 27.34 ± 0.10 | 30.8 ± 0.4 |
| IRAS 05127 | 9.03 ± 0.05 | 28.83 ± 0.06 | 44.5 ± 0.3 |
| SMP SMC 011 | 12.28 ± 0.17 | ··· | −0.4 ± 0.5 |
| IRAS 05315 | 9.52 ± 0.14 | 27.52 ± 0.11 | 47.2 ± 0.6 |
| IRAS 05495 | 7.99 ± 0.08 | 28.32 ± 0.10 | 56.5 ± 0.6 |
| SMP SMC 025 | 0.90 ± 0.02 | ··· | 13.8 ± 0.8 |
| SMP LMC 099 | 2.81 ± 0.10 | ··· | 22.1 ± 1.5 |

than use fixed wavelengths to set the continuum, we have allowed the wavelengths for integration to vary by setting them to the minima in the spline-removed spectra in intervals on either side of the features.

Table 16 presents the total integrated fluxes for all features, and for individual features, the central wavelength and the strength as a percentage of the total feature flux. We do not report a central wavelength for features detected at less that 2.5 $\sigma$. The features are integrated between the minima found in the following intervals: 5–6, 9–10.2, 13.8–15.2, 17–19, 22–26, and 35–37 $\mu$m. We have also zeroed negative data to the red of 35 $\mu$m (after finding the position of the minimum) to reduce the impact of a poorly determined spline at the boundary of the data.

Table 16 includes a column giving the central wavelength and fraction of the flux from the 26–30 $\mu$m emission feature for the eleven 21 $\mu$m sources and the three 21 $\mu$m candidates. Table 17 provides the same data for the remainder of the sample. Some spectra do not show a 26–30 $\mu$m feature or show it with only a low SNR. In others, the spectrum actually climbs at the longest wavelengths, possibly due to background subtraction issues. In these cases, we have not reported a central wavelength.

## APPENDIX 2. PHOTOMETRY

To assemble optical and infrared photometry for our sample, we began with the observed IRS coordinates, as determined by the optimal extraction, then found the counterpart point source as observed by IRAC in either the SAGE or SAGE-SMC catalogs (Meixner et al. 2006; Gordon et al. 2011).[20] The SAGE-SMC catalog includes updated photometry from the earlier S$^3$MC survey of the core of the SMC (Bolatto et al. 2007). IRAC observed all sources except IRAS 06111 and SMP LMC 099, which lie outside the SAGE footprint. The SMC sources LIN 49 and IRAS 00350 are $\sim$2″ and 4.″5, respectively, away from their position as given by SIMBAD.

Using the new coordinates, we searched the 2MASS catalog (Skrutskie et al. 2006), and where we found a source, again updated the coordinates. We then searched several additional catalogs. The 2MASS-6X catalog covers the Magellanic Clouds with deeper sensitivity and in multiple epochs (Cutri et al. 2006). The Infrared Survey Facility (IRSF) also surveyed the Magellanic Clouds at $JHK_s$ and provides additional temporal coverage (Kato et al. 2007). The Third Release of the DENIS catalog extended our temporal coverage at $J$ and $K_s$.[21] Cioni et al. (2000) introduced the original DENIS point-source catalog of the Magellanic Clouds. We also used the WISE survey for additional coverage at 3.4 and 4.6 $\mu$m (Wright et al. 2010).[22]

We used the IRSA website to access all of the catalogs except the IRSF catalog, which we obtained through VizieR.[23] We assumed equivalence in closely overlapping photometric filters. Thus we did not distinguish for differences in near-IR filters, and we combined WISE data at 3.4 and 4.6 $\mu$m with IRAC data at 3.6 and 4.5 $\mu$m, respectively.

Table 18 presents the combined infrared photometry for our sample. The coordinates reported in Table 1 are an average of the sources reported in the 2MASS, 2MASS 6X, and IRSF surveys, with equal weight assigned for each epoch in which the source was observed. None of those surveys detected IRAS 05495, and for it we report the mean IRAC position. We estimate, based on discrepancies between positions for a given source among the catalogs, that the positions we report are good to $\sim$0.″2 in most cases.

Table 19 presents the combined optical photometry. We obtained $UBVI$ photometry from the Magellanic Clouds Photometric Survey of the SMC (Zaritsky et al. 2002) and LMC (Zaritsky et al. 2004), supplemented with $I$-band data from DENIS and data from the OGLE-III shallow survey of the LMC (Ulaczyk et al. 2012).[24] Again, we did not distinguish between differences in filters and simply combined all available data for each source in each filter.

Table 19 also contains a column of absolute bolometric magnitudes, which are found by integrating through the IRS data and the available photometry to the blue of 5 $\mu$m. We assumed a Wien distribution to the blue of the available data and a Rayleigh-Jeans distribution to the red of the IRS data. The absolute bolometric magnitude

[20] IRAC = Infrared Array Camera on *Spitzer*; SAGE = Surveying the Agents of Galactic Evolution.
[21] DENIS = Deep Near-Infrared Survey.
[22] WISE = Wide-field Infrared Survey experiment.
[23] IRSA = Infrared Science Archive, maintained by NASA and the Infrared Processing and Analysis Center (IPAC) at Caltech, and available at http://irsa.ipac.caltech.edu.
[24] OGLE = Optical Gravitational Lens Experiment.

TABLE 18
Combined near- and mid-infrared photometry

| Target | $J$ | $H$ | $K_s$ | [3.6] | [4.5] | [5.8] | [8.0] | [24] |
|---|---|---|---|---|---|---|---|---|
| SMP LMC 002 | 16.83 ± 0.06 | 16.43 ± 0.09 | 15.39 ± 0.08 | 13.78 ± 0.09 | 12.81 ± 0.02 | 12.05 ± 0.04 | 10.52 ± 0.01 | 7.40 ± 0.02 |
| SMP LMC 056 | 15.74 ± 1.68 | 15.04 ± 1.96 | 15.22 ± 0.21 | 13.47 ± 0.20 | 12.48 ± 0.06 | 11.73 ± 0.04 | 10.13 ± 0.00 | 6.76 ± 0.00 |
| SMP SMC 024 | 16.18 ± 0.13 | 15.73 ± 0.08 | 14.68 ± 0.02 | 13.11 ± 0.18 | 12.26 ± 0.06 | 11.47 ± 0.01 | 9.76 ± 0.04 | 6.06 ± 0.04 |
| LIN 49 | 16.58 ± 0.08 | 15.72 ± 0.07 | 14.51 ± 0.15 | 12.93 ± 0.14 | 12.17 ± 0.03 | 11.33 ± 0.05 | 9.74 ± 0.01 | 6.47 ± 0.04 |
| SMP SMC 016 | 16.05 ± 0.10 | 15.28 ± 0.09 | 14.08 ± 0.15 | 12.57 ± 0.16 | 11.72 ± 0.03 | 10.90 ± 0.04 | 9.29 ± 0.04 | 5.98 ± 0.06 |
| SMP SMC 013 | 16.04 ± 0.10 | 15.73 ± 0.10 | 14.57 ± 0.43 | 13.24 ± 0.17 | 12.37 ± 0.08 | 11.35 ± 0.01 | 9.50 ± 0.04 | 5.71 ± 0.02 |
| SMP SMC 018 | 15.31 ± 0.31 | 14.85 ± 0.24 | 14.01 ± 0.41 | 12.37 ± 0.10 | 11.45 ± 0.03 | 10.32 ± 0.01 | 8.60 ± 0.00 | 4.46 ± 0.02 |
| SMP SMC 015 | 15.56 ± 0.19 | 15.31 ± 0.05 | 14.13 ± 0.13 | 12.56 ± 0.17 | 11.49 ± 0.03 | 10.30 ± 0.00 | 8.53 ± 0.02 | 4.50 ± 0.00 |
| SMP SMC 001 | 16.15 ± 0.03 | 15.48 ± 0.04 | 14.49 ± 0.11 | 12.57 ± 0.12 | 11.56 ± 0.04 | 10.12 ± 0.03 | 8.33 ± 0.00 | 4.13 ± 0.01 |
| SMP LMC 008 | 15.63 ± 0.16 | 15.60 ± 0.17 | 14.40 ± 0.06 | 12.35 ± 0.25 | 10.95 ± 0.01 | 9.54 ± 0.00 | 7.81 ± 0.00 | 3.26 ± 0.02 |
| SMP LMC 048 | 15.39 ± 0.05 | 14.10 ± 1.46 | 13.17 ± 1.45 | 11.82 ± 1.32 | 11.16 ± 1.11 | 10.63 ± 0.03 | 8.88 ± 0.00 | 4.35 ± 0.07 |
| SMP LMC 025 | 15.50 ± 0.04 | 15.25 ± 0.10 | 14.23 ± 0.13 | 12.61 ± 0.02 | 11.76 ± 0.07 | 10.68 ± 0.03 | 8.83 ± 0.01 | 4.24 ± 0.00 |
| SMP LMC 085 | 15.46 ± 0.12 | 15.16 ± 0.07 | 14.01 ± 0.14 | 12.38 ± 0.22 | 11.28 ± 0.01 | 9.75 ± 0.02 | 7.93 ± 0.01 | 3.42 ± 0.04 |
| SMP LMC 076 | 15.85 ± 0.20 | 15.97 ± 0.06 | 15.04 ± 0.02 | 13.46 ± 0.25 | 12.47 ± 0.07 | 10.89 ± 0.06 | 9.01 ± 0.04 | 4.66 ± 0.03 |
| SMP LMC 058 | 15.62 ± 0.17 | 15.53 ± 0.09 | 14.53 ± 0.03 | 12.27 ± 0.24 | 11.08 ± 0.02 | 9.70 ± 0.01 | 8.08 ± 0.01 | 4.00 ± 0.01 |
| SMP SMC 027 | 16.02 ± 0.09 | 15.87 ± 0.48 | 15.37 ± 0.05 | 14.01 ± 0.26 | 13.26 ± 0.04 | 12.73 ± 0.01 | 10.87 ± 0.03 | 6.15 ± 0.05 |
| SMP LMC 051 | 15.84 ± 0.12 | 15.61 ± 0.02 | 14.23 ± 0.07 | 11.87 ± 0.24 | 10.68 ± 0.03 | 9.17 ± 0.02 | 7.40 ± 0.01 | 3.30 ± 0.01 |
| IRAS 05370 | 17.50 ± 0.37 | 16.49 ± 0.01 | 15.19 ± 0.03 | 12.04 ± 0.19 | 10.76 ± 0.14 | 9.20 ± 0.04 | 7.39 ± 0.01 | 2.96 ± 0.02 |
| IRAS 05537 | 16.38 ± 0.14 | 15.93 ± 0.18 | 15.03 ± 0.08 | 12.97 ± 0.30 | 11.91 ± 0.04 | 9.90 ± 0.00 | 7.74 ± 0.05 | 3.00 ± 0.00 |
| SMP SMC 020 | 15.88 ± 0.14 | 15.98 ± 0.04 | 15.06 ± 0.04 | 12.90 ± 0.28 | 11.48 ± 0.01 | 10.26 ± 0.04 | 8.72 ± 0.03 | ··· |
| IRAS 05588 | 14.64 ± 0.06 | 14.30 ± 0.22 | 13.41 ± 0.35 | 11.50 ± 0.32 | 10.48 ± 0.21 | 8.83 ± 0.09 | 6.78 ± 0.03 | 3.04 ± 0.01 |
| SMP SMC 006 | 15.91 ± 0.21 | 15.87 ± 0.14 | 14.95 ± 0.07 | 12.75 ± 0.24 | 11.54 ± 0.02 | 9.90 ± 0.04 | 8.06 ± 0.03 | 3.74 ± 0.02 |
| IRAS 05073 | 16.57 ± 0.06 | 15.37 ± 0.05 | 14.53 ± 0.03 | 12.42 ± 0.34 | 11.40 ± 0.14 | 9.69 ± 0.01 | 7.57 ± 0.01 | 3.26 ± 0.03 |
| IRAS 05063 | 15.08 ± 0.17 | 13.86 ± 0.11 | 13.16 ± 0.16 | 11.45 ± 0.29 | 10.44 ± 0.17 | 9.17 ± 0.03 | 7.56 ± 0.01 | 3.57 ± 0.00 |
| IRAS 05413 | 15.59 ± 0.10 | 14.20 ± 0.15 | 13.11 ± 0.14 | 11.27 ± 0.66 | 10.38 ± 0.45 | 9.14 ± 0.04 | 7.67 ± 0.03 | 3.72 ± 0.01 |
| IRAS 00350 | 11.37 ± 0.07 | 10.19 ± 0.04 | 9.10 ± 0.03 | 7.68 ± 0.08 | 7.03 ± 0.05 | 6.51 ± 0.00 | 5.80 ± 0.02 | 3.55 ± 0.00 |
| IRAS 05127 | 15.52 ± 0.16 | 15.05 ± 0.06 | 14.15 ± 0.25 | 12.58 ± 0.23 | 11.80 ± 0.00 | 10.11 ± 0.02 | 8.25 ± 0.02 | 3.64 ± 0.00 |
| J010546 | 14.72 ± 0.01 | 14.62 ± 0.03 | 14.47 ± 0.12 | 13.54 ± 0.03 | 12.89 ± 0.07 | 10.62 ± 0.04 | 8.13 ± 0.02 | 4.92 ± 0.03 |
| IRAS F05192 | 14.64 ± 0.05 | 14.25 ± 0.03 | 13.92 ± 0.14 | 12.83 ± 0.22 | 11.53 ± 0.04 | 9.43 ± 0.01 | 7.17 ± 0.03 | 3.41 ± 0.01 |
| J052043 | 13.17 ± 0.30 | 12.73 ± 0.32 | 12.52 ± 0.26 | 12.23 ± 0.49 | 12.22 ± 0.26 | 11.31 ± 0.01 | 8.94 ± 0.00 | 4.46 ± 0.04 |
| IRAS 05110 | 13.29 ± 0.01 | 12.83 ± 0.04 | 12.60 ± 0.08 | 12.19 ± 0.10 | 11.70 ± 0.04 | 9.92 ± 0.03 | 7.38 ± 0.00 | 3.56 ± 0.00 |
| IRAS Z05259 | 13.65 ± 0.04 | 13.46 ± 0.06 | 13.33 ± 0.07 | 13.12 ± 0.03 | 12.96 ± 0.03 | 11.24 ± 0.04 | 8.59 ± 0.01 | 4.12 ± 0.01 |
| J004441 | 13.63 ± 0.06 | 13.25 ± 0.02 | 13.04 ± 0.08 | 12.33 ± 0.07 | 11.87 ± 0.04 | 10.39 ± 0.00 | 8.32 ± 0.02 | 5.13 ± 0.01 |
| NGC 1978 WBT 2665 | 14.72 ± 0.07 | 13.63 ± 0.11 | 12.97 ± 0.15 | 11.96 ± 0.10 | 11.23 ± 0.06 | 9.52 ± 0.01 | 7.33 ± 0.00 | 3.33 ± 0.03 |
| IRAS 06111 | 16.29 ± 0.04 | 14.93 ± 0.07 | 14.08 ± 0.06 | 12.39 ± 0.02 | 11.04 ± 0.02 | ··· | ··· | ··· |
| IRAS 05092 | 15.28 ± 0.13 | 14.80 ± 0.04 | 14.17 ± 0.04 | 11.91 ± 0.26 | 11.22 ± 0.07 | 8.95 ± 0.06 | 6.93 ± 0.02 | 3.90 ± 0.05 |
| IRAS 05185 | 16.62 ± 0.23 | 15.63 ± 0.14 | 14.65 ± 0.07 | 11.49 ± 0.23 | 10.80 ± 0.02 | 8.38 ± 0.03 | 6.49 ± 0.01 | 3.33 ± 0.03 |
| IRAS 05360 | 16.28 ± 0.20 | 15.15 ± 0.05 | 14.14 ± 0.12 | 11.57 ± 0.23 | 10.46 ± 0.03 | 8.49 ± 0.01 | 6.67 ± 0.00 | 3.31 ± 0.03 |
| SMP SMC 011 | 16.10 ± 0.21 | 15.44 ± 0.15 | 15.27 ± 0.10 | 14.90 ± 0.02 | 14.87 ± 0.06 | ··· | ··· | ··· |
| IRAS 05315 | 18.54 ± 0.08 | 17.94 ± 0.11 | 17.23 ± 0.22 | 13.89 ± 0.03 | 12.12 ± 0.14 | 10.22 ± 0.00 | 7.83 ± 0.00 | 2.76 ± 0.02 |
| IRAS 05495 | ··· | ··· | 15.52 ± 0.21 | 13.63 ± 0.12 | 11.31 ± 0.03 | 8.45 ± 0.03 | 2.42 ± 0.04 | ··· |
| SMP SMC 025 | 17.89 ± 0.20 | 17.56 ± 0.40 | 16.84 ± 0.10 | 15.95 ± 0.13 | 14.67 ± 0.14 | 13.67 ± 0.07 | 11.68 ± 0.03 | 5.88 ± 0.02 |
| SMP LMC 099 | 16.07 ± 0.01 | 15.92 ± 0.04 | 14.95 ± 0.12 | 13.51 ± 0.03 | 12.49 ± 0.02 | ··· | ··· | ··· |

was determined assuming a distance modulus of 18.50 to the LMC and 18.90 to the SMC, and $M_{bol} = -4.75$ for the Sun. $M_{bol} = -5.2$ corresponds to $\approx 10^4\ L_\odot$.

For the Fullerene group, we modified the procedure for determining bolometric magnitude. The blue $U - B$ colors point to the presence of emission from the central star in the spectrum, and to account for this additional emission, we appended a 30,000 K blackbody to the spectrum, scaling it to the $U$ magnitude. The bolometric magnitudes in Table 19 reflect this correction, which raised the brightness of the sources 1.5 mag on average. Before the correction, the bolometric magnitudes ranged from −2.1 to −3.4, compared to −3.6 to −4.8 after.

TABLE 19
COMBINED UBVI PHOTOMETRY AND BOLOMETRIC MAGNITUDES

| Target | $U$ | $B$ | $V$ | $I$ | $M_{\rm bol}$ |
|---|---|---|---|---|---|
| SMP LMC 002 | 15.97 ± 0.06 | 17.13 ± 0.03 | 17.01 ± 0.00 | 17.26 ± 0.07 | −3.99[a] |
| SMP LMC 056 | 16.56 ± 0.09 | 17.36 ± 0.04 | 17.11 ± 0.03 | 17.39 ± 0.15 | −3.61[a] |
| SMP SMC 024 | 15.67 ± 0.04 | 16.66 ± 0.04 | 15.90 ± 0.03 | 17.04 ± 0.07 | −4.81[a] |
| LIN 49 | 15.86 ± 0.05 | 17.10 ± 0.02 | 17.23 ± 0.03 | 17.04 ± 0.12 | −4.58[a] |
| SMP SMC 016 | 15.78 ± 0.05 | 16.94 ± 0.02 | 16.81 ± 0.02 | 16.94 ± 0.03 | −4.73[a] |
| SMP SMC 018 | 15.83 ± 0.03 | 16.64 ± 0.04 | 15.99 ± 0.05 | 16.35 ± 0.35 | −4.33 |
| SMP SMC 013 | 16.12 ± 0.04 | 16.30 ± 0.04 | 15.34 ± 0.02 | 16.89 ± 0.17 | −3.61 |
| SMP SMC 015 | 15.72 ± 0.05 | 16.24 ± 0.10 | 15.33 ± 0.03 | 16.51 ± 0.12 | −4.44 |
| SMP SMC 001 | ··· | ··· | ··· | 16.91 ± 0.07 | −4.42 |
| SMP LMC 008 | 16.65 ± 0.04 | 16.98 ± 0.03 | 15.95 ± 0.04 | 16.58 ± 0.06 | −4.84 |
| SMP LMC 048 | 15.38 ± 0.08 | 16.45 ± 0.04 | 15.10 ± 0.01 | 16.11 ± 0.02 | −4.21 |
| SMP LMC 025 | 15.26 ± 0.06 | 15.83 ± 0.03 | 14.82 ± 0.11 | 16.33 ± 0.13 | −4.24 |
| SMP LMC 085 | 15.83 ± 0.04 | 16.53 ± 0.02 | 15.71 ± 0.02 | 16.39 ± 0.04 | −4.73 |
| SMP LMC 076 | 15.85 ± 0.04 | 16.42 ± 0.02 | 15.51 ± 0.04 | 16.85 ± 0.06 | −3.66 |
| SMP LMC 058 | 15.94 ± 0.04 | 16.24 ± 0.05 | 15.35 ± 0.03 | 16.55 ± 0.04 | −4.39 |
| SMP SMC 027 | ··· | ··· | ··· | 16.75 ± 0.09 | −2.65 |
| SMP LMC 051 | 17.95 ± 0.06 | 17.56 ± 0.04 | 16.26 ± 0.10 | 17.10 ± 0.15 | −4.80 |
| IRAS 05370 | 20.44 ± 0.37 | 21.23 ± 0.24 | 18.78 ± 0.17 | 18.08 ± 0.03 | −4.99 |
| IRAS 05537 | ··· | ··· | ··· | 17.67 ± 0.24 | −4.93 |
| SMP SMC 020 | ··· | ··· | ··· | 16.73 ± 0.08 | −3.71 |
| IRAS 05588 | 15.98 ± 0.05 | 16.04 ± 0.02 | 15.51 ± 0.13 | 14.92 ± 0.10 | −5.35 |
| SMP SMC 006 | 16.98 ± 0.04 | 16.98 ± 0.13 | 15.95 ± 0.04 | 17.13 ± 0.20 | −4.82 |
| IRAS 05073 | ··· | ··· | ··· | ··· | −4.81 |
| IRAS 05063 | ··· | ··· | ··· | ··· | −4.78 |
| IRAS 05413 | ··· | ··· | ··· | ··· | −4.64 |
| IRAS 00350 | 17.04 ± 0.07 | 15.95 ± 0.05 | 14.59 ± 0.02 | 13.06 ± 0.07 | −7.07 |
| IRAS 05127 | 15.60 ± 0.07 | 16.59 ± 0.04 | 16.30 ± 0.21 | 16.05 ± 0.11 | −4.44 |
| J010546 | 15.44 ± 0.03 | 15.82 ± 0.03 | 15.44 ± 0.06 | 15.02 ± 0.11 | −4.39 |
| IRAS F05192 | 20.13 ± 0.16 | 19.21 ± 0.06 | 17.67 ± 0.26 | 15.71 ± 0.11 | −4.82 |
| J052043 | 17.62 ± 0.07 | 16.52 ± 0.06 | 15.13 ± 0.08 | 13.87 ± 0.08 | −4.43 |
| IRAS 05110 | 20.53 ± 0.19 | 18.42 ± 0.05 | 16.63 ± 0.03 | 14.51 ± 0.02 | −4.91 |
| IRAS Z05259 | 17.56 ± 0.04 | 16.57 ± 0.03 | 15.37 ± 0.04 | 14.92 ± 1.16 | −4.34 |
| J004441 | 19.25 ± 0.15 | 17.52 ± 0.02 | 15.96 ± 0.18 | 14.45 ± 0.01 | −4.42 |
| NGC 1978 WBT 2665 | ··· | ··· | ··· | 16.31 ± 0.07 | −4.94 |
| IRAS 06111 | ··· | ··· | ··· | 18.04 ± 0.17 | −5.07 |
| IRAS 05092 | ··· | 20.18 ± 0.05 | 18.41 ± 0.05 | 16.39 ± 0.11 | −4.67 |
| IRAS 05185 | ··· | ··· | ··· | 18.04 ± 0.19 | −5.17 |
| IRAS 05360 | ··· | ··· | ··· | ··· | −5.07 |
| SMP SMC 011 | ··· | 20.73 ± 0.09 | 19.03 ± 0.13 | 16.93 ± 0.23 | −5.79 |
| IRAS 05315 | ··· | ··· | ··· | ··· | −4.94 |
| IRAS 05495 | ··· | ··· | ··· | ··· | −5.30 |
| SMP SMC 025 | 17.84 ± 0.05 | 18.33 ± 0.05 | 17.70 ± 0.10 | 18.65 ± 0.06 | −2.41 |
| SMP LMC 099 | ··· | ··· | ··· | 17.02 ± 0.12 | −3.30 |

[a] Modified by adding a 30,000 K Planck function.

REFERENCES


Acke, B., Bouwman, J., Juhász, A., et al. 2010, ApJ, 718, 558
Allamandola, L. J., Tielens, A. G. G. M., & Barker, J. R. 1989, ApJS, 71, 733
Bernard-Salas, J., Peeters, E., Sloan, G. C., et al. 2006, ApJ, 652, L29
Bernard-Salas, J., Peeters, E., Sloan, G. C., et al. 2009, ApJ, 699, 1541
Bernard-Salas J., Cami, J., Peeters, E., et al. 2012, ApJ, 757, 41
Berné, O., & Tielens, A. G. G. M. 2012, PNAS, 109, 401
Berné, O., Mulas, G., & Joblin, C. 2013, A&A, 550, L4
Bocchio, M., Micelotta, E. R., Gautier, A.-L., & Jones, A. P. 2012, A&A, 545, A124
Bolatto, A. D., Simon, J. D., Stanimirović, S., et al. 2007, ApJ, 655, 212
Bregman, J. D., Allamandola, L. J., Tielens, A. G. G. M., Geballe, T. R., & Witteborn, F. C. 1989, ApJ, 344, 791
Buchanan, C. L., Kastner, J. H., Forrest, W. J., et al. 2006, AJ, 132, 1890
Cami, J., Bernard-Salas, J., Peeters, E., & Malek, S. E. Science, 329, 1180
Casassus, S., Roche, P. F., Aitken, D. K., & Smith, C. H. 2001, MNRAS, 327, 744
Cerrigone, L., Hora, J. L., Umana, G., et al. 2011, ApJ, 738, 121
Cioni, M.-R., Loup, C., Habing, H. J., et al. 2000, A&AS, 144, 235
Clayton, G. C. 2012, J. Am. Assoc. Var. Star Obs. 40, 539
Cox, A. N., ed., 2000, Allen's Astrophysics Quantities, 4th Ed., (New York: Springer)
Cutri, R. M., Skrutskie, M. F., van Dyk, S., et al. 2006, 2MASS 6X Point Source Working Database/Catalog, VizieR On-line Data Catalog II/281
De Smedt, K., Van Winckel, H., Karakas, A. I., et al. 2012, A&A, 541, A67
Dopita, M. A., Vassiliadis, E., Meatheringham, S. J., et al. 1994, ApJ, 426, 150
Duley, W. W., & Williams, D. A. 1981, MNRAS, 196, 269
Evans, A., Gehrz, R. D., Woodward, C. E., & Helton, L. A. 2010, MNRAS, 406, L85
Forrest, W. J., Houck, J. R., & McCarthy, J. F. 1981, ApJ, 248, 195
Forrest, W. J., Sargent, B., Furlan, E., et al. 2004, ApJS, 154, 443
García-Hernández, D. A., Manchado, A., García-Lario, P., et al. 2010, ApJ, 724, L39
García-Hernández, D. A., Iglesias-Groth, S., Acosta-Pulido, J. A., et al. 2011, ApJ, 737, L30
García-Hernández, D. A., Villaver, E., García-Lario, P., et al. 2012, ApJ, 760, 107
García-Hernández, Kameswara Rao, N, & Lambert, D. L. 2013, ApJ, 773, 107
Geballe, T. R., Joblin, C., d'Hendecourt, L. B., et al. 1994, ApJ, 434, L15
Goebel, J. H., & Moseley, S. H. 1985, ApJ, 290, L35
Gordon, K. D., Meixner, M., Meade, M. R., et al. 2011, AJ, 142, 102
Groenewegen, M. A. T., Sloan, G. C., Soszyński, I., & Petersen, E. 2009, A&A, 506, 1277
Gruendl, R. A., Chu, Y.-H., Seale, J. P., et al. 2008, ApJ, 688, L9
Hao, L., Spoon, H. W. W., Sloan, G. C., et al. 2005, ApJ, 625, L75
Hill, H. G. M., Jones, A. P., & d'Hendecourt, L. B. 1998, A&A, 336, L41
Herald, J. E., & Bianchi, L. 2004, ApJ, 611, 294
Hony, S., Waters, L. B. F. M., & Tielens, A. G. G. M. 2002, A&A, 390, 533
Hony, S., Kemper, F., Woods, P. M., et al. 2011, A&A, 531, 137
Houck, J. R., Roellig, T. L., & van Cleve, J., et al. 2004, ApJS, 154, 18
Jones, A. P. 2012a, A&A, 540, A1
Jones, A. P. 2012b, A&A, 542, A98
Jones, A. P., Duley, W. W., & Williams, D. A. 1990, QJRAS, 31, 567
Justtanont, K., Barlow, M. J., Skinner, C. J., et al. 1996, A&A, 309, 612
Kato, D., Nagashima, Ch., Nagayima, T., et al. 2007, PASJ, 59, 615
Keller, L. D., Sloan, G. C., Forrest, W. J., et al. 2008, ApJ, 684, 411
Kraemer, K. E., Sloan, G. C., Price, S. D., & Walker, H. J. 2002, ApJS, 140, 389
Kraemer, K. E., Sloan, G. C., Wood, P. R., Price, S. D., & Egan, M. P. 2005, ApJ, 631, L147
Kraemer, K. E., Sloan, G. C., Bernard-Salas, J., Price, S. D., Egan, M. P., & Wood, P. R. 2006, ApJ, 652, L25
Kwok, S., Hrivnak, B. J., & Volk, K. M. 1989, ApJ, 345, L51
Kwok, S., & Zhang, Y. 2011, Nature, 479, 80
Lagadec, E., Zijlstra, A. A., Sloan, G. C., et al. 2007, MNRAS, 376, 1270
Lagadec, E., Zijlstra, A. A., Sloan, G. C., et al. 2009, MNRAS, 396, 598
Lagadec, E., Sloan, G. C., Zijlstra, A. A., Mauron, N., & Houck, J. R. 2012, MNRAS, 427, 2588
Lebouteiller, V., Bernard-Salas, J., Sloan, G. C., & Barry, D. J. 2010, PASP, 122, 188
Leisenring, J. M., Kemper, F., & Sloan, G. C. 2008, ApJ, 681, 1557
Leisy, P., & Dennefeld, M. 2006, A&A, 456, 451
Li, A., & Draine, B. T. 2002, ApJ, 572, 232
Lombaert, R., de Vries, B. L., de Koter, A., et al. 2012, A&A, 544, L18
Malek, S. E., Cami, J., & Bernard-Salas, J. 2012, ApJ, 744, 16
Martin, P. G., & Rogers, C. 1987, ApJ, 322, 374
Matsuura, M., Sloan, G. C., Bernard-Salas, J., Volk, K., & Hrivnak, B. J., 2011, Proc. of the Asymmetrical Planetary Nebula V Conf., ed. A. A. Zijlstra, et al., 97
Matsuura, M., Bernard-Salas, J., Lloyd Evans, T., et al. 2014, MNRAS, 439, 1472
Meixner, M., Gordon, K. D., Indebetouw, R., et al. 2006, AJ, 132, 2268
Micelotta, E. R., Jones, A. P., Cami, J., Peeters, E., Bernard-Salas, J., & Fanchini, G. 2012, ApJ, 761, 35
Micelotta, E. R., Jones, A. P., Tielens, A. G. G. M. 2010a, A&A, 510, A36
Micelotta, E. R., Jones, A. P., Tielens, A. G. G. M. 2010b, A&A, 510, A37
Nemes, L., Ram, S. R., Bernath, P. F., et al. 1994, Chem. Phys. Lett., 218, 295
Otsuka, M., Kemper, F., Hyung, S., et al. 2013, ApJ, 764, 77
Peeters, E., Hony, S., Van Kerckhoven, C., et al. 2002 A&A, 390, 1089
Pino, T., Dartois, E., Cao, A.-T., et al. 2008, A&A, 490, 665
Rieke, G. H., & Lebofsky, M. J. ApJ, 288, 618
Sanduleak, N., MacConnell, D. J., & Philip, A. G. D. 1978, PASP, 90, 621
Sellgren, K., Werner, M. W., Ingalls, J. G., et al. 2010, ApJ, 722, L54
Skrutskie, M. F., Cutri, R. M., Stiening, R., et al. 2006, AJ, 131, 1163
Sloan, G. C., Bregman, J. D., Geballe, T. R., Allamandola, L. J., & Woodward, C. E. 1997, ApJ, 474, L101
Sloan, G. C., Kraemer, K. E., Price, S. D., & Shipman, R. F. 2003, ApJS, 147, 379
Sloan, G. C., Kraemer, K. E., Matsuura, M., et al. 2006, ApJ, 645, 1118
Sloan, G. C., Jura, M., Duley, W. W., et al. 2007, ApJ, 664, 1144
Sloan, G. C., Matsuura, M., Lagadec, E., et al. 2012, ApJ, 752, 140
Sloan, G. C., Herter, T. L., Charmandaris, V., et al. 2014, AJ, submitted
Smolders, K., Acke, B., Verhoelst, T., et al. 2010, A&A, 514, L1
Soszyński, Udalski, A., Szymański, M. K., et al. 2009, AcA, 59, 335
Soszyński, Udalski, A., Szymański, M. K., et al. 2011, AcA, 61, 217
Spano, M., Mowlavi, N., Eyer, L., et al. 2013, A&A, 536, A60
Speck, A. K., Thompson, G. D., & Hofmeister, A. M. 2005, ApJ, 634, 426
Stanghellini, L., García-Lario P., Garcá-Hernández, D. A., et al. 2007, ApJ671, 1669
Ulaczyk, K., Szymańsky, M. K., Udalski, A., et al. 2012, Acta Astron., 62, 247
Villaver, E., Stanghellini, L., & Shaw, R. A. 2003, ApJ, 597, 298
Villaver, E., Stanghellini, L., & Shaw, R. A. 2004, ApJ, 614, 716
Volk, K., Hrivnak, B. J., Matsuura, M., et al. ApJ, 735, 127
Volk, K., Kwok, S., Hrivnak, B. J., & Szczerba, R. 2002, ApJ, 567, 412
Werner, M. W., Roellig, T. L., Low, F. J., et al. 2004a, ApJS, 154, 1
Werner, M. W., Uchida, K. I., Sellgren, K., et al. 2004b, ApJS, 154, 309
Whitelock, P. A., Feast, M. W., Menzies, J. W., & Catchpole, R. M. 1989, MNRAS, 238, 769
Wright, E. L., Eisenhardt, P. R. M., Mainzer, A. K., et al. 2010, AJ, 140, 1868
Zaritsky, D., Harris, J., Thompson, I. B., Grebel, E. K., & Massey, P. 2002, AJ, 123, 855
Zaritsky, D., Harris, J., Thompson, I. B., & Grebel, E. K. 2004, AJ, 128, 1606
Zhang, K., Jiang, B. W., & Li, A. 2009a, MNRAS, 396, 1247
Zhang, K., Jiang, B. W., & Li, A. 2009b, ApJ, 702, 680
Zhukovska, S., & Gail, H.-P. 2008, A&A, 486, 229

Zijlstra, A. A., Matsuura, M., Wood, P. R., et al. 2006, MNRAS, 370, 1961